

Year 2 Annual Report: 1 January 1994 - 31 December 1994
Correlations Between Micromagnetic, Microstructural and Microchemical Properties
in Ultrathin Epitaxial Magnetic Structures

M.R. Scheinfein^{a,b}, and G.G. Hembree^a

^aDepartment of Physics and Astronomy

^bCenter for Solid State Science

Arizona State University

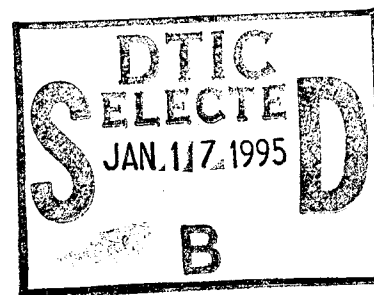
Tempe, AZ 85287-1504

A Proposal Supported By The Office Of Naval Research
(N00014-93-1-0099)

Project Director

Dr. Richard G. Brandt

Electronics Division - Code 312



Technical Representative:

Michael R. Scheinfein

(602) 965-9658 Phone

(602) 965-7954 FAX

shine@shine.la.asu.edu

scheinfein@phyast.la.asu.edu

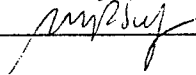
e-mail

e-mail

Signatures:

Michael R. Scheinfein

Department of Physics and Astronomy



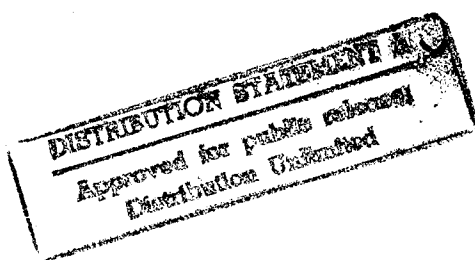
Date:

12/30/94

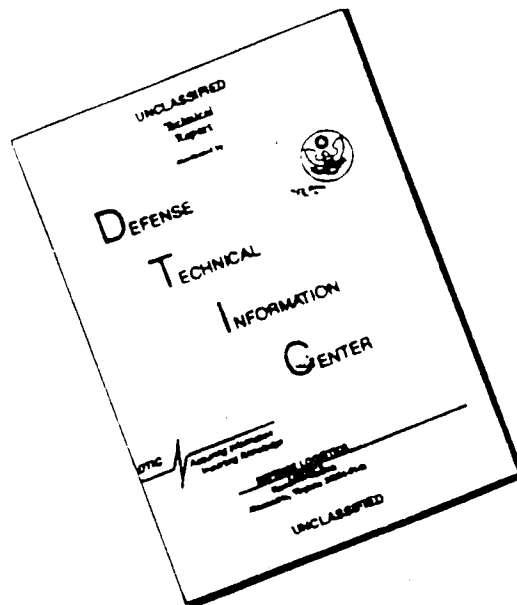
Teresa Demonte

Sponsored Projects

Date:



DISCLAIMER NOTICE



THIS DOCUMENT IS BEST QUALITY AVAILABLE. THE COPY FURNISHED TO DTIC CONTAINED A SIGNIFICANT NUMBER OF PAGES WHICH DO NOT REPRODUCE LEGIBLY.

Contents

0.0	Contents	2
1.0	Introduction	3
2.0	Fe/CaF ₂ /Si(111)	3
3.0	Ag/Fe/CaF ₂ /Si(111)	15
4.0	[Co/Cu] _n Co/Si(100)	21
5.0	Electron Holography	28
6.0	Research Plans : Year 3	42
7.0	Appendix A: Associated Staff	42
8.0	Appendix B: Publication List	43
9.0	Appendix C: 1994 Publications	45

Accession For	
NTIS GRA&I	<input checked="" type="checkbox"/>
DTIC TAB	<input type="checkbox"/>
Unannounced	<input type="checkbox"/>
Justification	
By <i>See ADA277200</i>	
Distribution/	
Availability Codes	
Dist	Avail and/or Special
<i>A-1</i>	<i>23</i>

1.0 Introduction:

The proposed goal of this project is to obtain quantitative measurements of the microstructural, microchemical and micromagnetic properties of surfaces and interfaces of ultrathin films composed of magnetic materials deposited on non-magnetic, antiferromagnetic (metal) and insulating substrates. Surface microanalytic methods based on a unique ultrahigh-vacuum scanning transmission electron microscope/scanning electron microscope (UHV-STEM/SEM) equipped with in-situ thin film preparation and characterization tools are being used. Magnetic characterization is performed in-situ using the surface magneto-optical Kerr effect (SMOKE). Additional magnetic microstructure measurements are being conducted in a novel STEM based electron holography system where absolutely calibrated nanometer resolution magnetometry is possible. The measurements are designed to clarify the relationship between observed real-space micro-structure of interfaces, ultrathin magnetic films and superlattices with magnetic properties, such as surface anisotropy. The dependence of magnetic properties on film morphology, which may be a function of the deposition parameters during the initial stages of growth, and on structural properties such as strain and interface roughness is being studied. We are exploring the electron beam modification of CaF_2 and CoF_2 , both as an electron beam resist and as a damagable material for preferential nucleation, as a means of defining one and two dimensional nanometer sized epitaxial magnetic devices. Here, we report on our progress in year 2 of this 3 year project.

2.0 $\text{Fe}/\text{CaF}_2/\text{Si}(111)$

Iron was deposited at a rate of 0.1-0.2 ML/min ($1\text{ML}=7.7\times 10^{14}$ atom/ cm^2) using an electron-bombardment Fe evaporator. The evaporation rate was measured by RBS, AES, and quartz-crystal microbalance techniques. The base pressure of the system was less than 5×10^{-11} mbar but increased to 2×10^{-9} mbar during Fe growth. The substrates were held at a constant temperature between 20 and 400 °C.

The initial stages of Fe growth proceed by three-dimensional islanding on $\text{CaF}_2(111)$ surfaces. Surfaces with less than 7 ML of Fe could not be analyzed because of a poor signal-to-noise ratio of the SE microscopy images, as was the case for bulk specimens. Iron film coverages of 7-8 ML yielded nearly hemispherically-shaped islands such that an average Fe island diameter [$D=2(\text{cross-sectional area} / \pi)^{1/2}$] could be determined from the micrographs. The statistical analysis performed on these images yielded the following information for Fe coverages between 7 and 8 ML grown on 10-25 nm thick $\text{CaF}_2/\text{Si}(111)$ substrates maintained at a constant temperature of 20 through 300 °C: (1) an average Fe island diameter of 2.0 ± 0.3 nm; (2) a range of Fe island diameters where 85% of the population will lie within 2.0 ± 1.0 nm; (3) a 23% coverage of $\text{CaF}_2(111)$ with Fe islands; (4) the number of Fe islands per unit area is 7.4×10^{12} islands/ cm^2 ; (5) the mean distance between Fe island centers is approximately 3.7 ± 0.6 nm; (6) no geometric ordering of the islands was observed based on fast Fourier transform image analysis.

Particle size analysis of the SE images revealed no statistical difference between the diameters and spatial distributions of Fe islands grown on $\text{CaF}_2/\text{Si}(111)$ substrates held at room temperature through 300 °C. Figure 2.1 exhibits the island distributions on four different $\text{CaF}_2/\text{Si}(111)$ surfaces held at various temperatures during Fe growth. All of the CaF_2 films are approximately 10 nm in thickness and covered with 7-8 ML of Fe. All of these films were observed at room temperature. Figures 2.1(a), 2.1(b), 2.1(c), and 2.1(d) are SE images taken of surfaces which were grown while the substrates were held at a fixed temperature of 20, 140, 300, and 400 °C, respectively. As can be seen in Figs. 2.1(a)-2.1(c), the Fe island size and spatial distributions are nearly identical for Fe films grown on substrates held between room temperature and 300 °C. The lack of a temperature dependence on the Fe island size and spatial distributions, for those films grown between 20 and 300 °C, implies that the island nucleation density is not determined by a diffusion length. A more probable explanation for the temperature

THIS QUANTUM EFFECTS

19950112 033

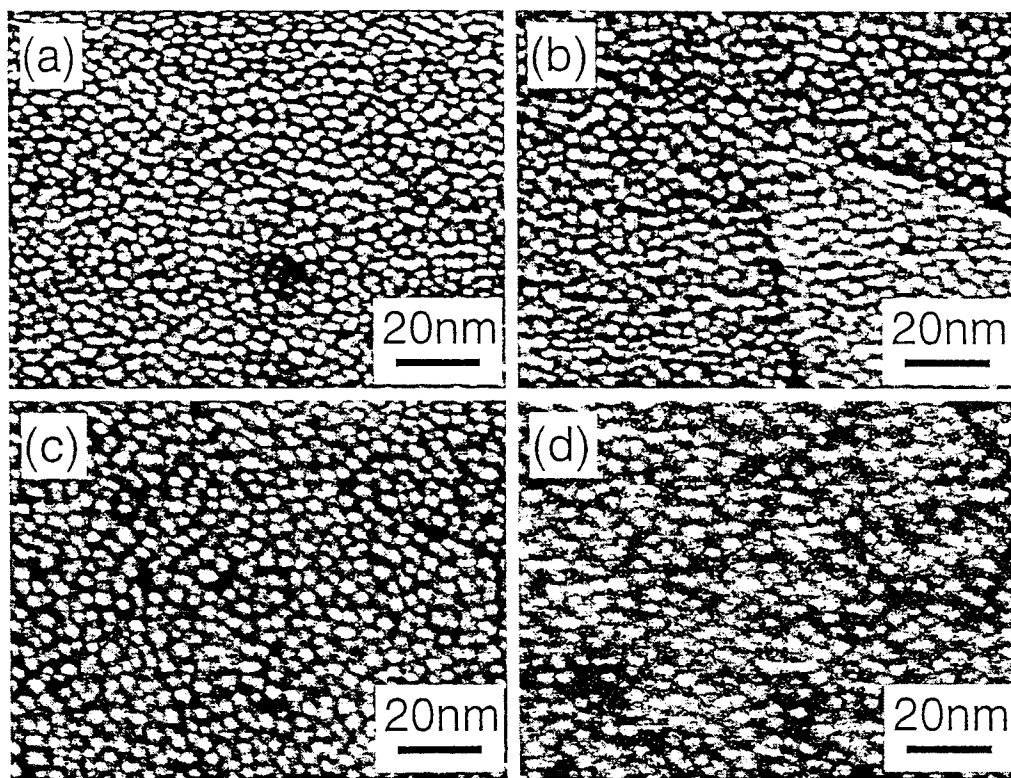


FIG. 2.1. Fe island distributions for four different $\text{CaF}_2/\text{Si}(111)$ substrates held at a constant temperature of (a) 20, (b) 140, (c) 300, and (d) 400 °C during growth. All of the CaF_2 films are approximately 10 nm thick and covered with 7-8 ML of Fe. A relaxed CaF_2 film was used as a substrate in (b). CaF_2 decomposition at higher temperatures is responsible for the change in nucleation density observed in (d).

independent distributions is the existence of Fe-receptive chemical bonds or atom-trapping defects on the substrate

Venables has applied the kinetic growth model to the Fe/CaF_2 system. A value of 4.28 eV and 1.1×10^{13} Hz for the sublimation energy (L) and adsorption frequency, respectively, were computed using the Einstein model so that the calculated vapor pressure matches experimental results. This computed value is in complete agreement with the experimental sublimation energy of 4.28 ± 0.01 eV. An Fe atom binding energy, E_b , equal to 1.00 eV yields an island surface density consistent with our observations, even though the experimental binding energy of Fe is 1.04 ± 0.22 eV *in vacuo* rather than on a two-dimensional surface. For a hexagonal lattice the binding energy reduces to $L = E_a + 3E_b$ for nearest neighbor pair bonds, resulting in an adsorption energy, E_a , of 1.28 eV. Venables has determined, after incorporating these parameters into the model, that a stable Fe cluster size of one atom is consistent with the theory from 20 to 400 °C. In addition, an adsorption energy of 1.28 eV will give complete condensation of Fe atoms up to around 300 °C. The model also predicts a diffusion energy, E_d , of 0.5-0.6 eV for the room-temperature depositions resulting in $7\text{-}9 \times 10^{12}$ Fe islands/ cm^2 . A diffusion energy of ~ 0.5 eV is comparable with, but slightly higher than similarly calculated values for Au/KCl (0.279-0.294 eV) and Au/NaF (0.120-0.385 eV). The model has been employed for Ag on $\text{Mo}(100)$ and $\text{Si}(100)$ experimental results which give Ag adatom diffusion energies of 0.45 and 0.7 eV, respectively. However, it underestimates the Fe island density on CaF_2 near $T=300$ °C by more than a factor of 20. This failure to accurately predict the Fe island density from $20 < T < 300$ °C is probably due to CaF_2 surface imperfections. Venables' model does not explicitly include surface defects, although defects essentially reduce the diffusion coefficients. Metallic

depositions performed on NaCl surfaces which were formed *in situ* (by cleaving the crystal) had a lower island surface density than for surfaces which were exposed to normal atmospheric conditions. Since CaF_2 is also very hygroscopic it is likely that island nucleation is enhanced (and constant from $20 < T < 300$ °C) because the samples were not grown *in situ*, rather, they were introduced to UHV conditions *after* CaF_2 film production. Annealing the CaF_2 to temperatures near 400 °C was not effective in restoring the original UHV-produced $\text{CaF}_2(111)$ surface. As a result, constant Fe island nucleation is favored for a substantial temperature range. The *in situ* growth of CaF_2 followed by Fe deposition is expected to verify this hypothesis.

Iron films of various coverages were deposited on 10-nm thick, unrelaxed CaF_2 films to characterize the Fe morphology as a function of Fe coverage. Iron coverages of 7.5, 10, 15, 20, 30, and 48 ML grown on room-temperature substrates are shown in Figs. 2.2(a)-2.2(f), respectively. The 7.5 ML Fe film of Fig. 2.2(a) displays the resulting hemispherical Fe islands. As the Fe growth proceeds, the islands enlarge [Fig. 2.2(b), 10 ML of Fe] until one "meandering" island is composed of two to three of the original hemispherical islands. A comparison of the 15 ML film in Fig. 2.2(c) with the 7.5 ML film of Fig. 2.2(a) exhibits the initial stages of "meandering" island formation. Further Fe depositions [i.e. 20 ML film in Fig. 2.2(d) and 30 ML film in Fig. 2.2(e)] yield a network of still larger "meandering" islands. The islands increase in size by branching out and connecting with other "meandering" islands until only one island exists. Although not continuous within the surface plane, Fig. 2.2(f) displays a completely connected (one island in the field of view) film for a 48 ML deposition. Table 2.1 summarizes the particle statistics of these six surfaces.

Unlike most metal on insulator systems, the Fe islands on these CaF_2 surfaces do not grow into larger round-shaped structures with successive depositions. If we calculate the number, N_i , of Fe atoms/island at all Fe coverages, we see that N_i is proportional to the volume for total coverages less than 15 ML and that N_i is proportional to the area for total coverages more than 15 ML. *In situ* magnetic measurements have reconfirmed the existence of two-dimensional island growth because the effective magnetic moment is proportional to the Fe island area rather than to the volume. The two growth processes may be due to a high concentration of Fe-receptive chemical bonds which trap Fe adatoms. The island diameter grows once a single adsorbate atom nucleates at one of these sites. In addition, the number of Fe-receptive surface sites must be comparable to the nucleation density just before two-dimensional growth is initiated (i.e., $\sim 7 \times 10^{12}$ sites/cm² from Table 2.1). Two-dimensional island growth occurs because the available atomic sites have become saturated and the Fe adatoms are able to travel to and bond with pre-existing Fe islands. The Fe adatoms minimize the energy of the system by covering the relatively high energy Fe surface rather than covering the remaining, exposed CaF_2 surface. Therefore, "meandering" island growth is favored for Fe deposited on *ex situ*-created $\text{CaF}_2(111)$ surfaces.

TABLE 2.1. Particle statistics for various coverages of Fe on 10 nm thick CaF_2 surfaces.

Fe Coverage (ML)	CaF_2 Surface Coverage (%)	Average Fe Island Area (nm ²)	Number of Islands per Area ($\times 10^{-2}$ islands/nm ²)
7.5	19 ± 2	2.65 ± 0.25	7.15 ± 0.44
10	25 ± 4	3.22 ± 0.64	7.71 ± 0.56
15	29 ± 2	6.00 ± 0.92	4.83 ± 0.44
20	42 ± 2	15.2 ± 2.5	2.82 ± 0.43
30	48 ± 5	35.0 ± 14.8	1.55 ± 0.46
48	62 ± 2	NA	NA

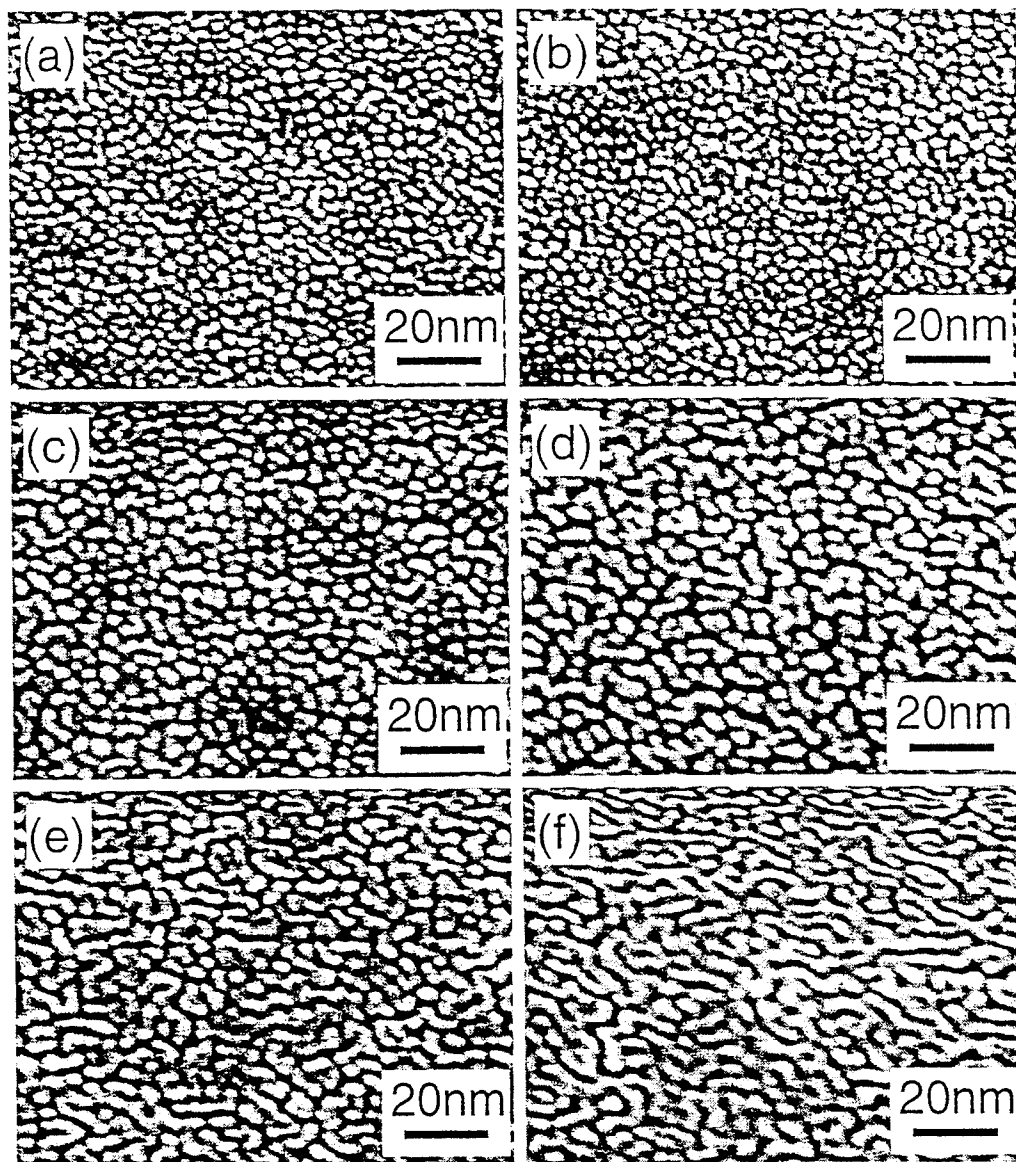


FIG. 2.2. Secondary electron images of (a) 7.5, (b) 10, (c) 15, (d) 20, (e) 30, and (f) 48 ML Fe films grown at room temperature on 10-nm thick, unrelaxed CaF_2 . A 7.5 ML Fe film (a) is characterized by a uniform coverage of 2-nm diameter Fe islands. As more Fe is deposited the hemispherically-shaped islands form into "meandering" islands [(c), (d), and (e)]. The "meandering" islands eventually become completely connected when the Fe coverage approaches 48 ML (f).

The initial stages of $\text{Fe}/\text{CaF}_2(111)$ growth proceed by three-dimensional islanding on relaxed, unrelaxed, 10, ~ 800 nm, and bulk CaF_2 surfaces. As an example of this, Figs. 6.12(a)-6.12(d) display four $\text{CaF}_2(111)$ surfaces with nominally 7.5 ML of room-temperature grown Fe. Visual inspection of these SE images portrays the independent Fe island size and spatial distribution of Fe on various $\text{CaF}_2(111)$ surfaces. A relatively even distribution of 2.0-nm diameter Fe islands was measured on the 10 nm thick relaxed and unrelaxed surfaces shown in Figs. 2.3(a) and 2.3(b), respectively. Due to electron-beam induced charging of ~ 800 nm thick and bulk CaF_2 substrates, island size analysis was not possible. Since the bulk CaF_2 surface had not been exposed to solvents during 3-mm disc preparations and since the island distributions are similar for all four surfaces, it is doubtful that disc preparations affected the observed growth mode. All four surfaces were, however, exposed to normal atmospheric conditions prior to vacuum insertion. An Fe island size independence on these four vastly differing CaF_2 substrates implies that CaF_2

growth conditions and 3-mm disc preparations are not responsible for the observed Fe film morphology. The deposition of a less reactive material (i.e. Ag or Au) on any of these surfaces, or the *in situ* production of a true $\text{CaF}_2(111)$ surface is necessary to more fully determine the involved growth mechanisms. As such, silver has been deposited with various coverages on room-temperature CaF_2 substrates and is discussed in a following section.

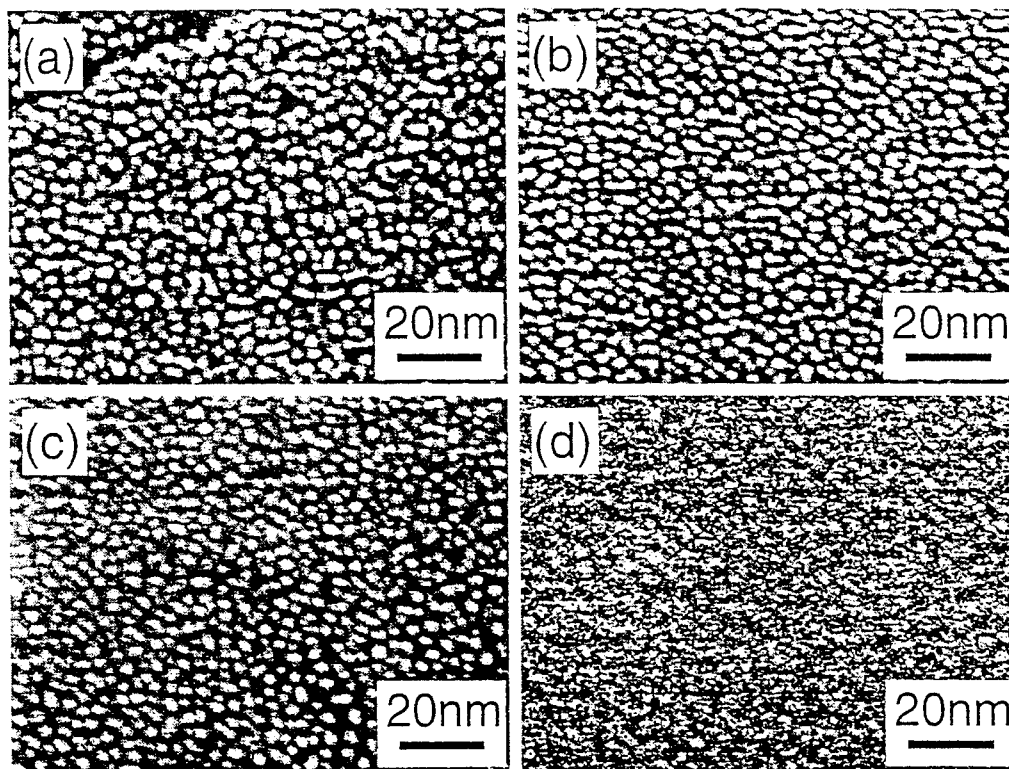


FIG. 2.3. Room temperature, ~ 7.5 ML Fe growth on (a) 10-nm thick relaxed, (b) 10-nm thick unrelaxed, (c) 800-nm thick relaxed, and (d) bulk $\text{CaF}_2(111)$ surfaces. The nucleation density is nearly equal for all four surfaces, therefore the observed nucleation density is not dependent upon specimen preparation. Due to specimen charging, image (d) has a poor signal-to-noise ratio compared to the thin film samples (a)-(c).

The stable state of a large ferromagnetic crystal, in the absence of an applied magnetic field, is characterized by magnetic domains arranged such that the magnetic flux lines are contained almost entirely within the specimen. This multiple domain configuration minimizes the total energy of the magnetic system. As the dimensions of a magnetic specimen are reduced, surface energies contribute more to the total energy of the system than do volume energies. Therefore, magnetic measurements performed on the Fe/ CaF_2 /Si(111) system with ~ 2 -nm diameter Fe islands are expected to reveal magnetic properties unlike those obtained from bulk, ferromagnetic samples. These properties may include increased coercivity and permanent saturation magnetization. Since domain boundaries no longer exist, high coercivity may result because spin rotation is required to change the magnetization of a specimen. This is due to the inhibition of spin rotation motion by anisotropy forces, which are typically much larger than the forces which oppose domain boundary motion. In addition, the single-domain particles individually behave as if magnetized to saturation in one direction. An array of single domain, ferromagnetic particles (above a critical temperature) can behave magnetically similar to moment-bearing atoms which display Langevin paramagnetism. This is termed superparamagnetism because the single-domain particles are composed of as many as 10^4 individual atoms with their own magnetic moments. The summation of these moments may result in a total particle moment more than 10^4 times that of an isolated atom. The temperature at which

thermal stability of the superparamagnetic moments is compromised (such that the majority of moments are no longer magnetically aligned) can be approximated by setting $k_B T$ equal to μH , where k_B is Boltzmann's constant, T is the temperature, μ is the magnetic moment of the single-domain particles, and H is the applied magnetic field. An array of single-domain particles should exhibit paramagnetic hysteresis loops when observed above this temperature.

The ~2-nm diameter Fe islands for the Fe/CaF₂/Si(111) system are composed of approximately 178 atoms, assuming a hemispherical shape and a mass density ($\rho_m = 7.87 \text{ g/cm}^3$) similar to that of bulk Fe. If a magnetic moment of 2.2 Bohr magnetons (μ_B) is assumed for each Fe atom in each island, a total moment of $392\mu_B$ results. Therefore, a temperature above 26 K thermally destroys the magnetic ordering of the particle array for fields up to 1 kOe. It is for this reason that room-temperature ferromagnetic behavior cannot be observed for this system. Our *in situ* characterization facility does not allow for low-temperature magnetism studies of surfaces, hence low-temperature measurements were not performed.

The islands observed in Figs. 2.1, 2.2(a) and 2.3(b) are smaller than the critical single domain size and separated by less than the mean free path of conduction electrons in metals (near 30 nm at room temperature for Cu). These properties make this system of nanometer-sized Fe islands on an insulator, when covered by a noble metal, an excellent candidate for room-temperature giant magnetoresistance (GMR) studies. In addition, if the Fe island diameters could be controlled so that all of the particles are of equal magnetic moment, then the magnetization curve could be fit to the Langevin function. Upon inserting the SE microscopy-determined volume of the islands into the Langevin paramagnetism equation, the magnetic moment per island could be calculated along with the average moment per Fe atom. A comparison could be made from this as to whether the average moment per Fe atom is correlated with that of a free ($4\mu_B$), a surface ($3\mu_B$), or a bulk ($2.2\mu_B$) Fe atom. For example, a 2-nm diameter island, where a 0.2-nm thick shell is considered as the surface, is composed of approximately 50% bulk atoms and 50% surface atoms. Since surface atoms tend to exhibit a higher magnetic moment due to a decreased coordination number, the resulting island structure should have a correspondingly higher total moment when composed of a high percentage of surface atoms. Due to the nature of the Fe/CaF₂ growth mode, hemispherical Fe island size was not controllable within a useful range. The onset of a measurable paramagnetic signature occurred for 7 ML Fe films. These islands appeared hemispherically shaped, while surface structures produced from depositions greater than 10 ML began forming into "meandering" islands rather than larger hemispherical particles. The formation of "meandering" islands does, however, allow for a comparison between the average island area and the corresponding Kerr signal. A surface composed of "meandering" islands, as compared to discrete 2-nm diameter islands, should exhibit a larger Kerr signal. This is due to the availability of more Fe atoms on the surface which can produce a Kerr rotation and also a greater average moment per island thus providing stability against thermally induced magnetization fluctuations.

Five of the surfaces shown in Fig. 2.2 were analyzed for magnetic behavior using SMOKE. All five films were analyzed in both the 1F and 2F modes. In addition, the dc reflectivity level was monitored for each surface in both the 1F and 2F modes. The dc level must be known so that the resulting Kerr intensities can be normalized amongst themselves and quantitative comparisons can be made. For example, two identical substrates with similar island size distributions but with a different quantity of islands per unit area would yield dissimilar Kerr intensities. This is not due to a larger magnetic moment per island, rather, it is due to a greater number of islands from which the Kerr signal was obtained. Correspondingly, identical film morphologies on (1) a highly reflective substrate and (2) a completely transmissive substrate would yield different Kerr intensities because a highly reflective surface can redirect the scattered light back through the islands and to the detector, unlike the non-reflective surface. Since the Kerr rotation is additive, the signal is compounded with each successive pass through the magnetic medium and is independent of the propagation direction. In fact, suitable coverages of nonmagnetic films on magnetic underlayer films result in an enhanced Kerr rotation due to constructive interference. This has often been

misinterpreted as an enhanced magnetic moment of the magnetic layer rather than an interference effect. Computer simulations are necessary to calculate the effects of nonmagnetic overlayers deposited on magnetic thin films. A similar condition results for the growth of magnetic films on multilayered substrates such as Fe on $\text{CaF}_2/\text{Si}(111)$.

Qualitative comparisons can still be made between Fe film coverage and the corresponding magnetic behavior. Figure 2.4 displays the polar and longitudinal Kerr signals for five different Fe coverages measured in the 2F mode. Figure 2.5 displays the Kerr loops which resulted in the 1F mode on four of the surfaces. Both modes exhibit a superparamagnetic signal in the polar and longitudinal geometry for Fe coverages up to 20 ML. The superparamagnetic signal is indicated by a linear variation in the Kerr signal with applied magnetic field. Coverages near 7.5 ML [Figs 2.4(a), 2.4(b), 2.5(a), and 2.5(b)] are weakly magnetic and result in noisy, yet unmistakable magnetic signals. Greater coverages yield stronger Kerr signals because (1) more Fe is available to produce a Kerr rotation and (2) thermally-induced magnetization fluctuations are further reduced by the effects of a larger average moment per Fe island. The polar and longitudinal Kerr signals are both observed to increase in strength with subsequent Fe evaporations [i.e., see Figs. 2.4(c)-2.4(f) and 2.5(c)-2.5(f)]. Near 30 ML, however, the film displays complex magnetic behavior. This is evident by the square hysteresis loop superimposed on a hard-axis signal in Fig. 2.4(g). Therefore, the onset of ferromagnetism for room-temperature grown Fe on $\text{CaF}_2/\text{Si}(111)$ occurs for coverages slightly less than 30 ML. The hard-axis behavior is probably a result of anisotropy effects within the ferromagnetic regime rather than superparamagnetic effects. If part of the film were superparamagnetic, then both the polar and longitudinal Kerr signals should increase (decrease) with large positive (negative) applied fields just as in Figs. 2.4(a)-2.4(f). The ferromagnetic easy-axis is within the surface plane since the longitudinal Kerr signal of Fig. 2.4(h) saturates near 200 Oe. A similar condition holds for the 1F mode Kerr loops displayed in Figs. 2.5(g) and 2.5(h). In the 1F mode, however, the ratio between the polar and longitudinal Kerr signals is different than for the same film measured in the 2F mode. Therefore, the resultant loops appear different in their slopes towards saturation as a result of the different sensitivities to the Kerr signals in the different modes.

The 1F and 2F polar and longitudinal Kerr loops in Figs. 2.4 and 2.5 were fitted with straight lines where the slope is proportional to the zero field susceptibility in the superparamagnetic regime. Only films that were superparamagnetic (less than 20 ML of Fe) were used. The dc reflectivity fluctuated by about 10% as a result of changes in the scattering intensities from differing surface topographies. The vertical error bars represent our uncertainty in the magnetization measurement while the horizontal error bars represent a distribution of Fe island cross-sectional areas. Figure 2.6(a) illustrates the linearity with which the effective magnetic moment per island increases as a function of Fe island area indicating that the effective moment is proportional to the average Fe island area for coverages greater than ~ 7.5 ML. The solid lines are linear regressions to the data points. In comparison, a plot of this data versus volume (i.e., three-dimensional islanding assuming a hemispherical shape) results in a non-linear effective moment dependence. Therefore, these magnetic measurements substantiate the previously reported statement that Fe island growth proceeds two-dimensionally rather than three-dimensionally for coverages exceeding ~ 7.5 ML. The linearity of the superparamagnetic response is due to the linearity of the Langevin function for small values of $\mu_{\text{eff}}H/k_B T$ (the Langevin function is proportional to $\mu_{\text{eff}}H/3k_B T$). A comparison between the 1F, 2F, polar, and longitudinal modes in Fig. 2.6(b) reveals that all four measurements give a linear zero field susceptibility dependence on the average Fe island area. The four data sets do not fall on the same line (with the same slope) because relative Kerr intensities between the different modes were not accounted for. In addition, birefringence effects due to the UHV window, light scattering off the small hemispherical islands, and inhomogeneous surface effects cannot be easily quantified. However, the salient feature of Fig. 2.6 remains unambiguous. The effective magnetic moment is linearly dependent upon the average Fe island cross-sectional area, and thus two-dimensional Fe island growth (for coverages exceeding ~ 7.5 ML) is evident from both the magnetic analysis and particle statistical analysis.

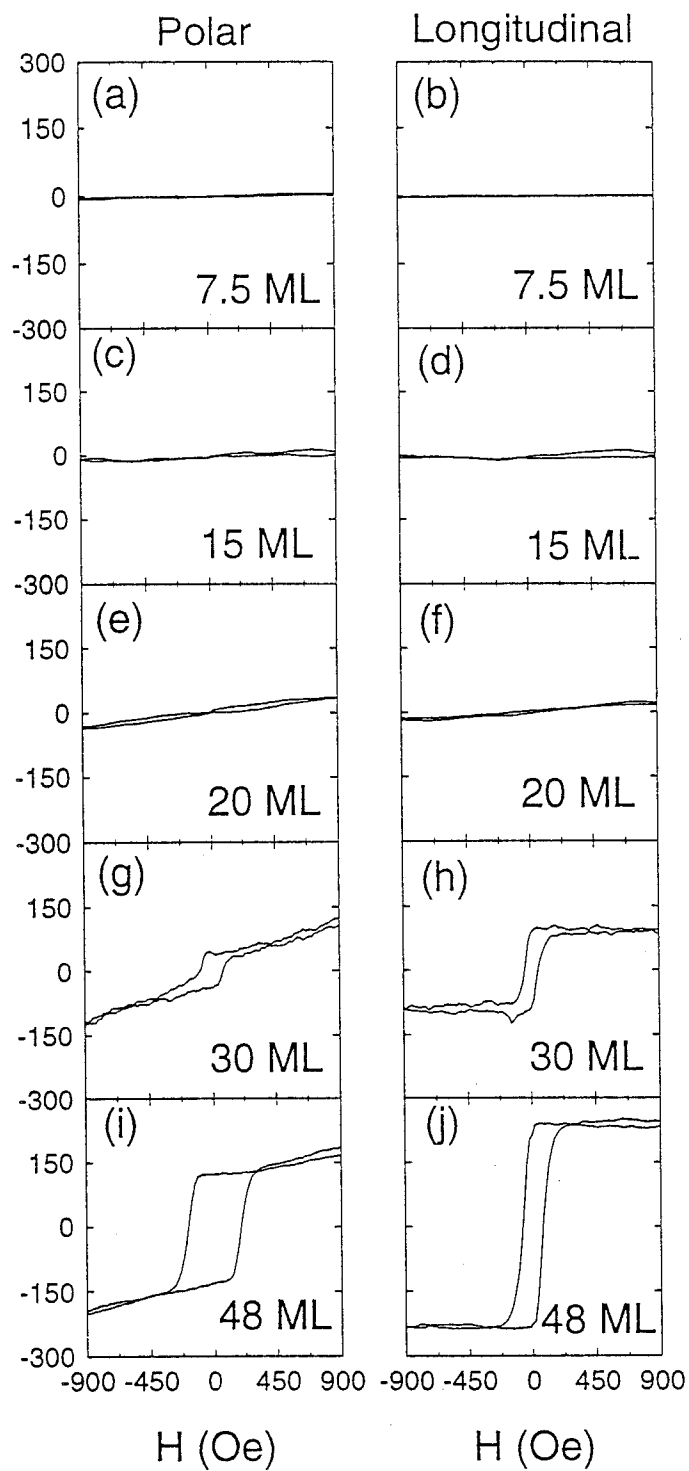


FIG. 2.4. Polar and longitudinal Kerr loops for various Fe coverages when measured in the 2F mode. All loops are on the same scale.

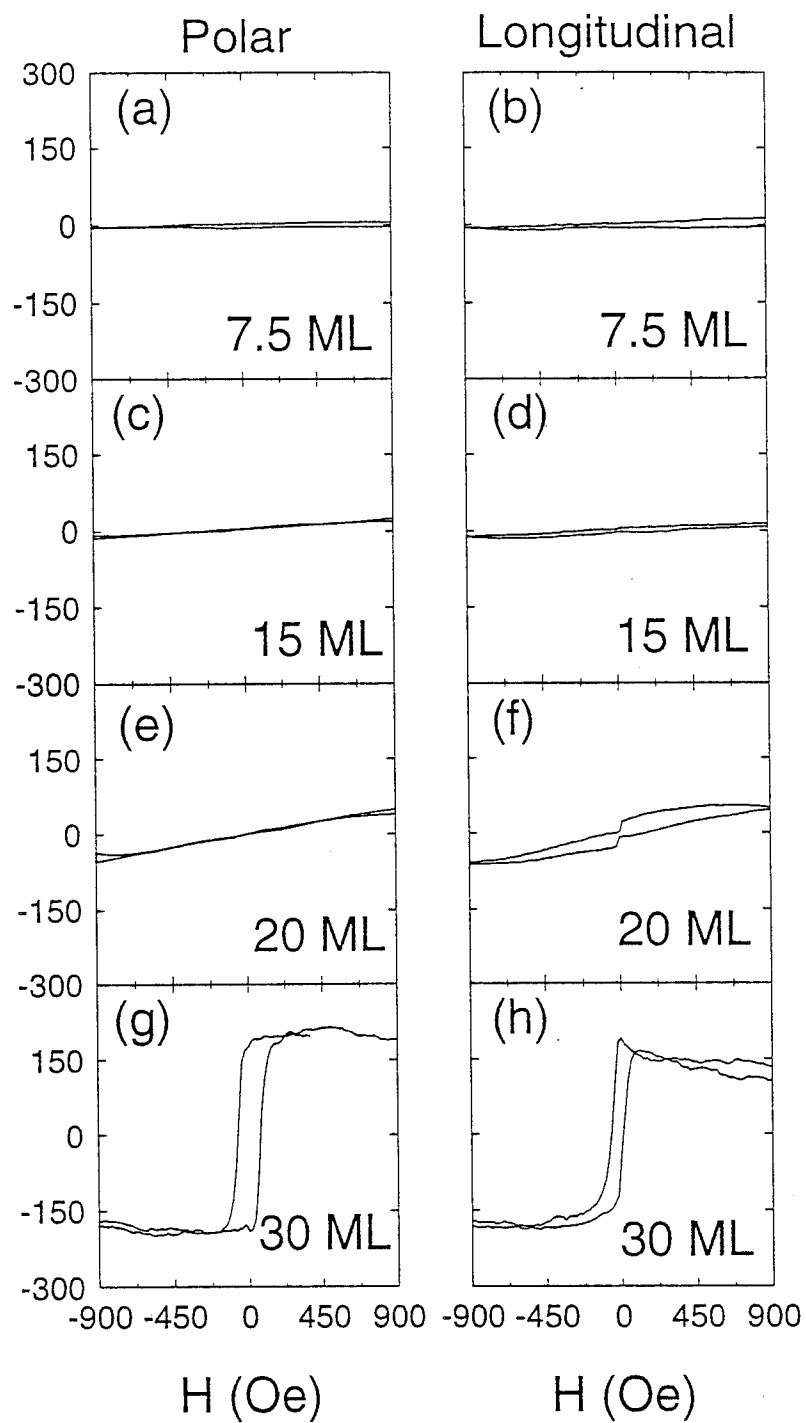


FIG. 2.5. Polar and longitudinal Kerr loops for various Fe coverages when measured in the 1F mode. All loops are on the same scale.

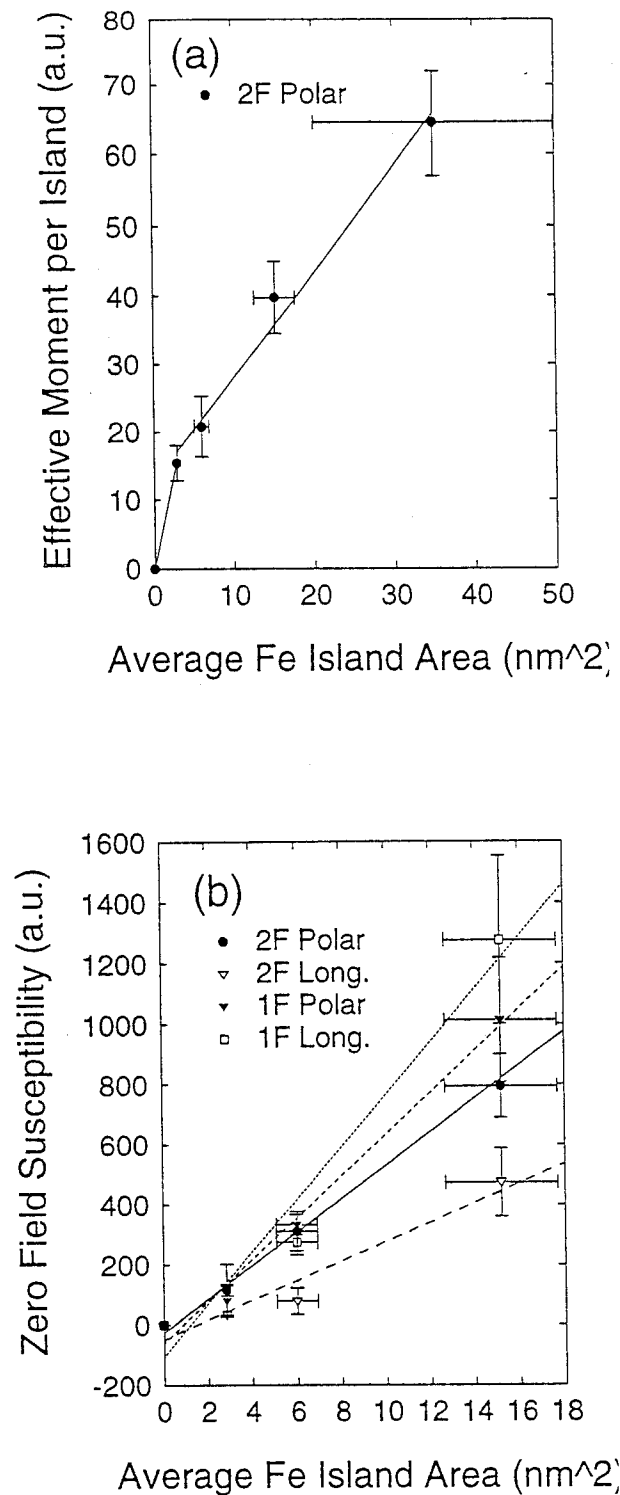


FIG. 2.6. Effective magnetic moment per island (a) and zero field susceptibility (b) as a function of average Fe island area.

We have developed a FORTRAN program which calculates all four Fresnel reflection and transmission coefficients for a multilayered system. The model, which was adapted from the work of Yeh, is able to calculate the plane-wave propagation of electromagnetic radiation in an arbitrarily layered birefringent

medium. This program is capable of predicting the Fresnel reflection coefficients for the Fe/CaF₂/Si(111) and Ag/Fe/CaF₂/Si(111) systems. Once the Fresnel coefficients are calculated they may be incorporated into a generalized Kerr intensity expression. Since the incidence angle is 45° from the surface normal, the resulting Kerr loops may provide information about the magnetic response both in-plane and out-of-plane for all three Kerr geometries (polar, longitudinal, and transverse). The ratio of the calculated Kerr intensities for the polar and longitudinal signals can be used to determine whether the magnetic anisotropy of the specimen is directed out-of-plane or in-plane. A similar comparison between the 1F and 2F modes can be made.

The utility of this model is hampered by the complexity of the Fe/CaF₂ system. Since the initial stages of growth favors island formation followed by "meandering" island formation, the scattering geometry changes as growth proceeds. Suitable corrections for island growth could be incorporated into the dielectric matrices but the varying island shape hinders its practicality. Therefore, non-uniform distributions of overlayers produce errors in our calculations. Nonetheless, our calculations provide a basis for observing the intensity reflectivity, Kerr rotation, and modulated Kerr intensity trends as a function of deposition coverage.

The program was used to calculate the intensity reflectivity, Kerr rotation, and modulated Kerr intensity for the polar and longitudinal Kerr geometries in both the 1F (1 ω) and 2F (2 ω) modes for 632.8 nm light arriving at a 45° angle of incidence. In both the polar and longitudinal geometries the reflectivity of s-polarized light is greater than that of p-polarized light. The polar Kerr rotations are less than 10 milliradians for a 50-nm thick Fe film while the longitudinal Kerr rotations are only 1/5 this value. Since the Fe film morphology is not constant with deposition (hemispherical then "meandering") we will define 1 ML of Fe as being 0.2 nm thick. Therefore, with this assumption, a 7.5 ML Fe film is 1.5 nm thick and provides a polar and longitudinal Kerr rotation of approximately 1 and 0.15 milliradians, respectively. Noisy Kerr signals typically result for these films because of the very small polarization rotations provided by the ultrathin magnetic films. The modulated Kerr intensity for the 1F polar geometry is stronger than the 2F mode until a thickness of 30 nm is reached. At this point the 2F polar Kerr signal becomes the dominant signal. These non-intuitive results signify the importance of modeling magnetic thin films systems with our magnetic-multilayer program.

A similar calculation was performed for various Ag coverages on a 1.5-nm (7.5 ML) thick Fe film on a 10-nm thick CaF₂ film on a semi-infinite Si substrate. The results of these calculations are illustrated in Figs. 2.7(a)-2.7(f). In this case the reflectivities increased while the Kerr rotations decreased with Ag coverage. This is expected because Ag is more reflective than Fe. The increased reflectivity also diminishes the amount of light which may reach the Fe islands, and hence the Kerr rotation is subsequently reduced with greater Ag overlayers. The trends in the modulated Kerr intensities, however, are not intuitively obvious. In the polar geometry [Fig. 2.7(e)] the 1F mode modulated Kerr intensity decreases monotonically with coverage while the 2F mode increases sharply at ~10 nm but decreases quickly thereafter. In contrast, the longitudinal geometry [Fig. 2.7(f)] provides a weaker Kerr signal and exchanges the roles of the 1F and 2F modes (i.e., the 2F mode monotonically decreases and the 1F mode reaches a maximum at ~10 nm).

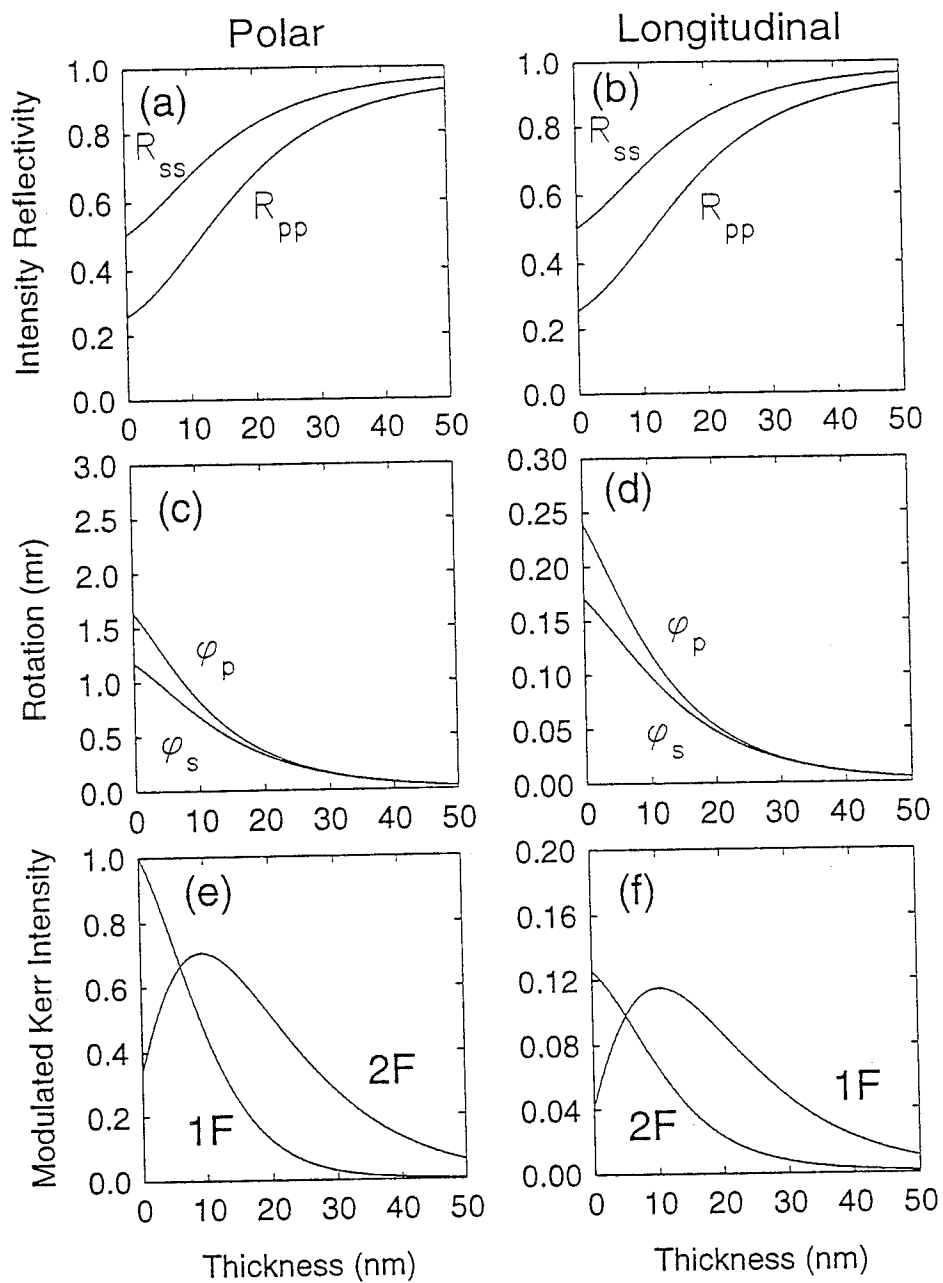


FIG. 2.7. Calculated reflectivities, Kerr rotations, and modulated Kerr intensities for various Ag coverages on a 1.5 nm Fe/10 nm CaF_2/Si substrate.

3.0 Ag/Fe/CaF₂/Si(111)

Silver was deposited on room-temperature CaF₂/Si(111) and Fe/CaF₂/Si(111) substrates so that comparisons in the growth modes between Fe/CaF₂, Ag/CaF₂, and Ag/Fe/CaF₂ could be made. Figures 3.1(a), 3.1(b), and 3.1(c) depict the film morphology for Fe_{10 ML}/CaF₂, Ag_{10 ML}/CaF₂, and Ag_{10 ML}/Fe_{7.5 ML}/CaF₂, respectively. The Fe islands in Fig. 3.1(a) are slightly larger than 2 nm in diameter and are very closely spaced. In contrast, an equivalent amount of Ag produces much larger, distantly spaced islands with a correspondingly greater size distribution than the Fe islands of Fig. 3.1(a). When a similar Ag deposition is performed on an Fe islanded substrate [Fig. 3.1(c)] the Ag tends not to form into large islands as observed in Fig. 3.1(b), rather, the Ag becomes more evenly distributed on a local scale just as the Fe is seen to do in Fig. 3.1(a).

The mechanism responsible for the Ag island formation displayed in Fig. 3.1(c) is that of surface energy minimization. Since $25 \pm 4\%$ of the CaF₂ surface is covered by Fe islands (for a 10 ML Fe deposition at room temperature), the Ag atoms tend to cover the higher surface energy Fe islands rather than the lower surface energy exposed CaF₂. As a result, the Ag atoms wet the Fe islanded surface much more than if no Fe was present. The formation of Ag islands, as shown in Fig. 3.1(b), which are much larger than the Fe islands formed from an equivalent amount of Fe may be due to several competing effects.

Silver atoms are relatively inert compared to Fe atoms. Therefore, the decreased probability of a Ag adatom being captured by an Fe-receptive chemical bond will decrease the nucleation density. Silver atoms also have a higher mobility than Fe atoms on most surfaces. The increased mobility is due to a smaller chemical reactivity. The Ag adatoms diffuse across the surface and are more likely to form larger, greatly spaced islands because of their smaller chemical reactivity.

Higher Ag adatom mobility due to a weaker chemical reactivity and no electron exposure during growth possibly increases the Ag island size distribution and decreases the nucleation density for similar coverages of Ag adatoms relative to those formed with Fe adatoms. Electron-beam generated surface defects are expected to be annealed out at elevated temperatures. This does not imply that Fe growth with simultaneous electron exposure at elevated temperatures should result in lowered nucleation densities if the defects are more readily annealed out. At higher temperatures the electrons may be more capable of generating defects due to a decreased desorption barrier which may be compensated for by a more efficient annealing process. As a result, the nucleation density may remain constant over a large temperature range, as has been observed in Fig. 2.1.

Due to the increased SE yield of Ag atoms (higher atomic number) compared to Fe atoms and the formation of larger Ag islands, Ag deposition of less than 2 ML can be easily observed with SE microscopy. The room-temperature deposition of 2.5, 10, 20, and 30 ML of Ag on CaF₂/Si(111) are displayed in Figs. 3.2(a), 3.2(c), 3.2(e), and 3.2(g), respectively. All of these surfaces exhibit round-shaped islands which are not uniform in size. At coverages near 30 ML the islands begin forming into faceted islands. An example of this is the six-sided and elongated island located near the center of Fig. 3.2(g). As a comparison, similar Ag coverages were deposited at room temperature on CaF₂/Si(111) which was previously coated with 7.5 or 10 ML of Fe. These four images are displayed in Figs. 3.2(b), 3.2(d), 3.2(f), and 3.2(h) next to the corresponding Fe-free surface with similar Ag coverage. In all four cases the Ag is shown to produce oddly shaped islands with a greater cross-sectional area as compared to the Fe-free, Ag islanded surfaces. The irregularly-shaped islands are also more uniformly sized and equally separated on all sides. This implies that the Ag adatoms are sufficiently mobile that small bands (~2-4 nm) of Ag-free regions can be maintained between the Ag islands.

Tables 3.1 and 3.2 list the island statistics for most of the surfaces shown in Figs. 3.2(a)-3.2(h). The statistics for Figs. 3.2(b) and 3.2(c) are not listed because the 2.5 ML Ag film was grown on a 10 ML Fe film (rather than 7.5 ML of Fe like the other three) and the 10 ML Ag/CaF₂ surface was prepared during a separate experimental run in which the deposition source was thought to be evaporating at an increased rate. Due to these uncertainties, these two data points have been omitted from the tables. In addition to the surface coverage, the average island size, and the island concentration are given. Table 3.2 reports the

average number of Fe islands covered by an average sized Ag island. The mean number of Fe particles covered by the Ag islands will be used to analyze the magnetic response of these films as observed by SMOKE.

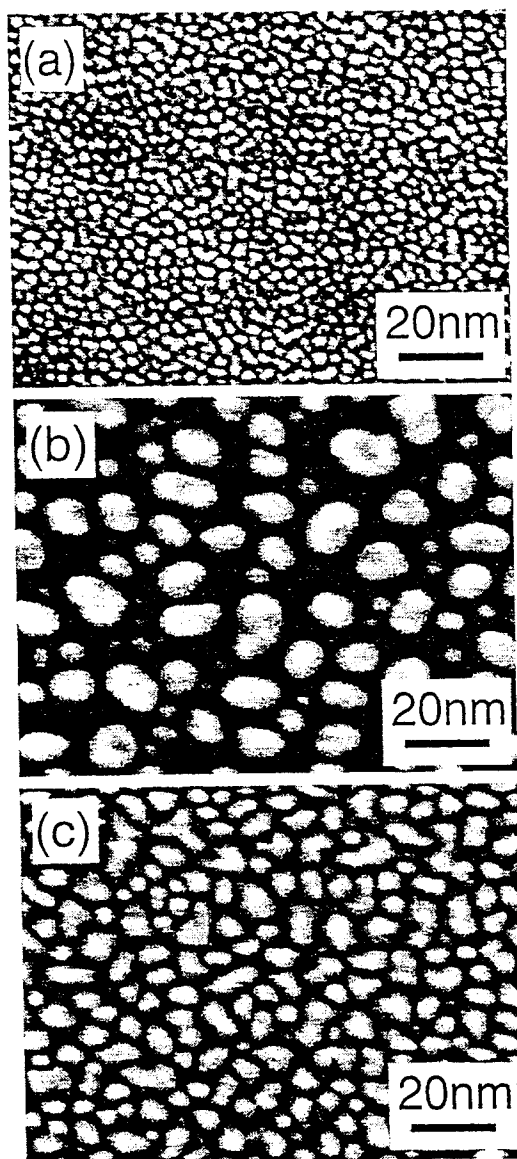


FIG. 3.1. Secondary electron images of three surfaces indicating the size and spatial distributions of (a) 10 ML Fe, (b) 10 ML Ag, and (c) 10 ML Ag/7.5 ML Fe grown at room temperature on 10-nm thick, unrelaxed CaF_2 .

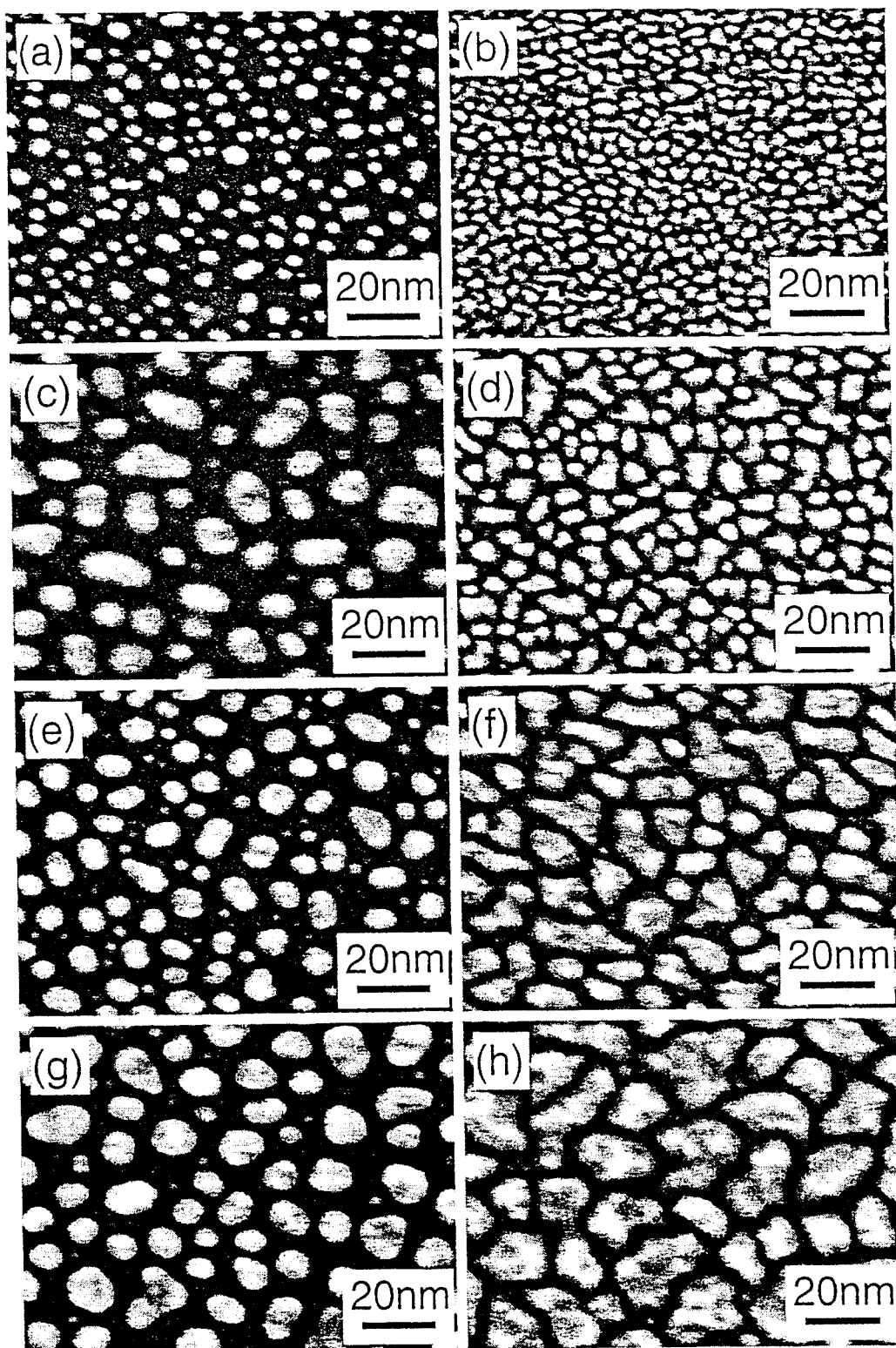


FIG. 3.2. Secondary electron images of Ag islands formed for room-temperature depositions on clean CaF_2 surfaces (left column) and 7.5-10 ML Fe/CaF_2 surfaces (right column). The CaF_2 surface is unrelaxed and 10 nm in thickness. The Ag coverages are (a)-(b) 2.5, (c)-(d) 10, (e)-(f) 20, and (g)-(h) 30 ML.

Table 3.1. Particle statistics for various coverages of Ag on 10-nm thick CaF₂ surfaces.

Ag Coverage (ML)	CaF ₂ Surface Coverage (%)	Average Ag Island Area (nm ²)	Number of Islands per Area ($\times 10^{-2}$ islands/nm ²)
6 \pm 3.5	22 \pm 1	9.63 \pm 0.88	2.59 \pm 0.43
20	34 \pm 2	27.9 \pm 2.1	1.23 \pm 0.15
30	43 \pm 2	46.4 \pm 6.5	0.93 \pm 0.17

Table 3.2. Particle statistics for various Ag coverages on 7.5 ML Fe/10 nm CaF₂ surfaces.

Ag Coverage (ML) on 7.5 ML Fe	CaF ₂ Surface Coverage (%)	Average Ag Island Area (nm ²)	Number of Islands per Area ($\times 10^{-2}$ islands/nm ²)	Average Number of Fe Islands beneath a Ag Island
10	38 \pm 2	18.4 \pm 1.4	2.06 \pm 0.27	3.47 \pm 0.67
20	50 \pm 2	64.0 \pm 1.9	0.78 \pm 0.05	9.18 \pm 1.12
30	61 \pm 1	126 \pm 15	0.48 \pm 0.07	14.8 \pm 2.9

For both the Ag/CaF₂ and Ag/7.5 ML Fe/CaF₂ systems, the number of Ag islands per unit area decreases with Ag coverage. This is a direct result of island growth where two or more closely spaced islands coalesce to form one larger island, hence the island population density decreases with evaporant coverage in this regime. This lends credence to the possibility of Fe-receptive chemical-bonding nucleation of Fe because the Ag does not grow into "meandering" islands like the Fe does. 1.6 times more Ag is needed to cover a bare CaF₂ surface than one which has a uniform distribution of ~2-nm diameter Fe islands. This results from the Fe islands which are spatially fixed and spaced less than 4 nm apart (between island centers), and have a higher surface energy than the CaF₂ substrate. The Ag adatoms nucleate on the individual Fe islands because of the high surface energy difference between Fe and CaF₂. Since the Fe islands are immobile and closely spaced, the Ag islands eventually coalesce into larger islands with continued depositions. As a result, the larger Ag islands cover several ~2-nm diameter Fe islands. If the Fe was not present, there would be fewer initial nucleation sites and correspondingly longer surface diffusion lengths leading to the formation of larger three-dimensional islands, hence less surface area would be covered.

Various amounts of Ag were deposited on a 7.5 ML Fe/10 nm CaF₂/Si(111) substrate to monitor the change in magnetic behavior as a function of Ag coverage. As is evident from Figs. 3.2(b), 3.2(d), 3.2(f), and 3.2(h), the number of Fe islands covered by a single Ag island increases with Ag coverage. Therefore, if the effective magnetic moment increases with Ag island size then the Ag atom conduction electrons must mediate the magnetic interaction of the enclosed Fe islands. This is a form of mediated-exchange. For ferromagnetic-like long-range exchange, the effective moment should increase as more Fe islands are enclosed within the Ag islands because $\mu_{\text{eff}}H$ is a larger percentage of $k_B T$. For antiferromagnetic-like mediated-exchange the effective moments would decrease and if no long-range exchange is present then the effective moment would remain unchanged as a function of Ag island size.

2F polar and longitudinal Kerr loops for the Ag/7.5 ML Fe/10 nm CaF₂/Si system (by definition 7.5 ML is equivalent to 1.5 nm) were acquired. The peak-to-peak superparamagnetic signals were averaged for both the polar and longitudinal geometries. This gives an average modulated Kerr intensity for each surface in both SMOKE geometries. The modulated Kerr intensities from the Ag coated surfaces, however, represent the magnetic signature from both covered and uncovered Fe islands. The magnetic signal from the uncovered Fe islands must be subtracted from the total magnetic signal in order to correctly compare effective magnetic moments as a function of Ag coverage. The amount of Kerr signal subtracted for the Ag-coated surfaces is determined by the fraction of uncovered surface area (no Ag

islands) multiplied by the Kerr signal for an uncovered Fe islanded-only surface. The uncovered surface area for each Ag deposition is 1.00 minus the CaF_2 surface coverage listed in the Tables. The amount of Kerr signal from only the uncovered Fe islands is subtracted from the total Kerr intensity for the three Ag-coated surfaces, therefore, the Kerr signal for only Ag covered islands results. These values must be compared to the corresponding magnetic signal from just the Fe islands within the same cross-sectional area. The uncovered Fe island signal is proportional to the percentage of surface area covered by Ag islands times the magnetic signal for an Fe islanded-only surface. In this fashion, equivalent total areas are compared for Ag-covered and Ag-uncovered Fe islands. A plot of this data is depicted in Fig. 3.3(a). A similar graph is shown in Fig. 3.3(b) with the adjustments for the changing optical scattering coefficients. The adjustments are necessary because the Kerr signal diminishes slightly with Ag coverage due to an increased reflectivity. This has already been discussed earlier and is evident from Figs. 2.7(a)-2.7(f).

The two graphs of Fig. 3.4 reveal the increased effective magnetic moment as a function of Fe islands contained within an average Ag island (related to cross-sectional area and listed in the Tables). Since equivalent areas of Ag-covered and Ag-uncovered Fe islanded regions were compared, the slope of the curves for both polar and longitudinal Kerr would be zero if the Ag did not mediate the magnetic exchange between Fe islands enclosed within a Ag island. In both the optically uncorrected [Fig. 3.3(a)] and optically corrected [Fig. 3.3(b)] plots, the longitudinal Kerr intensity increases with the number of Fe islands. This signifies that the Ag atoms *do* help correlate the in-plane magnetic moments between individual Fe islands contained within a single Ag island. If the long-range exchange mechanism completely coupled the moments within the Fe islands covered by a Ag island, the slope of this line would be exactly one. The corrected longitudinal signal of Fig. 3.3(b) gives a slope of 0.25 rather than 1.00. In comparison, the corrected polar signal has zero slope within the measurement uncertainty. Since the in-plane slope is unmistakably present while the out-of-plane signal is absent, this suggests that the Ag atoms induce an in-plane anisotropy which favors in-plane magnetic alignment. An explanation for a non-unity slope in the longitudinal Kerr effect may be due to the increased Fe atom coordination number. Since Fe surface atoms have a higher magnetic moment than bulk atoms, the Ag coating may have reduced the moments of Fe atoms existing on the Fe island surfaces. Assuming that originally 50% of the Fe atoms are surface atoms (with a magnetic moment of $3\mu_B$), while the remainder are bulk ($2.2\mu_B$), implies that the slope of the effective magnetic moment versus number of Fe islands should decrease by only 15% $[(1.0)(2.2)/\{(0.5)(3) + (0.5)(2.2)\} = 0.85]$ rather than the observed 75%. Even if all the atoms within an Fe island are considered as surface atoms the slope would only decrease by 27% $[(1.0)(2.2)/(1.0)(3) = 0.73]$. Therefore, the effect of an increased coordination number does not completely account for the non-unity slope in the longitudinal geometry. A weakened super-exchange mechanism may be responsible for part, or all of, the missing longitudinal moment. Since super-exchange mechanisms are dependent upon the spatial separation of magnetic moments, it is possible that the Fe islands are separated by a distance that does not allow the Fe island moments to completely orient themselves relative to each other when covered by an individual Ag island. For example, in the RKKY interaction the exchange constant oscillates with magnetic moment separation. Therefore, two moments may be aligned, anti-aligned, or unaligned depending on the separation. A mechanism such as this is probably responsible for the missing longitudinal magnetic moment.

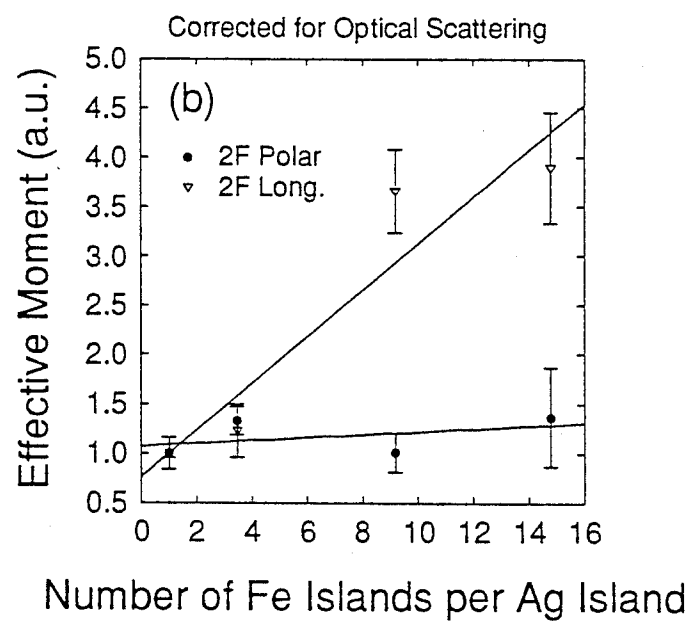
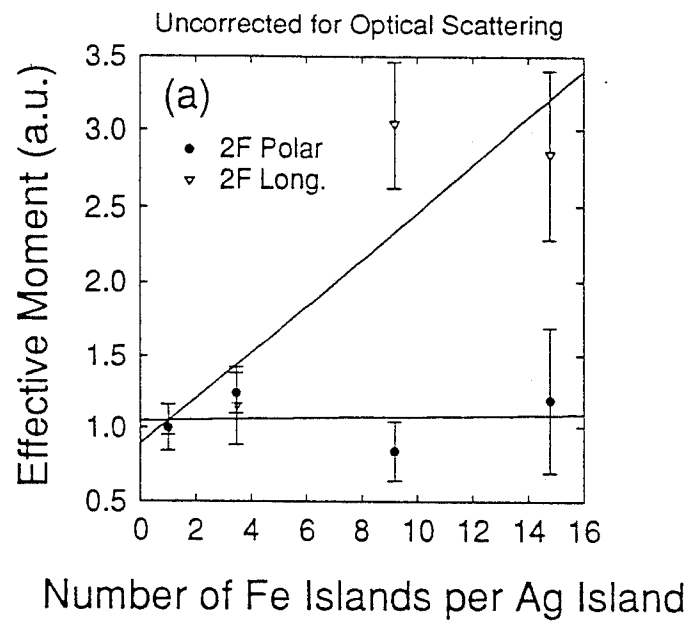


FIG. 3.3. Optically uncorrected (a) and corrected (b) effective magnetic moment as a function of Fe islands contained within an average Ag island.

4.0 [Co/Cu]_n/Co/Si(100)

Oscillatory exchange coupling across Cu interlayers has attracted considerable attention from both the fundamental and application viewpoint. The relatively simple nature of the Cu Fermi surface makes Cu a suitable candidate for the verification of exchange coupling theories. We have prepared [Co1.5nm/Cu_t]_n (7<n<13) superlattices by evaporating on Si(100) oriented crystals, Corning cover glass slides and holey carbon film covered grids. 6.0 nm thick Co layers were grown at 250°C as buffer layers on the substrates. It was found that use of a buffer layer gave the best GMR properties. Our STEM and LAXS results of pure Co thin films indicates that the 6.0 nm thick Co buffer layer will lead to flat Co and Cu layers. 4.5 nm thick Co capping layers covered the superlattices, making the sandwich symmetric. The total superlattice thickness ranged between 40 and 46 nm sufficiently thin so as to be electron transparent to 100 KeV electron beams so that we can characterize the magnetic microstructure using electron holographic methods. All films were grown at room temperature in a dual e-beam UHV evaporation system. Deposition rates were 0.3~1Å/sec at a base pressure 5×10⁻⁹ mbar. A growth pressure of 5×10⁻⁸ mbar can be maintained with a low growth rate of 0.3Å/s. In-situ thickness calibration using a quartz crystal microbalance was confirmed with Rutherford backscattering.

The x-ray spectra were measured using a Rigaku D/Max-II diffractometer with Kα radiation from a fixed Cu anode. The θ-2θ scan speed was typically 0.5°/sec with steps of 0.004° for Small Angle X-Ray Scattering (SAXS) and 4°/sec with steps of 0.02° for Large Angle X-Ray Scattering (LAXS). The Large Angle X-Ray Scattering (LAXS) data, as shown in Fig. 4.1(a), are characterized by a fcc (111) Co (Cu) peak indicating that the multilayers have a (111) out-of-plane texture. Some films show a very weak fcc (200) Co (Cu) peak. The peak positions shifted slightly from fcc (111) Co peak position (2θ=44.2°) towards the fcc (111) Cu peak position (2θ=43.5°) as the Cu spacer thickness increases. Fig. 4.1(b) shows the spacing d<111> vs the Cu spacer thickness t_{Cu}, showing d<111> increases as the Cu spacer thickness increases.

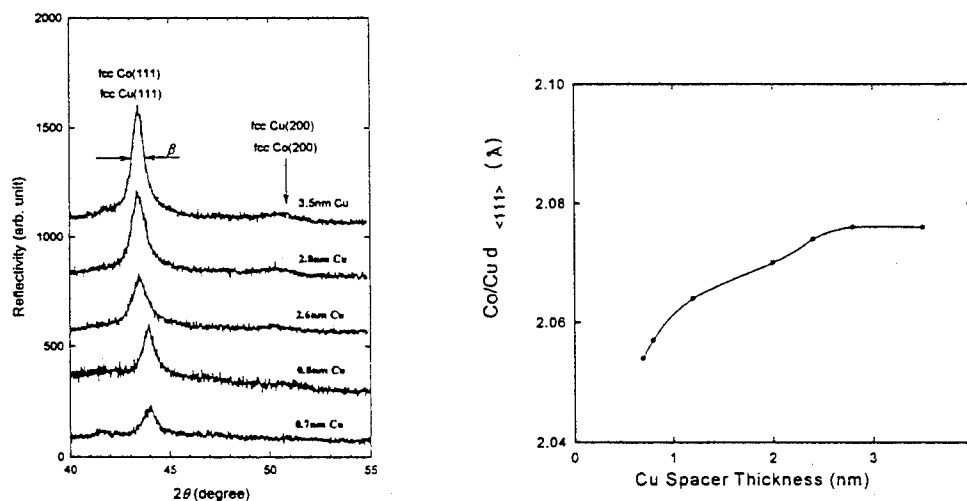


Figure 4.1(a) Large Angle X-Ray Scattering on superlattices of Si/[Co(1.5 nm)/Cu_t]_n, n is the bilayer number between 7-13. The Cu spacer thickness of all films and the fcc-Co, fcc-Cu peaks are marked. The FWHM β of fcc (111) is decreasing as a function of Cu interlayer thickness. (b) Atomic plane spacing d<111> vs the Cu spacer thickness (note that in pure Co and pure Cu crystal, d<111>_{Co}=2.048Å, d<111>_{Cu}=2.078Å) in the series of superlattices Si/[Co(1.5 nm)/Cu_t]_n (6<n<13), calculated from LAXS data.

The average grain sizes of the films calculated from the full width at half intensity (FWHM) β of the fcc (111) peak ranges between 10-14 nm. The FWHM β of the fcc (111) peak decreases from 0.8° - 0.6° as a function of increasing Cu interlayer thickness indicating an increase in grain size and fewer defects in the layer structures because of a smaller number of grain boundaries.

SAXS profiles of the superlattices are shown in Fig. 4.2(a). Only first order SAXS Bragg peaks with superlattice character Kiessig fringes were observed for the films with Cu interlayer thickness thinner than 1.2 nm indicating the presence of relatively rough interfaces and wavy layers. The rms-roughness of the interface estimated by fitting the SAXS spectra is ± 0.2 - 0.4 nm. Fig. 4.2(b) is the SAXS profile of the film with the structure of Si/Co(4.5 nm)/[Co(1.5 nm)/Cu(2.0 nm)]₈/Co(6.0 nm), together with an offset (for clarity) SAXS spectrum calculated with a standard dynamical scattering model (the simulation program was developed by M.R. Scheinfein). In order to match the spectral structures and damping rate, the interface roughness and layer spacing have to be correctly defined. The fits were simulated with a 2.0 nm SiO layer between Si substrates and the very first Co buffer layer, a 4.5 nm topmost CoO rough layer, and the interface roughness is ± 0.2 nm for the lower half of the superlattice stack, and ± 0.4 nm for the top half. Considering the roughness ± 0.2 - 0.4 nm estimated from the dynamical SAXS simulation program, the bilayer thickness is in good agreement with the nominal values with an error less than 5%. The observed broadening of the higher-order Bragg peaks and the disappearance of the high-order low angle amplitudes may arise from interfacial interdiffusion and cumulative random variations in layer thickness.

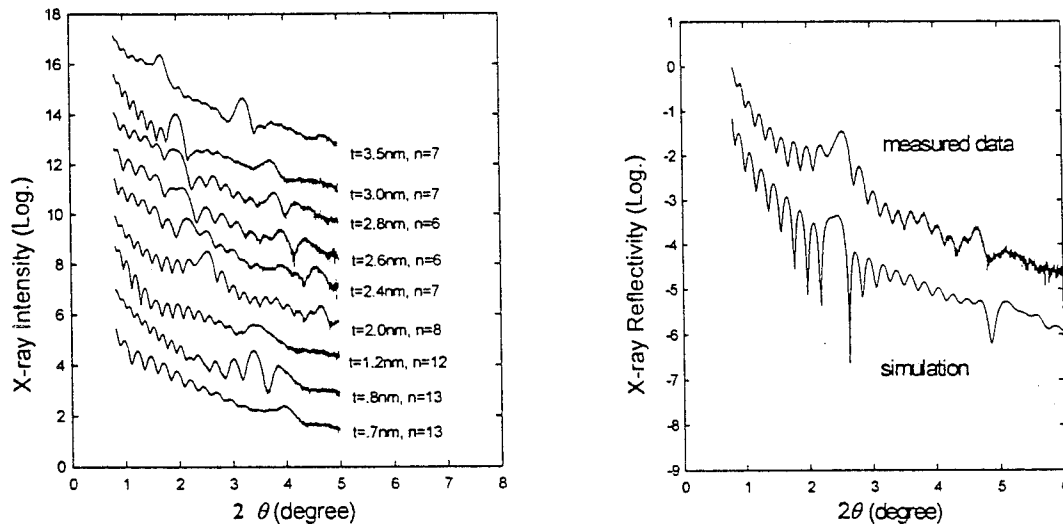


Figure 4.2 (a) SAXS measurements for the series of Si/Co(4.5nm)/[Co(1.5nm)/Cu]_n/Co(6.0nm) multilayers. The Cu interlayer thickness and the number of bilayers are marked for each film. (b) SAXS profiles of the superlattice with the structure of Si(100)/Co(4.5nm)/[Co(1.5nm)/Cu(2nm)]₈/Co(6nm). The top profile is measured data, and lower one is the simulation with the parameters given in the text.

Characterization methods based on the transmission electron microscope (TEM) enable the local microstructure of a material to be visualized directly in a manner that is not possible with bulk techniques such as x-ray diffraction and Rutherford backscattering. Diffraction contrast and defocussing techniques were used to study the presence of texturing and long-range orientational relationships. The successive layers of native oxide SiO (~2nm), Co buffer layer (~6nm), Co/Cu multilayer, and epoxy mount can be distinguished, illustrating clearly that the superlattice structures have sufficient quality to maintain separation of the layers. The TEM images showed that the layers are coherent over several hundred Å, which again is consistent with our x-ray diffraction data. The flatness and continuity of the layers does not support the view that the MBE and evaporation growth of (111)-oriented samples is particularly prone to pinhole formation. Typical interface roughness statistics extracted from TEM images are given in Tables 4.1 and 4.2.

Table 4.1 Multilayer Roughness Estimated from Profiles of TEM Image Line Scans for the Superlattice with a Nominal Structure Si(100)/Co(4.5nm)/ [Co(1.5nm)/Cu(2.0nm)]₈ /Co(6.0nm).^{*,**}

	position 1	position 2	position 3	position 4	Average
$\langle t \rangle_{\text{Co}} (\text{\AA})$	15.7	15.6	16	16	15.83
$\sigma^2 (\text{\AA})$	1.23	4.56	4.45	5.7	3.99
$\sigma (\text{\AA})$	1.11	2.13	2.1	2.4	1.94
$\langle t \rangle_{\text{Cu}} (\text{\AA})$	19.3	19.76	19.6	19.4	19.52
$\sigma^2 (\text{\AA})$	2.28	1.63	2.91	1.02	1.96
$\sigma (\text{\AA})$	1.51	1.28	1.71	1.1	1.4

Table 4.2 Multilayer Roughness Analysis for Each Individual Layer Estimated from Profiles of TEM Image Line Scans for the Superlattice with a Nominal Structure Si(100)/Co(4.5nm)/[Co(1.5nm)/Cu(2.0nm)]₈ /Co(6.0nm).^{*,**}

	line 1	line 2	line 3	line 4	$\langle t \rangle$	σ^2	σ
SiO	22	22	22	22	22	0	0
Co	60	57.7	58.4	57.1	58.3	1.57	1.25
Cu	20.7	19.6	19.82	18.32	19.61	0.96	0.98
Co	15.3	15.25	14.3	15.1	14.99	0.22	0.47
Cu	16.3	17.4	19.2	20.5	18.35	3.48	1.87
Co	14.2	13.1	15.4	11.9	13.65	2.24	1.5
Cu	18.5	21.8	18.72	20.5	19.88	2.44	1.56
Co	16.34	18.5	14.3	20.5	17.41	7.18	2.68
Cu	19.6	19.6	22	18.32	19.88	2.36	1.54
Co	17.4	14.2	18.7	16.2	16.63	3.66	1.91
Cu	20.7	19.6	17.6	19.4	19.33	1.65	1.29
Co	16.34	18.5	17.6	15.1	16.89	2.2	1.48
Cu	20.6	19.6	22	20.5	20.68	0.98	1
Co	16.34	16.3	18.7	17.24	17.15	1.26	1.12
Cu	18.5	20.7	17.6	18.3	18.78	1.8	1.34
Co	14.2	13.1	13.2	16.2	14.2	2.1	1.44

*All units for thickness are in Å, the average $t_{\text{Co}}=15.85 \pm 1.53 \text{\AA}$, $t_{\text{Cu}}=19.5 \pm 0.83 \text{\AA}$.

**Each position of line scans sampled is 5 Å apart to each other.

GMR and 90° Coupling Oscillation in Co/Cu Multilayers

We have shown that our Co/Cu multilayers are well characterized layered structures with interface roughness of ± 0.2 - 0.4 nm. All films show fcc (111) texturing with an average grain size of 10 nm and grain-to-grain epitaxial coherence. In order to investigate the origin of the GMR and coupling in these superlattices, we have carried out a study of the magnetic alignment within adjacent Co layers with the combined three-axis Magneto-Optical Kerr Effect (MOKE). In order to obtain the transverse in-plane component of the magnetization, M_y , both the sample and the magnetic field are rotated until both the easy-axis and the applied field direction are perpendicular to the scattering plane. Without modifying the position of any optical elements, calibrated M_x and M_y components of the magnetization can be recorded during the switching process. The components can be added together in quadrature as a measure of the total magnetization, M_s . When the normalized total magnetization differs from one, there are regions where the magnetization is misaligned. The misalignment can be due to domain formation within a given layer(s) of the superlattice, or may be due to small regions of anti-alignment between adjacent layers. It has been shown that the interfaces between Co and Cu get rougher with increasing distance from the substrate surface. In order to assess effects due to cumulative roughness in layered structures, Kerr effect hysteresis loops were measured from both sides of samples grown on glass substrates. No obvious difference was observed in hysteresis loops measured from the top or the bottom of the superlattice stack. Our TEM micrographs showed no obvious difference in roughness observed at the lower part of the superlattice stack and at the top of the stack near the surface because the total thickness of our superlattices is limited to below 50 nm and the number of bilayers limited to below 13.

The magnetoresistance (MR) was measured on both strip-shaped ($5 \times 8 \text{ mm}^2$) and patterned, dumbbell shaped ($5 \times 0.2 \text{ mm}^2$) Si(100)/Co(4.5 nm)/[Co(1.5 nm)/Cu(t)]_n/Co(6.0 nm) ($6 < n < 13$) superlattices. The oscillation period of interlayer coupling was about 1 nm (see the APL preprint in Appendix C for MR curves and MO hysteresis loops). The peaks in the 90° oriented magnetization correspond with the peaks in the magnetoresistance data at approximately t_{Cu} of 0.8, 2.0 and 2.8 nm. In all films examined, H_c was approximately 35 Oe. During the switching process, the magnetization reorients itself along a direction 90° from the easy axis and the field for Cu layer thicknesses where the MR is maximum. This is clear evidence that there is 90° domain formation in the superlattice which appears as 90° coupling (see APL).

Interlayer Coupling and Magnetotransport Mechanisms

A much debated issue concerns the appearance of giant magnetoresistance (GMR) in samples that show little or no evidence of antiferromagnetic (AF) interlayer coupling. It has been suggested that AF interlayer coupling may be masked in the Co-Cu (111) system by stacking faults and pinholes, and 90° coupling may arise from spatial nanoscopic fluctuations in the interlayer coupling through the non-magnetic spacer layer. Erickson et al. calculated antiferromagnetic (180° or bilinear) interlayer coupling constant A_{12} and biquadratic (or 90°) interlayer coupling constant B_{12} based on a free-electron model and found that both A_{12} and B_{12} oscillate with spacer-layer. The overall amplitude of B_{12} is generally smaller than that of A_{12} . The criterion for biquadratic coupling is $B_{12} < -|A_{12}|$. This may happen at the nodes of the A_{12} oscillation curves when A_{12} is near zero at certain regions of spacer-layer thickness. The AF coupling is sufficiently strong to overcome random coercive or pinning forces that oppose realignment within the magnetic layers only for ideal (perfect) layer structures. However, near the nodes where the AF coupling goes through zero and for large spacer thickness, the AF coupling is no longer

strong enough compared to the pinning forces to define uniquely the magnetic configuration of the multilayers.

The experimental data for the period of AF coupling oscillation in fcc (111) Co-Cu multilayers is about 5-6 ML. The magnitude of the coupling at the first AF coupling maximum is $A_{12} = 0.15-0.3 \text{ erg cm}^{-2}$ at $T=0$; this value decreases by roughly 10% at room temperature. For the same system (assuming a roughness parameter $\sigma \approx 0.25$), a theoretical calculation based on modified RKKY model gives the period $\Lambda \approx 4.5 \text{ ML}$, $A_{12} = 0.25 \text{ erg cm}^{-2}$ at $T=0$, and a 5% decrease of A_{12} at room temperature, which are in good agreement with the experimental data. It is reasonable for us to discuss the effect of roughness in our fcc Co-Cu (111) superlattices with imperfect interfaces by using the theoretical data from Bruno and Chappert, calculated for fcc Co-Cu (001) system ($\Lambda \approx 2.56$ and 5.88 ML for short- and long-oscillation) at $T=0$ and interfacial roughness $\sigma=0$. We apply the interfacial roughness of $\sigma \approx \pm 0.2-0.4 \text{ nm}$ extracted from TEM and SAXS data to our imperfect interface model. For a Gaussian distribution of interfacial roughness, the intensity and period of the interlayer coupling are to be modulated by convolution with a Gaussian function as

$$A_{12}(t, \sigma) = (\sigma\sqrt{2})^{-1} \int A_{12}(\xi - t) \exp(-\xi^2 / 2\sigma^2) d\xi$$

where t is the spacer-layer thickness. Fig. 4.3 shows results of our modeling where the solid line is the convoluted theoretical data from Bruno and Chappert for an ideal fcc Co/Cu superlattice, and A_0 is about 13 erg cm^{-2} . It can be seen clearly that the period of oscillation spreads out and the intensity of AF coupling is diminished as the roughness increases. The intensity of the coupling for an rms roughness of 0.2 nm is only 20% of that compared to the theoretical curve representing perfect layers with zero roughness. At this roughness (0.2 nm), very weak AF coupling appears at the Cu spacer thickness of $0.9, 2.0, 3.0$, and 4.0 nm , as shown in Fig. 4.3. This period is consistent with the accepted range of Cu spacer thickness indicating that the interfacial roughness and incomplete AF coupling should be considered in interpreting experimental data reported so far for Co/Cu superlattices. This weak AF coupling is totally masked at the roughness of 0.4 nm leaving the possibility for 90° coupling. Only after the interlayer AF (180°) coupling is masked by interlayer roughness, does the 90° coupling become dominant. This 90° coupling is the main reason for observing the GMR effect in our superlattices with imperfect interfaces.

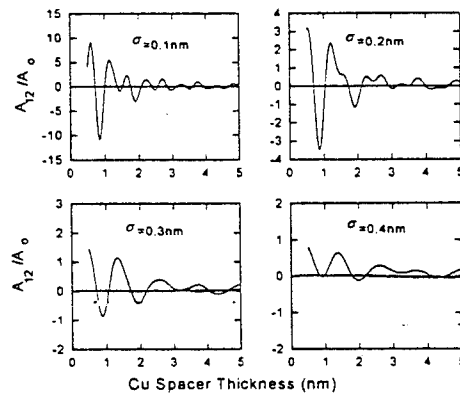


Figure 4.3 Oscillation curves of AF interlayer coupling constant A_{12} (normalized to A_0) for fcc Co-Cu multilayers as a function of the Cu spacer thickness showing that the intensity is diminished and the period spread out as the roughness increases.

In a simplest possible model, GMR values due to 90° coupling arising from interfacial roughness can be calculated using simple linear relationships as follows:

$$\left(\frac{\Delta R}{R}\right)_{measured} = \alpha \left(\frac{\Delta R}{R}\right)_{ideal}$$

We apply our 90° coupling factor α (M_y/M_s) plotted in Fig. 1 of the APL in Appendix C to the GMR data at room temperature from Mosca et. al. The modulated MR data in Fig. 4.4(c) fits very nicely with the experimental MR oscillation curve for our series of Co/Cu superlattices except that the value of the MR in our sample with Cu spacer thickness of 0.8 nm at the first oscillation peak is strongly suppressed. This modeling suggests that the principal reason why the magnetoresistance values of imperfect Co-Cu multilayers fall below some ideal value is the competition between the 180° coupling and the 90° coupling in the regions of AF coupling. This competition leads to the complicated magnetic configuration and domain structure of the superlattices. The effect of interfacial roughness on interlayer coupling masks the 180° coupling and gives rise to 90° domains. However, 90° coupling can not totally dominate (α is less 50% in our experiment) due to the small coupling constant. The coefficient $(1-\alpha)$ represents the degree of ill defined magnetization states at zero field in the regions where the AF coupling is masked. These ill defined magnetization states reduce $\Delta R/R$ primarily by decreasing the resistance of the zero-field state. The suppression of the MR value, at the first oscillation position in our superlattice with Cu spacer thickness of 0.8 nm having a wavy layered structure and very rough interfaces confirmed by TEM and SAXS measurements, implies that interface scattering is not favorable in the Co/Cu system to produce high values of MR. In contrast, GMR in Fe/Cr multilayers results from spin dependent interface scattering which leads to an increase in the MR value. As shown in Table 4.3, the resistance R_s at the saturation field increases as thickness decreases indicating that the suppression of MR values at the thinnest Cu spacer thicknesses in superlattices with rough interfaces is mainly caused by diffuse surface scattering and the increasing of the sheet resistance.

Table 4.4 Dependence of MR Values and Saturation Resistance R_s at Saturation Field H_s (14KOe) on Cu Spacer Thickness for Si(100)[Co(4.5nm)/[Co(1.5nm)/Cu(t)]_n/Co(6nm) with n from 6-13.

Cu spacer thickness t(nm)	R_s ($H_s=14KOe$) (Ω)	MR%
0.7	6.036	0.6
0.8	5.088	1.67
2.0	1.47	7.14
3.5	1.585	3.6

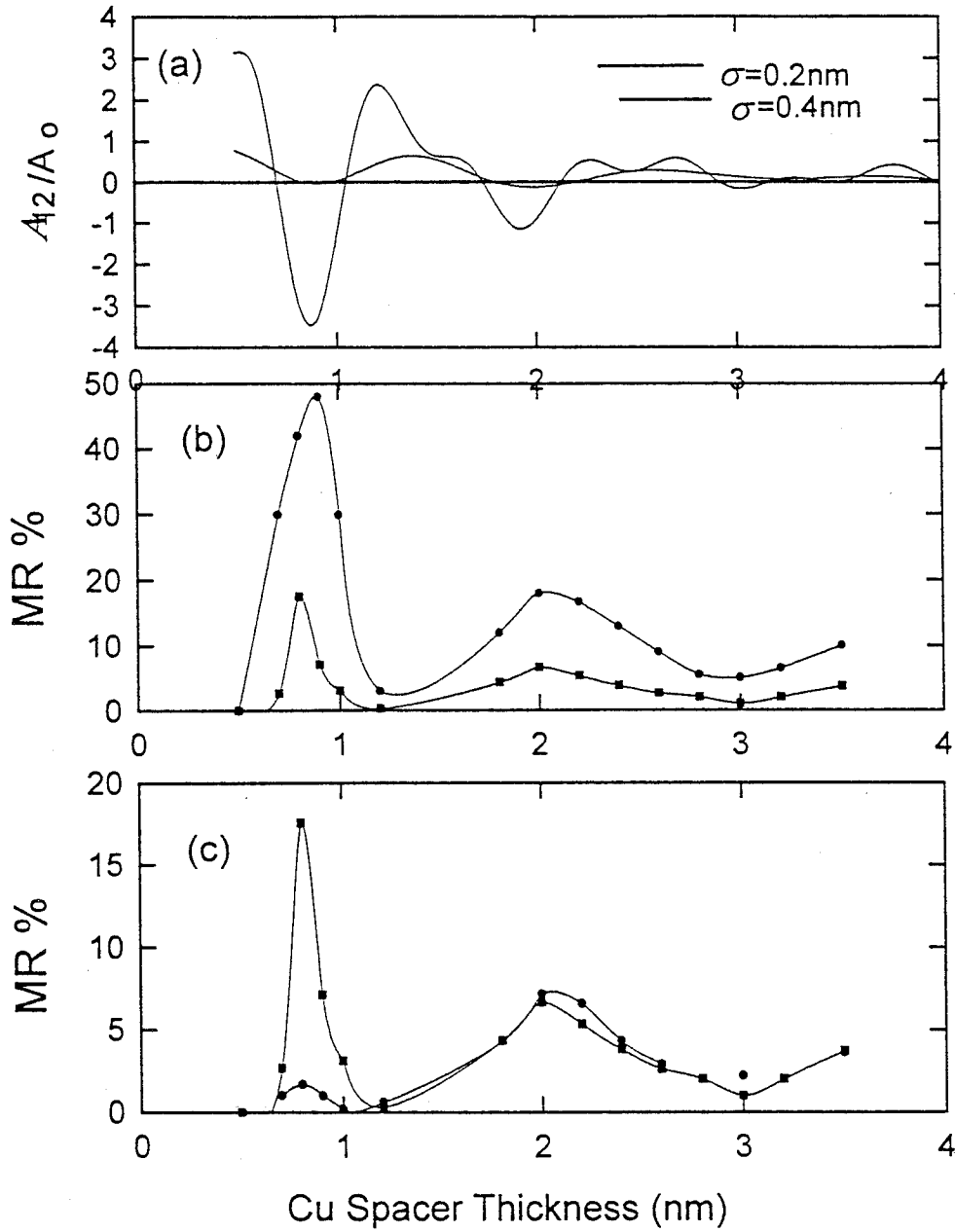


Figure 4.4 MR and coupling oscillation curves. (a) 180° coupling constant A_{12} with roughness of 0.2 and 0.4 nm; (b) The lower curve shows the calculated GMR and the upper curve is MR data at room temperature from Mosca et. al.; (c) Our experimental MR oscillation curve for Co/Cu at room temperature (lower) is compared with the calculated data (upper) from (b).

5.0 Electron Holography of Superlattices and Small Particles

We have developed the electron holographic technique as a means of performing absolutely calibrated micromagnetic measurements. In this section, we show examples of how we have applied this method to analyzing the micromagnetic structure of magnetic superlattices and small particles. Although the development of this technique was not supported directly by the ONR grant, we have used the advanced micromagnetic characterization as an important tool in proceeding with our ONR funded research. Additionally, we have applied for an AASERT in order to fund this holography work in parallel with the ONR magnetism in small structures initiative. We therefore include in this annual report applications of the electron holography method important to our ONR funded research.

A Co/Pd multilayer structure ($\text{Pd}(20\text{nm})/[\text{Co}(1\text{nm})\text{Pd}(1.1\text{nm})]_{10}$) with a dominant in-plane magnetization was studied. The Fresnel mode images (Fig. 5.1a and Fig. 5.1b) display a typical distribution of magnetic domain walls appearing as white and dark lines (note in Fig. 5.1a the broad dark biprism shadow and the edge which is parallel to the biprism at the bottom of Fig. 5.1a). Near an edge or hole, the domain walls become nearly parallel to each other, running approximately perpendicularly to the specimen's edge. Further away from the edge, the magnetization begins to curl forming typical 'w' shaped domain

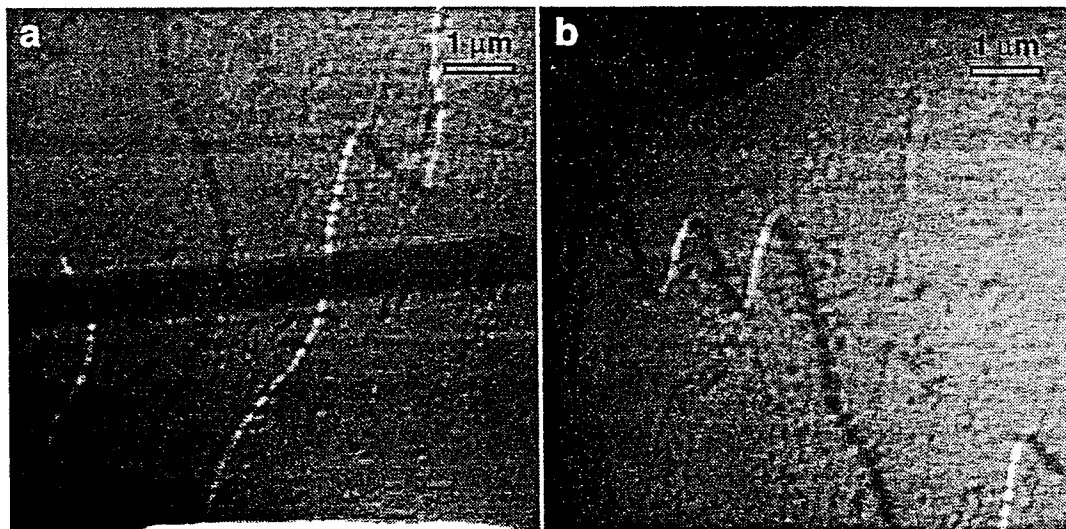


Figure 5.1 (a) and (b) Fresnel mode images of Co/Pd multilayer structures.

walls (Fig. 5.1b). A phase image, reconstructed from a hologram acquired in the absolute mode of STEM holography (Fig. 5.2a) and a three-dimensional map of the marked area (Fig. 5.2b) show that the magnetization is oriented perpendicularly to the edge of the sample and rotates by 180° when crossing the domain wall, a result consistently observed in different specimen regions. A line scan of the phase, taken along the edge and averaged over a region 80 nm across (Fig. 5.2c) shows the linear dependence of the phase inside the domains I and II and the location of the domain wall. The slope of the phase absolutely determines the magnitude of magnetization inside the domains for uniform thickness films. In this case the phase gradient is 28.0 mrad/nm in domain I and 10.9 mrad/nm in domain II. The value in domain I agrees well with the theoretically predicted value for all Co layers ferromagnetically aligned throughout the superlattice stack. Assuming a total Co thickness of $10 \times 1.0 \text{ nm} = 10 \text{ nm}$ with uniform bulk spontaneous magnetization of 1440 emu/cm^3 (1.8096 T) the phase gradient equals 27.49 mrad/nm, i.e. within 2% of the measured value. The magnetization in domain II is $\sim 39.6\%$ of the expected ferromagnetically aligned bulk value. This suggests that not all magnetic layers in domain II are magnetized in the same direction (assuming only in-plane magnetization). The measured value indicates that the magnetization vectors in the layers must be oriented with 7 layers in one direction and three layers in the opposite direction producing a net projected (integrated) magnetization of 40% of the

saturated value. The phase gradient at the wall core (in direction parallel to the wall) is 11.5 mrad/nm. This suggests that not all layers rotate in the wall in the same direction.

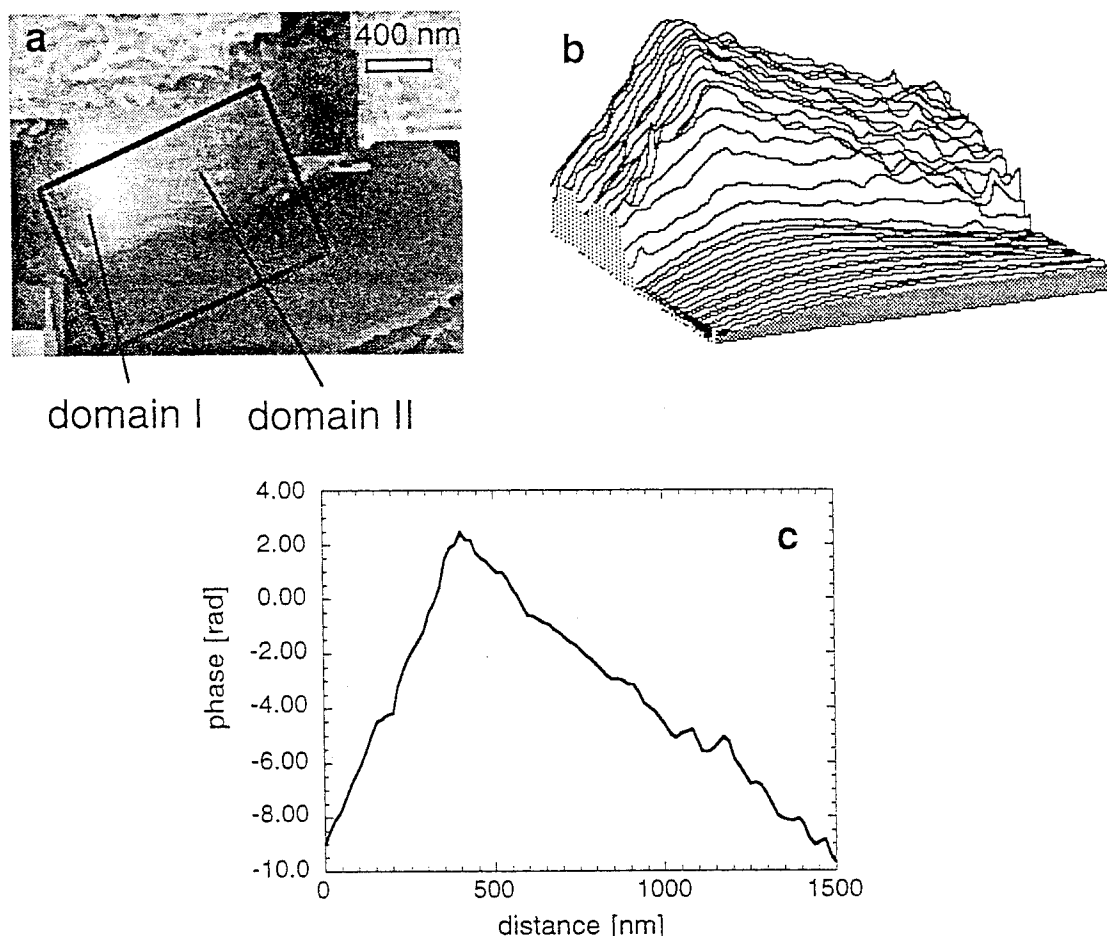


Figure 5.2 Holography of Co/Pd multilayer structures : (a) - partially unwrapped phase image of domain structure near the edge of a film, (b) - three-dimensional plot of the phase in the region marked in (a), (c) - line-scan of phase along specimen edge, averaged across 80 nm.

While observing the magnetic structure near the specimen edge, a strong magnetic flux leak was observed into the surrounding vacuum (Fig. 5.3). The reconstructed, unwrapped phase (Fig. 5.3a) and contour image (Fig. 5.3b) of the same area displays the periodically changing phase; the contours are equimagnetic-induction lines and make the flux-flow more visible. The line-scan in Fig. 5.3c, taken in a direction perpendicular to the film edge, shows the decay of the leakage field. The gradient of the phase, which is proportional to the projected component of the magnetic induction approximately parallel to the edge, reveals that the this field falls to $1/e$ of its maximum value at a distance approximately 250 nm from the edge. The ripple in the right part of the profile is due to the Fresnel fringes of the biprism. A comparison of the line-scan parallel to the film's edge (approximately 150 nm off-edge, Fig. 5.3d) and a Fresnel image of the same area shows that the domain walls terminate at inflexion points of the phase curve and near the center of a domain the phase is a maximum or a minimum. The corresponding maximum phase gradients are 7.1, 5.3 and 9.8 mrad/nm. A three-dimensional plot of the phase in the space near the edge is shown in Fig. 5.3e.

Investigations of the magnetic microstructure in regions far away from a hole are carried out in the differential mode of STEM holography (Fig. 5.4). In this mode, the phase represents a direct measure of the magnetic field in the specimen and displays a constant phase value in regions of constant

magnetization. This is advantageous for the investigation of domain wall profiles. A series of holograms (positions 1 through 3 in Fig. 5.4a) yields a set of 3 domain wall profiles for each of the two marked domain walls A, B. The average domain wall width, as determined from Figs. 5.4b and 5.4c, is 245 nm (wall A) and 200 nm (wall B). The difference in mean domain wall width is related to the presence of partial antiferromagnetic coupling within the superlattice stack.

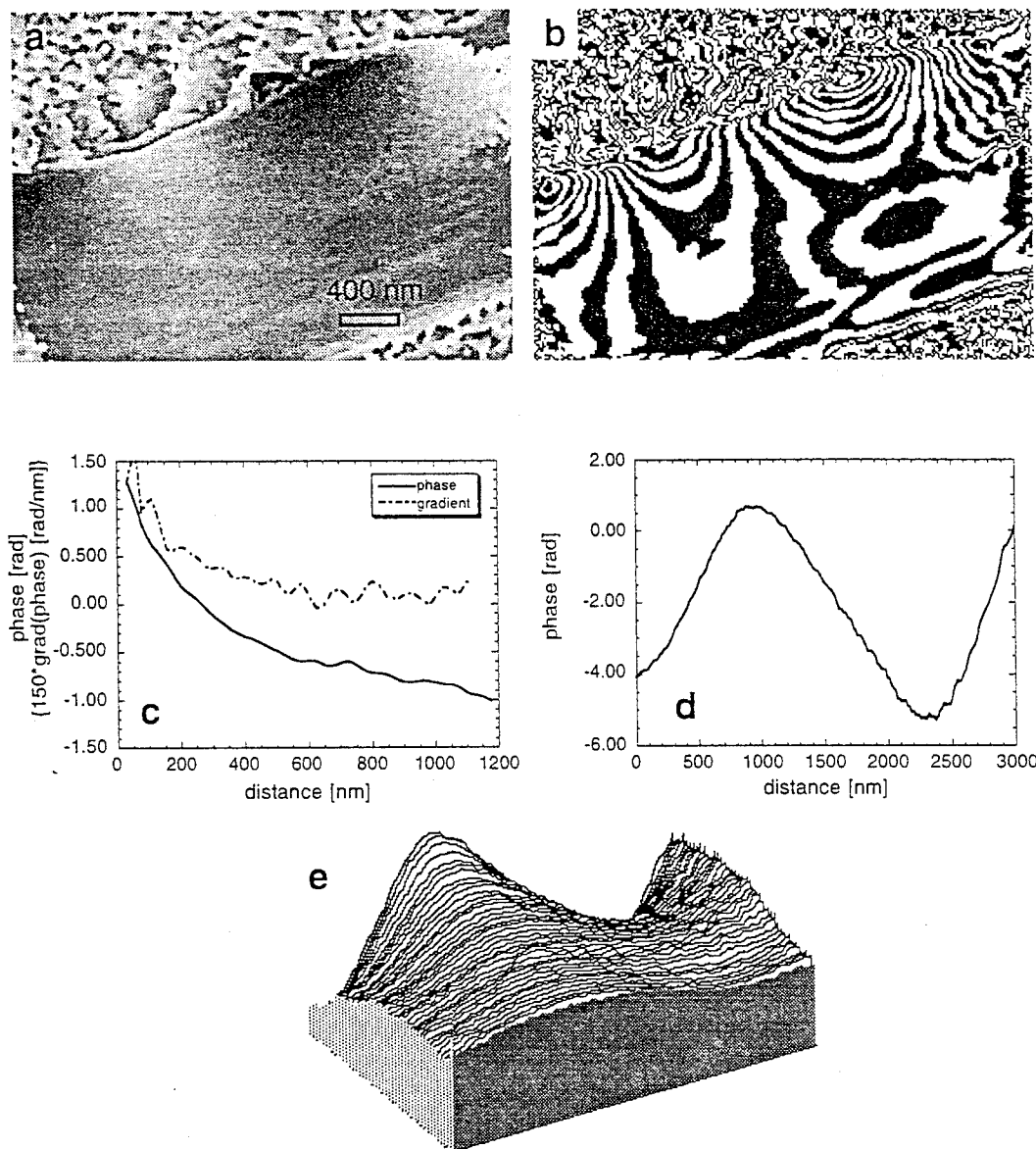


Figure 5.3 Leakage fields in Co/Pd multilayer films : (a) - unwrapped phase image, (b) - contour image of same area as in (a) where one contour corresponds to $\pi/10$ rad, (c) - line-scan of the phase perpendicular to the edge and its gradient, (d) - line-scan of the phase parallel to the edge, (e) - three-dimensional plot of phase outside the specimen.

Magnetic coupling between adjacent ferromagnetic layers in a superlattice composed of alternating ferromagnetic and nonmagnetic layers is present when giant magnetoresistance is observed. A series of multilayer structures with varying seed layer thickness, number of bilayers and bilayer geometry have been grown under ultra-high vacuum conditions. Samples grown on thin amorphous holey carbon films are observed in the Fresnel mode with the beam perpendicular to the layers of the superlattice (not cross-sectional view) and holograms of identical regions yield quantitative information about the magnetic microstructure. The variation of the magnitude of magnetization can be used to determine the interlayer

coupling assuming in-plane magnetization. For example, the Fresnel image of a Co(6nm)/[Cu(3nm)Co(1.5nm)]₆/Cu(3nm) superlattice shows five domains aligned in a flux vortex (Fig. 5.5a). From the hologram (Fig. 5.5b), the maximum phase gradients (in each of the five domains) are 41.2, 41.8, 39.8, 36.7 and 40.7 mrad/nm. The average maximum phase gradient in domains 1, 2, 3 and 5 is 41.0 ± 0.8 mrad, which differs from the predicted bulk value for a cobalt film of 15 nm total thickness (41.4 mrad/nm) by less than 1%. This indicates that the domains penetrate the sandwich and are uniformly (ferromagnetically) aligned. The phase gradient in domain 4 is 36.7 mrad/nm, which is approximately 90% of the expected uniformly magnetized value (37.3 mrad/nm). This magnetization amplitude loss is outlined in Fig. 5.5c. The magnetization in one of the layers (10% of the active thickness) is rotated by 90° with respect to the magnetization in the other layers. The amplitude must then be calculated as a vector sum, i.e. the magnetization amplitude equals to $\sqrt{0.1^2 + 0.9^2} \approx 0.906$ and is therefore approximately 10% lower than the aligned value. If a single layer were antiferromagnetically aligned in the superlattice stack within this domain, the phase gradient would have to be 80% of the maximum value. The existence of 90° coupling between layers has been confirmed by hysteresis loop measurements performed on the same sample (see APL in Appendix C). This confirms that we are able to determine the magnetization orientation of domains in a superlattice and thereby are capable of correlating macroscopic giant magnetoresistance measurements with micromagnetic structure.

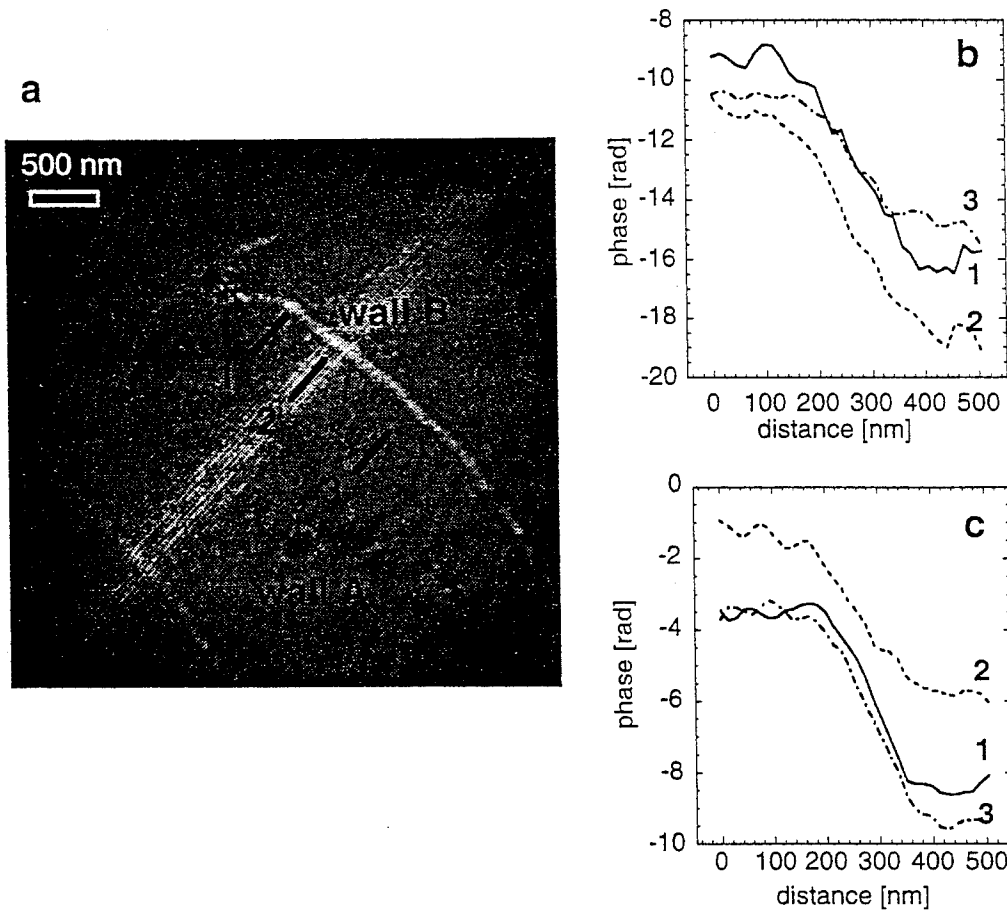


Figure 5.4 Domain walls in Co/Pd multilayer films : (a) - hologram with marked walls and line profile positions, (b) - profiles of broader wall A, (c) - profiles of wall B.

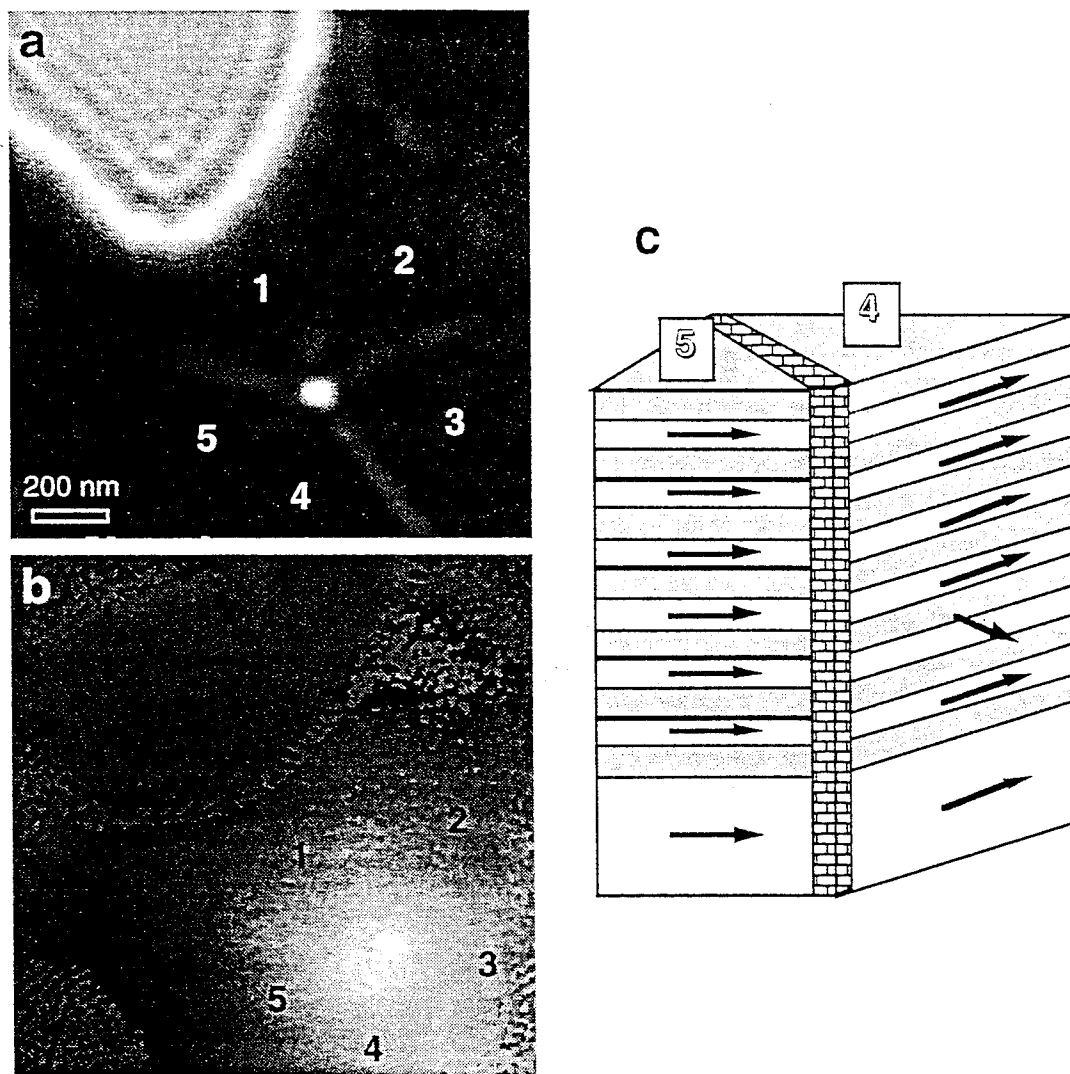


Figure 5.5 Holography of Co/Cu multilayer structures : (a) - Fresnel mode image (underfocus), (b) - unwrapped phase image (absolute mode), (c) - proposed magnetic structure in the multilayer stack.

Small (fine, ultrafine) particles can be defined as structures with dimensions limited in more than one direction, i.e. needles (limited in two dimensions) and genuine small particles (platelets, cubes, etc.). Properties of ultrafine magnetic particles differ considerably from those of the corresponding bulk materials. Magnetic properties are strongly dependent on the surface layers which constitute a relatively large fraction of ultrafines particles. Surface properties are sensitive to the environment and a rigorous investigation requires the application of ultra-high vacuum techniques and in-situ growth and characterization.

Details of the micromagnetic structure, for example the transition between multidomain and single domain behavior, is difficult to determine experimentally due to the small particle size. The critical dimensions, at which this transition occurs, is usually below the resolution limit of conventional magnetic imaging techniques. Most of the published results are based on computational techniques. The particle has a critical length when the micromagnetic stray field energy of the single domain approximately equals the sum of the stray field and domain wall energy of the two-domain state. The transition state depends on the aspect ratio of the particle. Particles of dimensions below approximately 10 nm (depending on material) exhibit superparamagnetic relaxation. When the particle is small enough, the energy barrier due

to anisotropy (proportional to volume) can be overcome by thermal fluctuations, resulting in a flip of the direction of magnetization. Several flips may occur during the measurement, yielding a smaller or zero average value of magnetization and the relaxation time depends strongly on the dimensions. An ensemble of such small particles behaves in a non-zero applied field as an ensemble of paramagnetic atoms (no hysteresis, but saturation when all particles aligned). Magnetic dipolar interactions may be present in these ensembles as well. The interaction depends on the arrangement of particles, varying from a regular lattice-like structure of identical particles to a disordered assembly of non-identical particles. A strong magnetic interaction between ferro- and ferrimagnetic particles may result in ordering of the magnetic moments of particles at temperatures at which they would be superparamagnetic if they were non-interacting.

Qualitative experimental observations of small particles have been carried out using the dry colloid Bitter technique, accompanied by SEM observations, Lorentz microscopy and TEM holography techniques. Direct quantitative investigations of the magnetic microstructure in small magnetic particles have been limited by the relatively low spatial resolution of commonly used micromagnetic analysis techniques (magneto-optical methods, magnetic force microscopy, Bitter-pattern method, etc.). The Fresnel and Differential Phase Contrast (DPC) modes of Lorentz microscopy reveal the in-plane component of magnetization as well as the local microstructure at high spatial resolution, but do not allow accurate quantitative measurements. The deflection angle in the DPC mode is too small ($\sim 10^{-5}$ rad) and in the Fresnel mode, only strong magnetization changes (domain walls, ripple) are observed; an image deconvolution with an exact value of defocus and known wall profile would be required to explicitly extract the micromagnetic structure. Electron holography, carried out in a STEM, provides quantitative information about the magnetization in the specimen at nanometer resolution and therefore represents a valuable tool for the determination of the magnetic microstructure in small particles.

Micromagnetic calculations of the three-dimensional magnetic fields and phase differences must be carried out for comparison with experimental phase images. The intuitive and straightforward interpretation of phase images can be done only for in-plane distributions of the magnetization and flux density. In the following simulations we will consider the absolute mode. Both beams propagate along the z-axis, the reference beam propagates through a field-free region only and its phase is set to zero. The rotation angle ϕ of the beam path in the magnetic field is small,

$$\phi = \frac{e}{2mv} \int_0^t B_z dz ,$$

where the flux is nonzero (not negligible) over a distance t . Consider a 100 nm thick sample with magnetization component $B_z = 10$ kOe. The rotation angle ϕ equals $5.4 \cdot 10^{-5}$ rad and is therefore negligible in phase calculations (and quantitative measurements of the phase).

The magnetic contribution to the phase difference depends upon the orientation, determined by the separation of the two probes. For a point magnetic dipole, located at the origin and oriented along the positive x-axis (Fig. 5.6), the simplified scalar potential is

$$\Phi(x, y, z) = \frac{\mathbf{p} \cdot \mathbf{r}}{r^3} = \frac{x}{\sqrt{(x^2 + y^2 + z^2)^3}}$$

and the components of the flux density can be written as

$$B_x = \frac{3x^2 - (x^2 + y^2 + z^2)}{\sqrt{(x^2 + y^2 + z^2)^5}} ,$$

$$B_y = \frac{3xy}{\sqrt{(x^2 + y^2 + z^2)^5}},$$

$$B_z = \frac{3xz}{\sqrt{(x^2 + y^2 + z^2)^5}}.$$

Figure 5.6 Geometry of the calculated magnetic dipole fields.

When the beam separation is along the x-axis, the phase difference depends on the y-component of the flux density,

$$\Delta\phi(x, y) = -\frac{e}{\hbar} \int_{-\infty}^x \left(\int_{-\infty}^{\infty} B_y dz \right) dx = -\frac{e}{\hbar} \int_{-\infty}^x \frac{4xy}{(x^2 + y^2)^2} dx.$$

The integrand, the projected y-component of the magnetic flux, is shown in Fig. 5.7a and coincides with the image observable in the differential mode. The second integration yields the phase shift as shown in Fig. 5.7c (compare with measured phase shifts).

$$\Delta\phi(x, y) = -\frac{e}{\hbar} \frac{-2y}{x^2 + y^2}$$

When the beam separation is along the x-axis, the phase difference depends on the y-component of the flux density, (Figs. 5.7b and 5.7d)

$$\Delta\phi(x, y) = -\frac{e}{\hbar} \int_{-\infty}^x \left(\int_{-\infty}^{\infty} B_y dz \right) dx.$$

The integrand (B_y) is an odd function of z and the z -integration must be equal zero. Similarly, with the probes separated along the y-direction,

$$\Delta\phi(x,y) = -\frac{e}{\hbar} \int_{-\infty}^y \left(\int_{-\infty}^{\infty} B_x dz \right) dy = 0$$

and no magnetic contrast is observed when the beam is parallel to the dipole axis.

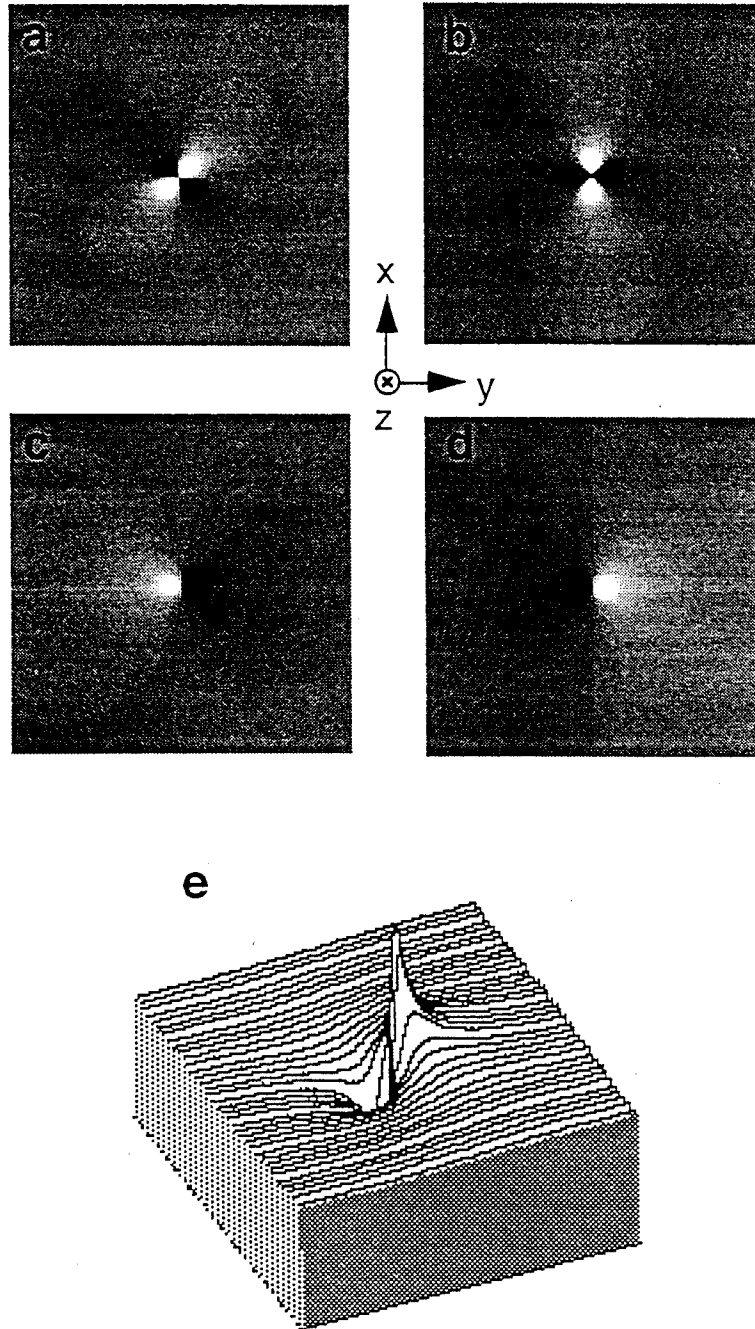


Figure 5.7 Phase image simulations for a magnetic dipole : (a) and (b) - projected y- and x-component of magnetic flux density, (c) and (d) - projected y- (x-) component integrated along x (y), (e) - three-dimensional view of (d).

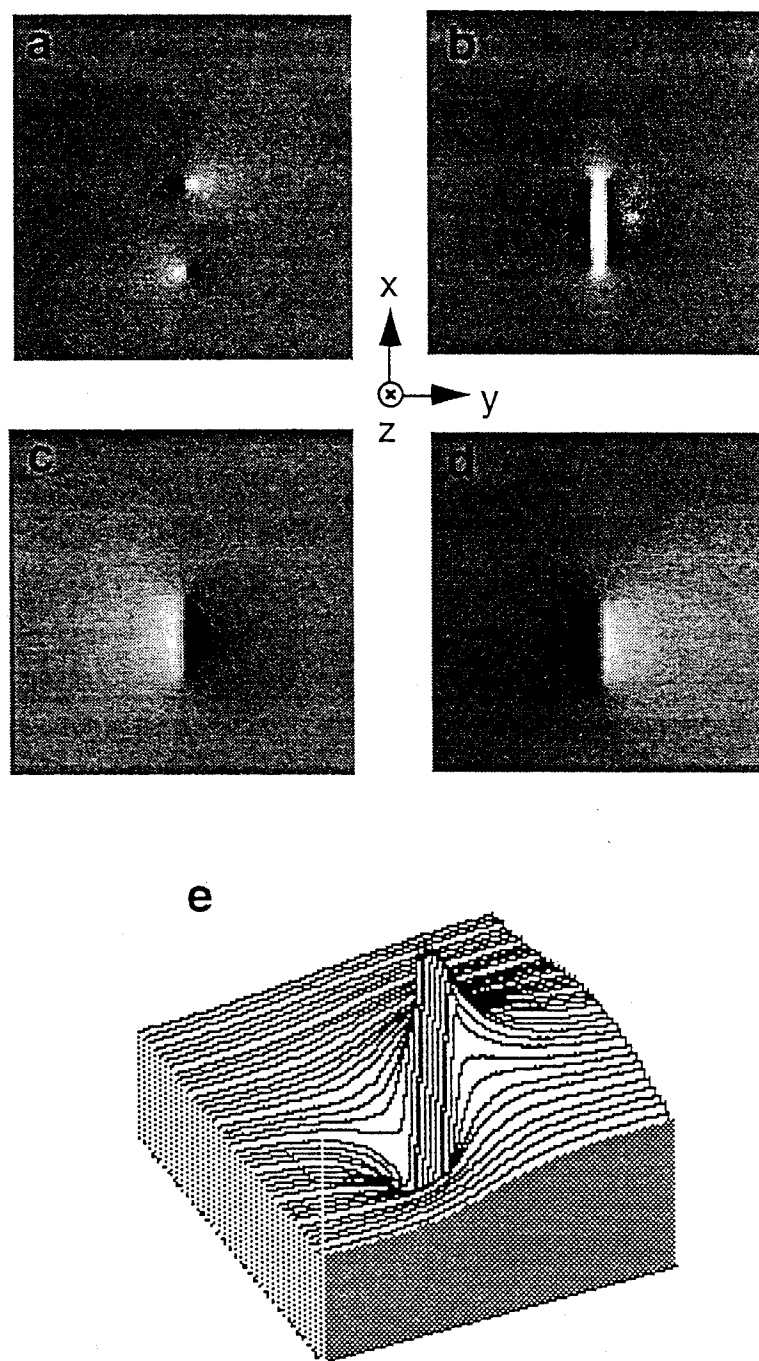


Figure 5.8 Phase image simulations for a physical magnetic dipole : (a) and (b) - projected y- and x-component of the magnetic flux density, (c) and (d) - projected y- (x-) component integrated along x (y), (e) - three-dimensional view of (d).

In the previous calculations we assumed a point dipole and therefore no information can be extracted about the inner structure of the dipole. For simulations accounting for the inner magnetic structure of the dipole (which differs for an electrostatic and magnetic dipole), micromagnetic calculations must be carried out. An example of such a calculation for a $640 \text{ nm} \times 80 \text{ nm} \times 40 \text{ nm}$ rectangular particle with magnetization moment of 400 emu/cm^3 is shown in Fig. 5.8. The integrated y- and x-components of the flux density, coinciding with the differential mode image, are shown in Fig. 5.8a

and 5.8b. The corresponding phase images obtained by integrating B_y along x and B_x along y (Fig. 5.8c and 5.8d) display the characteristic areas of bright and dark contrast outside the particle, the large gradient of the phase inside the particle and the flux leak from the particle's ends. A detailed simulation near one end of a dipole and its possible imaging representations are shown in Fig. 5.9.

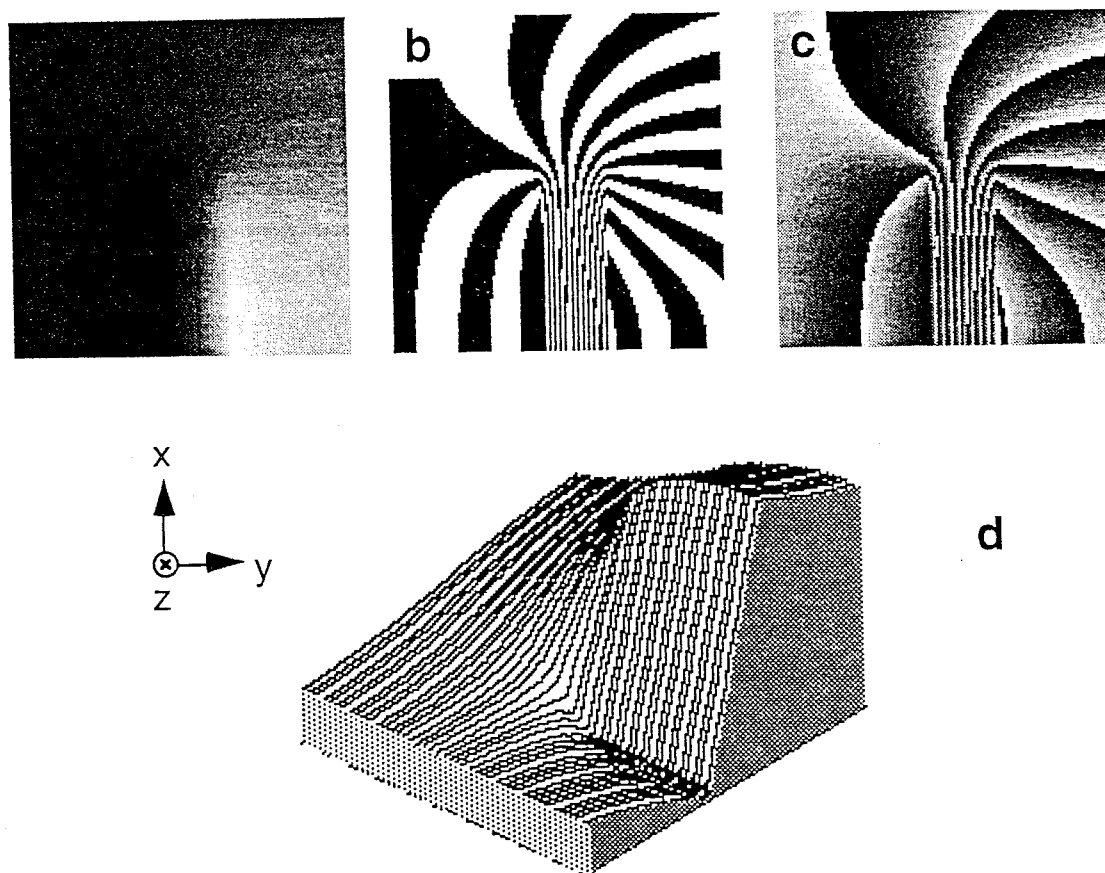


Figure 5.9 Phase image simulations near one end of a physical magnetic dipole : (a) - unwrapped phase image, (b) - contour image, (c) - wrapped phase image, (d) - three-dimensional view of phase image.

CrO_2 particles are elongated 'stretch shaped' particles (approximately 50-100 nm wide and 500-800 nm long) with a magnetic moment of 400 emu/cm^3 and a coercive field of 405 Oe. Holograms of single particles acquired in the absolute mode confirm the prediction that the particles are typically uniformly magnetized. CrO_2 particles are flat needles of nearly constant cross section, therefore we neglect the phase changes due to thickness variations. Micromagnetic calculations of the three-dimensional magnetic fields and phase differences have been carried out for comparison with experimental phase images. A typical example of a CrO_2 particle (640 nm long and 80 nm wide) with magnetic dipole structure is shown in Fig. 5.10a. Typical bright and dark contrast observed outside the particle is in good qualitative agreement with the calculated phase image. Absolute phase shifts caused by the magnetic dipole can be determined. The experimental line-scan across the particle (Fig. 5.10b) shows that the phase gradient inside the particle is approximately 30 mrad/nm, which compares favorably with the calculated image (28.1 mrad/nm). It must be noted here that the phase gradient for an in-plane magnetization distribution (no boundaries) of same thickness corresponds to 30.5 mrad/nm, hence the effects of the demagnetization field is apparent. An accurate value of the thickness is required and is obtained by imaging the particle in bright field using a tilt stage. The volume of the observed particle is approximately $2 \cdot 10^{-3} \mu\text{m}^3$, which corresponds to a magnetic moment of $\sim 10^{-12} \text{ emu}$. This means that we are capable of safely detecting magnetic moments of approximately 4 orders in magnitude smaller than detectable with SQUID

magnetometry. Under (near) ideal imaging conditions we can detect phase gradients of several mrad/nm, corresponding to a minimum particle volume of approximately $1\text{ nm} \times 1\text{ nm} \times 5\text{ nm}$. This corresponds to a magnetic moment of approximately $10^{-16} - 10^{-17}$ emu and presents our current ultimate limit for magnetization measurements.

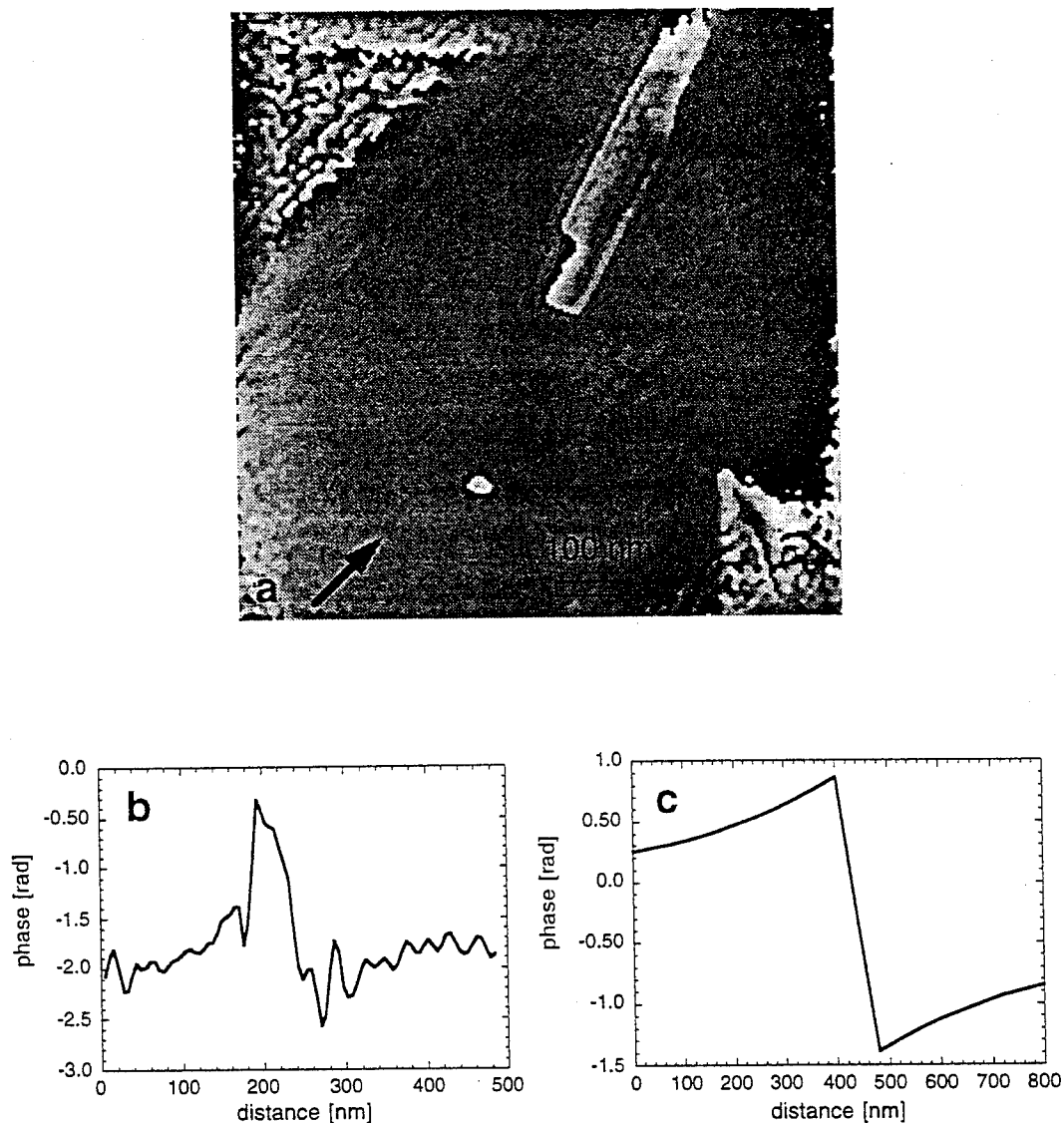


Figure 5.10 Quantitative measurements of a CrO₂ particle : (a) - wrapped absolute phase image, where the arrow marks the measured component of **B**, (b) - line-scan across particle in direction perpendicular to arrow in (a), (c) - line-scan from calculated dipole

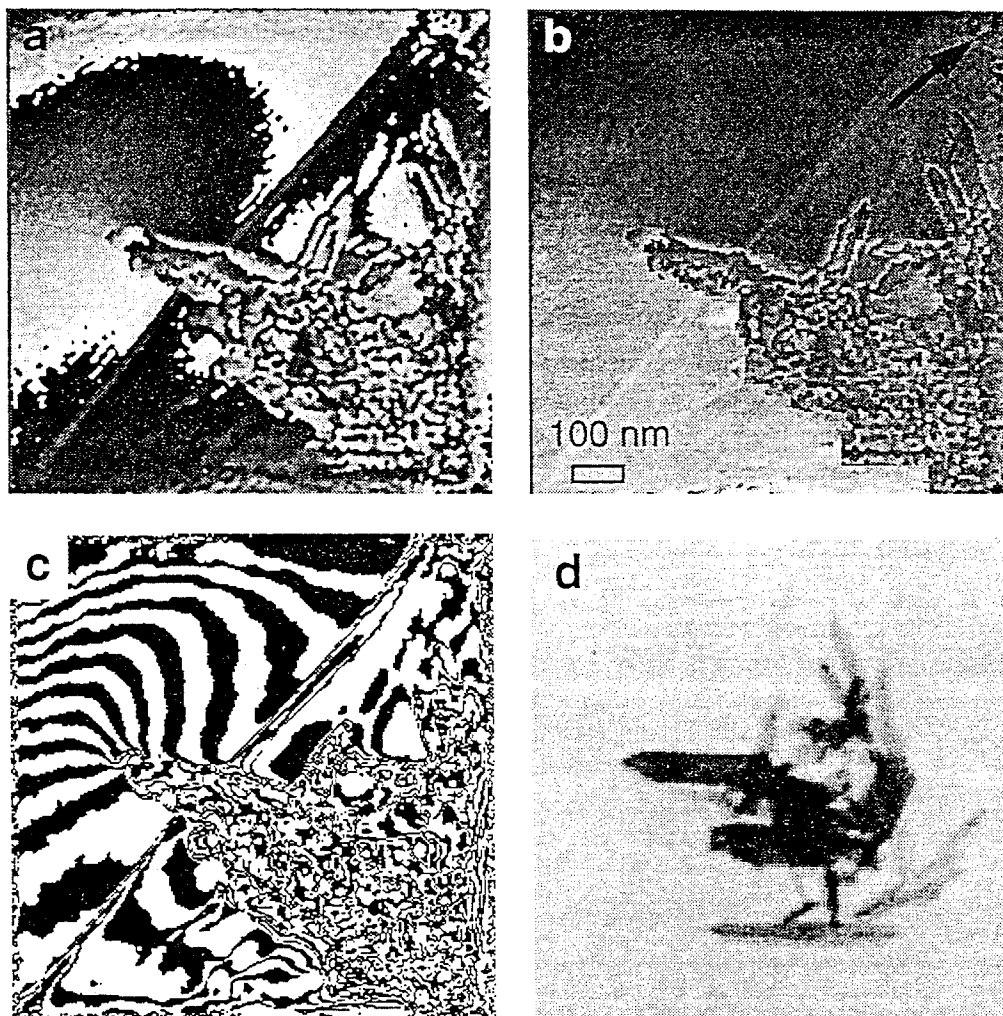


Figure 5.11 A cluster of CrO_2 particles with strong magnetic flux leak : (a) - wrapped absolute phase image, (b) - unwrapped absolute phase image, where the arrow marks the measured component of \mathbf{B} , (c) - contour image of phase, where one contour corresponds to approximately $\pi/11$, (d) - STEM bright field image of the cluster.

A cluster of strongly interacting CrO_2 particles is shown in Fig. 5.11. The magnetizations of the two CrO_2 particles near the edge of the supporting carbon film (Fig. 5.11a - 5.11(c) - phase and contour images) are aligned parallel, which manifests itself as a strong leakage field. A high resolution investigation of the tip of the leaking particle (Fig. 5.12) shows striking resemblance with the simulated images of a dipole end in Fig. 5.9. In comparison, the two CrO_2 particles in Fig. 5.13a and 5.13b (phase and contour image) are aligned antiparallel, therefore the magnetic flux is closed and no flux leak is observed. The three line-scans (Fig. 5.13c) are acquired in the direction of the probe

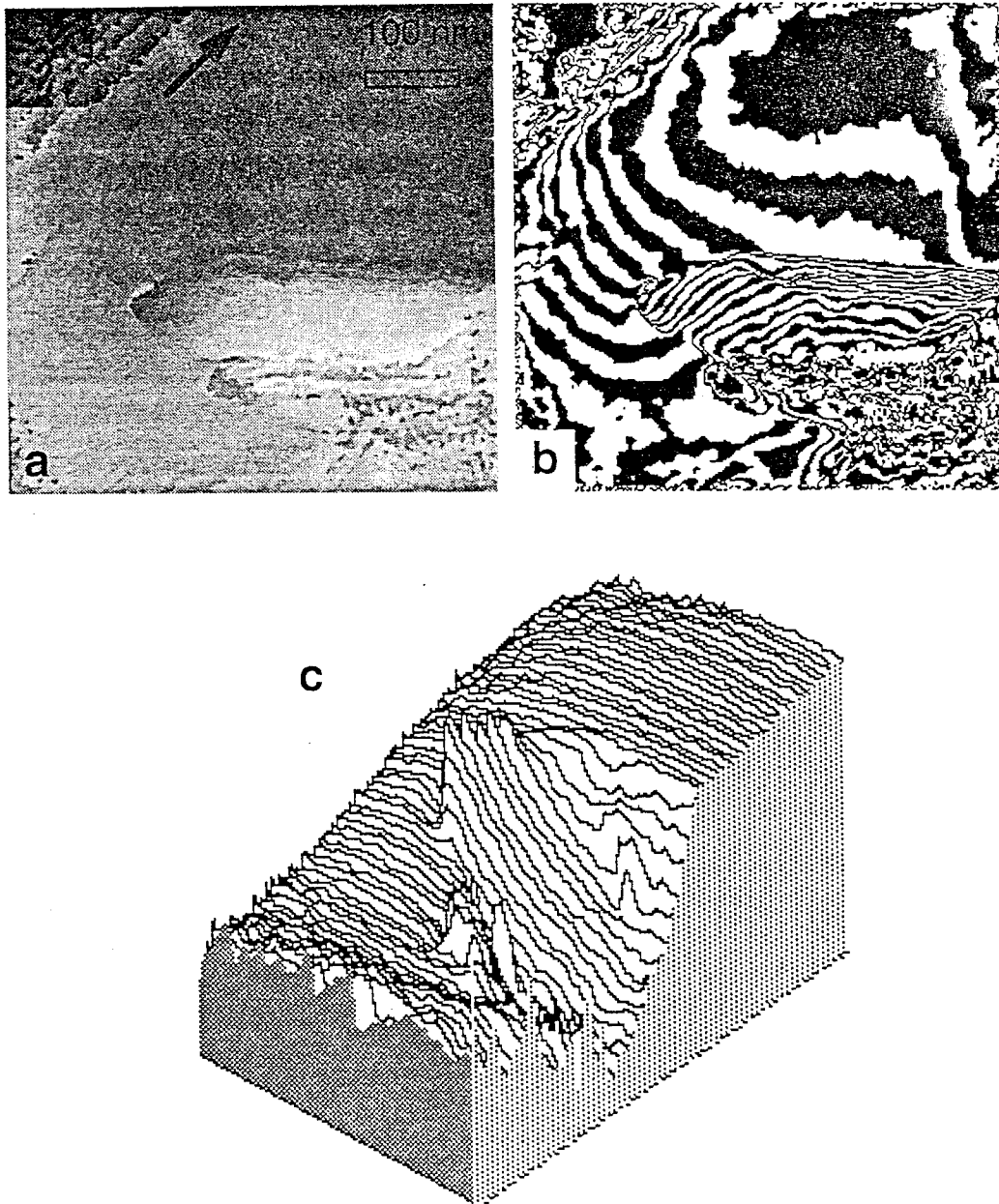


Figure 5.12 Tip of CrO_2 particle with strong magnetic flux leak : (a) - unwrapped absolute phase image, where the arrow marks the measured component of B , (b) - contour image of phase, where one contour corresponds to approximately $\pi/11$, (c) - three-dimensional plot of a part of (a), compare to Fig. V.7.

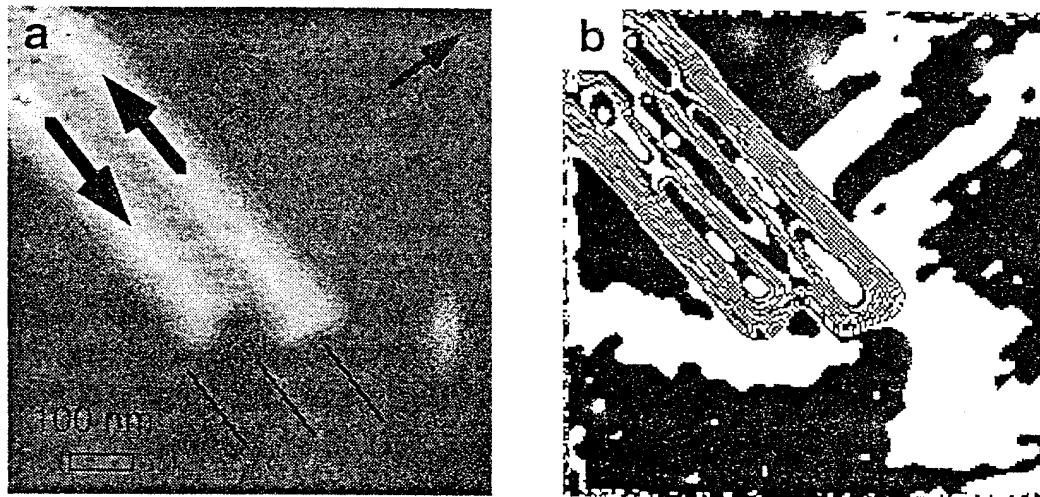


Figure 5.13 Two CrO₂ particles with magnetizations aligned antiparallel : (a) - unwrapped absolute phase image, where the thin arrow marks the measured component of \mathbf{B} , (b) - contour image of phase, where one contour corresponds to approximately $\pi/11$, (c) - three line-scans of phase in direction perpendicular to the (thin) arrow in (a) at positions marked by lines.

separation (perpendicular to arrow in Fig. 5.13a). In the left particle the phase is increasing linearly with an average gradient of 37.8 mrad/nm, while in the right particle the phase is decreasing linearly with an average gradient of -31.1 mrad/nm. In the region of particle overlap the phase is nearly constant (1.1 mrad/nm). Practically no magnetic flux leak is observed outside the particles, supporting the model of the antiparallel orientation of magnetizations in this case.

6.0 Research Plans : Year 3

Year three will continue with the metal/metal interface characterization in both the Co/Cu(100) and Fe/Ag(100) systems. The Fe/CaF₂/Si(111) and Ag/Fe/CaF₂/Si(111) has yielded some very important results. These experiments will be continued with Co as the ferromagnetic transition metal. We will attempt to measure the giant magnetoresistance in these well characterized two dimensional films by searching for an appropriate surface passivation layer for transfer our of UHV. We have been moderately successful at micropatterning 10 nm square Fe regions on the CaF₂ surface. We are exploring alternative methods to fabricate nm diameter ferromagnetic regions microscopically using both scanned probe and scanned electron beam methods in inorganic transition metal halide materials such as CoF₂. Initial results of these studies were very promising and will be continued. We have studied the Co/Cu(100) system which has had the highest reported thin-film magnetoresistances to date. We are systematically exploring the role of in-plane magnetic order, 90° coupling and domain formation with the giant magnetoresistance properties of these films. These studies will be completed this year with a comprehensive study of the domain structure resulting from intralayer coupling such that the role of intralayer and interlayer scattering in GMR structures may be isolated.

7.0 Appendix A: Associated Staff

We currently have 8 people associated with projects supported by this grant. Mike Scheinfein, an Associate Professor in the Department of Physics and Astronomy receives 2 months of summer salary from the grant. Gary Hembree, an Associate Research Scientist in the Department of Physics and Astronomy is on a 12 month University salary and receives no salary from the grant. Jeff Drucker, formerly a Research Scientist in the Center for Solid State Science received 37.5% (\$15,000) of his salary from the grant during the first six months of 1994. Jeff accepted an assistant professor position at the University of Texas at El Paso and left in July. Doug Bradley, Steve Coyle, Kevin Heim, Marian Mankos and Zhijun Yang are/were graduate research associates in the Department of Physics and Astronomy. Kevin Heim and Zhijun Yang were supported 100% time for spring and fall 1994. Both students received their PhD degrees in December. Kevin will take a post-doctoral position at the Jet Propulsion Laboratory in Pasadena. Zhijun is still looking for a post-doctoral position and will remain with the group until June. Marian Mankos was supported on a Department of Energy grant with John Cowley in the spring and on this grant in the fall. Marian has accepted a post-doctoral position in R. Tromp's lab at IBM Yorktown Heights. Steve Coyle has been working with our group for 18 months now. His original support was through a department of education grant (GAANN). He is supported on this grant 100% time in the fall of 1994. He will continue to be supported as he follows up on Kevin Heim's work on small particles and growth in the CaF₂/Si(111) system. Doug Bradley is our newest student and has been working with the group for 6 months. Doug has been growing Fe/Ag on NaCl substrates for low dimensional relaxation studies. He is supported by a GAANN grant until the end of summer 1994. We will likely pick him up on this grant in the fall of 1994. As with all of our students, a trial period of at least one year is used prior to accepting them for support on this grant.

8.0 Appendix B: Publication List

Refereed Scientific Publications (ONR: N00014-93-1-0099)

January 1, 1993 - December 31, 1994

- STEM Holography: Quantitative Characterization of Magnetic Microstructure at Nanometer Spatial Resolution, M. Mankos, M.R. Scheinfein, J.M. Cowley, in *Electron Holography*, Delta Series, eds. A. Tonomura, L. Allanrd, G. Pozzi, D. Joy, Y. Ono, Elsevier Science BV (in press -1994).
- 90° Domains in Co/Cu Giant Magnetoresistance Superlattice, Z.J. Yang, M.R. Scheinfein, Appl. Phys. Lett. (in press-1994).
- Absolute Magnetometry of Thin Cobalt Films and Co/Cu Multilayer Structures at Nanometer Spatial Resolution, Marian. Mankos, Z.J. Yang, M.R. Scheinfein, J.M. Cowley, IEEE-Trans. MAG 30(6), 4497 (1994).
- Far Out-of-Focus Electron Holography in a Dedicated FEG STEM, M. Mankos, A.A. Higgs, M.R. Scheinfein, J.M. Cowley, Ultramicrosc. (in press - 1994).
- Absolute Magnetometry At Nanometer Spatial Resolution : STEM Holography Of Thin Cobalt Films, M. Mankos, M.R. Scheinfein, J.M. Cowley, J. Appl. Phys. 75(11) 7418 (1994).
- Ultra High Vacuum Scanning Electron Microscopy Characterization of the Growth of Fe on $\text{CaF}_2/\text{Si}(111)$: Selective Nucleation on Electron-Beam Modified Surfaces, K.R. Heim, G.G. Hembree, M.R. Scheinfein, J. Appl. Phys. (in press - 1994).
- Structural and Magnetic Properties of Epitaxially Grown fcc Fe/Cu(100) and Fe/ $\text{CaF}_2/\text{Si}(111)$, M.R. Scheinfein, S.D. Healy, K.R. Heim, Z.J. Yang, J.S. Drucker, G.G. Hembree, Proc. Mat. Res. Soc. vol. 323, *Determining Nanoscale Properties of Materials by Microscopy and Spectroscopy*, eds. M. Isaacson, M. Sarikaya, K. Wickramasinghe, 473 (1994).
- Surface Magnetization Processes Investigated by the Combined Surface Magneto-Optical Kerr Effects in fcc Fe/Cu(100) Thin Films, Z.J. Yang, S.D. Healy, K.R. Heim, J.S. Drucker, G.G. Hembree, M.R. Scheinfein, J. Appl. Phys. 75(10), 5589 (1994).
- The Initial Phases of Epitaxy of fcc Fe/Cu(100): Supersurface and Subsurface Island Formation, S.D. Healy, K.R. Heim, Z.J. Yang, J.S. Drucker, G.G. Hembree, M.R. Scheinfein, J. Appl. Phys. 75(10), 5592 (1994).
- Combined Three-Axis Surface Magneto-Optical Kerr Effects in the Study of Surface and Ultrathin Film Magnetism, Z.J. Yang, M.R. Scheinfein, J. Appl. Phys. 74(11) 6810 (1993).
- Correlations Between Ultrathin Film Microstructure and Magnetic Properties in Epitaxial Films of fcc Fe/Cu(100), K.R. Heim, S.D. Healy, Z.J. Yang, J.S. Drucker, G.G. Hembree, M.R. Scheinfein, J. Appl. Phys. 74(12), 7422 (1993).
- Field Induced Metastable States in Ultrathin Films of fcc Fe/Cu(100), G.G. Hembree, J.S. Drucker, S. Healy, K. Heim, Z. Yang, M.R. Scheinfein, Appl. Phys. Lett. 64(8), 1036 (1993).

**Conference Proceedings and Extended Abstracts (ONR: N00014-93-1-0099)
January 1, 1993 - December 31, 1994**

Nanomagnetometry: Electron Holography of Small Particles, M. Mankos, J.M. Cowley, M.R. Scheinfein, IEEE Intermag-95 Digest, Intermag-95, 18-21 April, 1995, San Antonio, TX.

90° Coupling in Co/Cu Giant Magnetoresistance Superlattices, Z.J. Yang, M.R. Scheinfein, IEEE Intermag-95 Digest, Intermag-95, 18-21 April, 1995, San Antonio, TX.

STEM Holography: Quantitative Characterization of Magnetic Microstructure at Nanometer Spatial Resolution, M. Mankos, M.R. Scheinfein, J.M. Cowley, Proc. of the International Workshop on Electron Holography, Oak Ridge National Laboratory, 28-31 August 1994, p. 8.3 (1994).

STEM Holography of Small Metal Particles, M. Mankos, G. Matteucci, M.R. Scheinfein, J.M. Cowley, Proceedings of ICEM-13, Paris, France, 17-22 July 1994, p. 1179.

Quantitative Investigations of Magnetic Microstructure: Electron Holography in a Scanning Transmission Electron Microscope, M. Mankos, Z.J. Yang, M.R. Scheinfein, J.M. Cowley, Proceedings of ICEM-13, Paris, France, 17-22 July 1994, p. 317.

Characterization of Magnetic Microstructure at High Spatial Resolution, M.R. Scheinfein, Proceedings of the 51st Annual Microscopy Society Of America (MSA), G. W. Bailey, Ed., (San Francisco Press, San Francisco, CA 1993) p. 5.

**Arizona State Department of Physics Dissertations (ONR: N00014-93-1-0099)
January 1, 1993 - December 31, 1994**

Kevin R. Heim, "Magnetic and Structural Characterization of Ultrathin Iron Films on Metallic, Semiconducting and Insulating Surfaces," Arizona State University, December 1994.

Marian Mankos, "Electron Holography and Lorentz Microscopy of Magnetic Materials," Arizona State University, December 1994.

Zhijun Yang, "Giant Magnetoresistance and Magnetic Coupling in Co/Cu Superlattices Investigated by the Combined Three-Axis Magneto-Optical Kerr Effect," Arizona State University, December 1994.

9.0 Appendix C: 1994 Publications

STRUCTURAL AND MAGNETIC PROPERTIES OF EPITAXIALLY GROWN FCC Fe/Cu(100) and Fe/CaF₂/Si(111)

M.R. Scheinfein, S.D. Healy, K.R. Heim, Z.J. Yang, J.S. Drucker*, G.G. Hembree.
Department of Physics and Astronomy, *Center for Solid State Science, Arizona State University,
Tempe, AZ 85287-1504

ABSTRACT

We have used nanometer spatial resolution secondary electron and Auger electron imaging in an ultra-high vacuum scanning transmission electron microscope to characterize microstructure in ultrathin films of Fe/Cu(100) grown at room temperature and Fe/CaF₂/Si(111) grown at room temperature and 150 C. Thin film microstructure was correlated in situ with magnetic properties by using the surface magneto-optic Kerr effect.

INTRODUCTION

Ferromagnetic ultrathin epitaxial films grown on single crystal metal substrates display unusual properties characteristic of two-dimensional ferromagnetism stabilized by magnetic (surface) anisotropy [1]. The exchange coupling and crystalline anisotropy depend very sensitively on the lattice. Ultrathin films, grown epitaxially on templates which distort the bulk lattice are often highly strained enabling metastable film properties to be explored at room temperature. The most studied, and perhaps the most complex metal/metal epitaxial system is fcc Fe/Cu(100). The fcc phase of Fe, stable in bulk above 911° C [2], can be grown epitaxially on Cu(100) with 0.83% lattice mismatch. For fcc (fct) Fe, a non-magnetic, high and low spin, or an antiferromagnetic phase can be stable depending upon the lattice constant [3]. The magnetic properties of fcc Fe/Cu(100) have been investigated using the surface magneto-optical Kerr effect (SMOKE) [4,5], spin-polarized photoemission [6], spin-polarized secondary electron spectroscopy [7,8], conversion-Mössbauer spectroscopy [9], inverse photoemission [10] and spin-polarized scanning electron microscopy (SEMPA) [11]. The energy balance between surface anisotropy and shape anisotropy, both strong functions of film thickness, growth and measurement temperature [4,11-13], determine the easy axis of magnetization. Interest in this system is stimulated by rich structural properties present during various phases of film growth [12-18], including bilayer growth during initial phases of epitaxy [15-18], strain-relief at intermediate thicknesses, weak surface reconstructions [12], and fcc to bcc transitions [e.g. 13]. Extensive work has been devoted to correlating film microstructure with magnetic properties [12,13,19] with emphasis on the non-magnetic-to-magnetic transition at 1-2 ML (ML denotes a monolayer, 0.18 nm for fcc Fe(100)) coverages and the polar-to-longitudinal transition in the easy axis of magnetization at 4-8 ML.

EXPERIMENTAL RESULTS

Our magnetic thin film growth and characterization facility is schematically depicted in Fig. 1. The foundation of this system, shown on the far left-hand side of Fig. 1, is a modified Vacuum Generators HB501-S, field-emission scanning transmission electron microscope (STEM) [24,25]. A magnetic parallelizer (P) [26] guarantees nearly 100% collection efficiency at SE energies, and nearly 50% collection efficiencies at intermediate Auger energies (300 eV to 500 eV) [27]. This high collection efficiency and the ability to form subnanometer 100 keV focused electron probes allows for the acquisition of nanometer transverse spatial resolution secondary and Auger electron images [20-23]. A secondary electron detector (SE) located below the sample facilitates in the study of bulk specimens (S). This electron microscope and the attached preparation chamber enables growth and characterization under UHV conditions using high resolution imaging and standard surface science techniques. A 24 hour, 170°C bakeout of the entire microscope and preparation chamber produces base pressures below 5×10^{-11} mbar. The specimen preparation chamber is equipped with a sample heater (H), a Surface Magneto-Optic Kerr Effect (SMOKE)

analysis chamber, a Perkin Elmer model 10-155 cylindrical mirror analyzer (CMA) broad-beam Auger analysis system, a scanning ion sputtering gun (Ar^+), a residual gas analyzer (RGA), various Knudsen cell evaporation sources (K1, K2, and K3), and an electron-bombardment Fe evaporator. The combination of in situ SMOKE measurements with nanometer-resolution microstructural characterization techniques makes this observation system ideal for correlating thin film surface microstructure (those structures with features larger than 1 nm) with macroscopic magnetic properties.

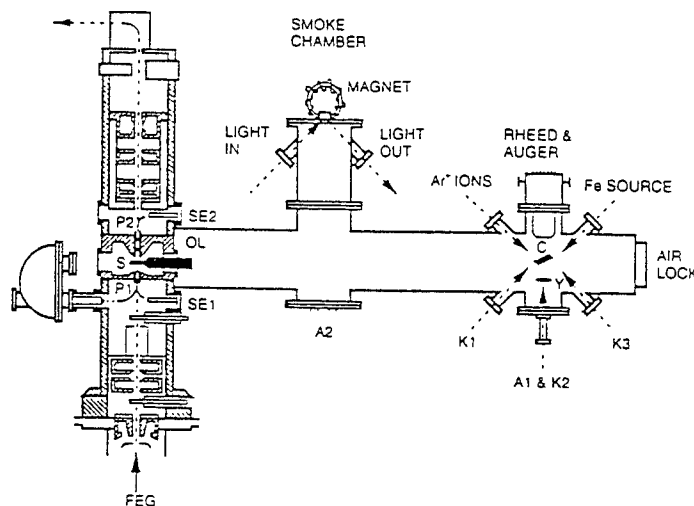


Fig. 1: Modified VG-HB501-S thin film growth and characterization facility. The microscope column contains; P2, P1-upper and lower parallelizers, respectively, SE2, SE1-upper and lower secondary electron detectors, respectively, S-sample, OL-objective lens, and a FEG-field emission gun. The specimen preparation chamber consists of a SMOKE chamber for surface magnetism analysis, a CMA-cylindrical mirror analyzer for AES and RHEED, and sample surface preparation tools such as an Ar^+ ion sputtering gun, an Fe evaporator, annealing stages A1 and A2, and Knudsen cell evaporators K1, K2, and K3. Also shown are the Cu crystal, C, the YAG crystal, Y, and the air lock for fast sample entry.

Single crystal Cu(100) substrates were machined into 1 mm thick, 3 mm diameter shouldered disks and commercially electropolished [28]. After attaining pressures below 5×10^{-11} mbar the Cu specimens were sputtered with 600 eV Ar^+ ions at 45° from the surface normal. Typical ion currents were between 200 and 250 nA (current densities of $\sim 10 \text{ mA/cm}^2$) with an operational pressure of 6×10^{-7} mbar. Specifically, the Cu crystals were first sputtered at room temperature for 1 hour. Next, the Cu was heated to $\sim 330^\circ\text{C}$ and hot-sputtered for 4 hours. Following this, the Cu was annealed at $\sim 600^\circ\text{C}$ for 15 minutes to produce a well-ordered surface, as observed with RHEED. Recleaning samples with less than 10 ML (1 ML = 1.805 \AA) of Fe on them required a $\sim 330^\circ\text{C}$ sputter period of 1 hour. Any cleaned surface exposed to ambient vacuum conditions for more than several hours or exposed to an electron beam (Auger spectroscopy, RHEED, or electron microscopy) was, prior to Fe deposition, cycled through a $\sim 330^\circ\text{C}$, 15 minute sputter and a $\sim 600^\circ\text{C}$, 15 minute anneal. The crystal was allowed to cool for 1.5-2.0 hours after the last anneal such that a temperature below 40°C was obtained prior to Fe deposition.

Following the performed u topography surfaces observed Cu₂O (based islands nuclei coverages \leq to no better : broad-beam 2b are the re spectra clean mode) while about two t oxygen cov clean Cu(10 coverage of 75 nm, which system. The reduced bel electron yie Auger spect larger, more particles po the detector integrity of surfaces ha coverage of

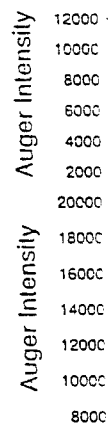


Fig. 2: A dN(E)/dE : step bands scans of ox (f) SE ima,

(CMA) broad-beam
gas analyzer (RGA),
ion-bombardment Fe
anometer-resolution
al for correlating thin
n) with macroscopic

UPCE

AIR
LOCK

ty. The microscope
SE1-upper and lower
FEG-field emission
r surface magnetism
e surface preparation
ges A1 and A2, and
C, the YAG crystal,

diameter shouldered
w 5×10^{-11} mbar the
normal. Typical ion
with an operational
at room temperature
Following this, the
ce, as observed with
e on them required a
vacuum conditions for
RHEED, or electron
minute sputter and a
after the last anneal

Following the surface preparation and Fe deposition, surface structural characterization was performed using secondary electron (SE) microscopy. SE microscopy contrast is sensitive to topography [23,29] and local changes in the work function [30]. Several of the cleaned Cu surfaces observed with SE microscopy revealed small contaminant clusters which we believe to be Cu_2O (based upon the most likely copper oxide formed at these temperatures and pressures [31]) islands nucleated over the entire Cu surface. Analysis of these SE images indicates that oxygen coverages ≤ 0.0011 at.% are well below the sensitivity of the broad-beam AES (typically sensitive to no better than 1 at.%) used in the preparation chamber. In Figs. 2a-f we display corresponding broad-beam Auger spectra and SE images for two identically prepared Cu surfaces. Figs. 2a and 2b are the respective EN(E) and dN(E)/dE spectra acquired for a clean Cu(100) surface. These spectra clearly exhibit five Cu Auger peaks (58, 105, 776, 840, and 920 eV in the derivative mode) while not detecting the O (503 eV) peak (the sensitivity factors at 3 keV indicate that O is about two times more detectable than the 920 eV Cu signal, from which we conclude that the oxygen coverage is ≤ 2 at.%). The SE image shown in Fig. 2e represents a typical area of the clean Cu(100) crystal surface with less than 1.4×10^9 oxide particles/cm², thus yielding an oxygen coverage of 0.016 at.%. The typical terrace width on these Cu(100) surfaces vary from 25 nm to 75 nm, which, based on the uniform growth, is greater than the Fe atom diffusion length for this system. Thus, the effects of a rough and disordered surface on the magnetic properties have been reduced below a detectable level. Insulators and oxides, in general, have higher secondary electron yields than metals [32], and hence appear bright in SE micrographs. In contrast, the Auger spectra in Figs. 2c and 2d also imply a clean Cu surface, but the SE image of Fig. 2f shows larger, more numerous (3.6×10^{10} particles/cm² of 10 nm average radius and 3.75 at.%) oxide particles populating the entire Cu surface. In situ electron microscopy, with its high sensitivity for the detection of surface contamination, was used to guarantee the real space chemical and structural integrity of all Cu(100) substrates prior to Fe deposition. In particular, our cleanest Cu(100) surfaces had 1×10^9 particles/cm² of 3 nm average radius oxide clusters, implying an oxygen coverage of order ≤ 0.01 at.%, well below the detectivity of standard surface science techniques.

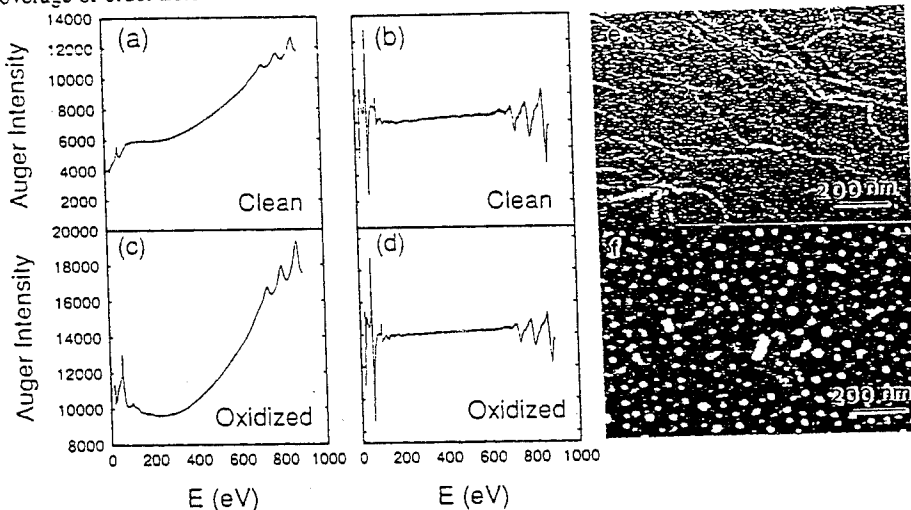


Fig. 2: Auger electron spectroscopy (AES) scans of clean copper in the (a) EN(E) and (b) dN(E)/dE mode with its corresponding (e) secondary electron (SE) image. The white curves are step bands separating terraces. The average terrace width lies within 25 nm and 75 nm. AES scans of oxidized copper in (c) EN(E) and (d) dN(E)/dE mode indicate no contamination while the (f) SE image reveals many oxide.

The thickness dependence of SMOKE hysteresis loops of as-grown fcc Fe/Cu(100) films are shown in Fig. 3. Fe film thicknesses below 2 ML displayed no magnetic response (not shown). Initial magnetic response is observed as a zero-remnance, linear hysteresis loop in the polar direction, with no magnetization in-plane, Figs. 3(a) and 3(b). At intermediate thicknesses, 3.5 ML, remanent polar, Fig. 3(c), and longitudinal, Fig. 3(d), SMOKE loops are observed. While the in-plane loop is square, the tilted polar loop displays the effects of shape anisotropy indicating a canted easy-axis. SMOKE loops from thicker films, 4.7 ML, shown in Figs. 3(e) and 3(f), lose polar remanence, but have square in-plane loops characteristic of an in-plane easy-axis. As-grown in-plane remanence and saturation magnetization both increase nearly linearly with thickness below 5 ML indicating that most of the film (above 2 ML) is magnetically active. Film thicknesses exceeding this range ($t > 10$ ML) become non-magnetic, in accordance with prior observations [13]. Films thinner than 10 ML had fcc structure with the transverse lattice constant of the substrate (our RHEED measurements permit an evaluation of the in-plane lattice constant to within $\pm 2\%$).

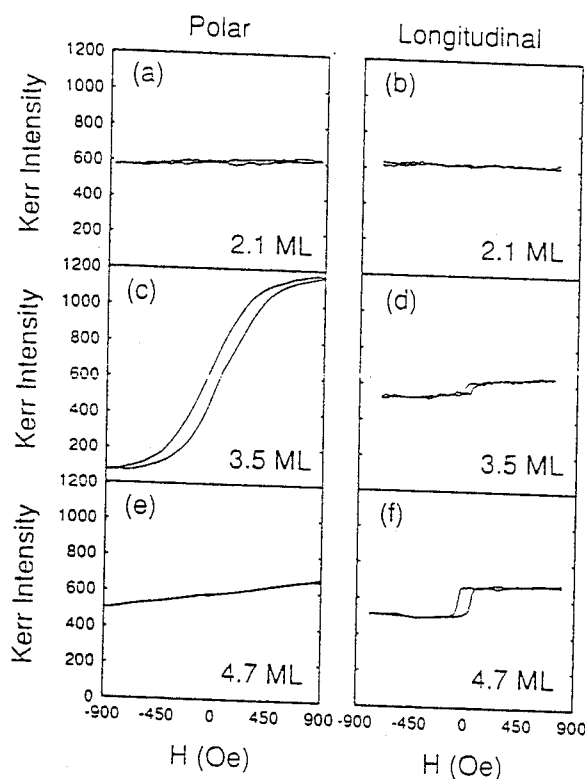


Fig. 3: Room temperature grown fcc Fe/Cu(100) polar and longitudinal surface magneto-optical Kerr effect (SMOKE) hysteresis loops. The incident angle is 45° for both longitudinal and polar SMOKE measurements. (a) polar - 2.1 ML, (b) longitudinal - 2.1 ML, (c) polar - 3.5 ML, (d) longitudinal - 3.5 ML, (e) polar - 4.7 ML and (f) longitudinal - 4.7 ML. All measurements made at room temperature.

At low film coverages, supersurface island formation can be observed locally by correlating the SE images with the Cu and Fe AE images. One such set of spatially correlated images is displayed in Figure 4 for a 0.33 ML thick Fe film. SE images are sensitive to both the work function and topography of the surface. The SE image in figure 4a illustrates supersurface Fe islands with the corresponding contour plot shown in figure 4b. The large island (~ 45 nm in diameter) has intensity contours near its upper left quadrant indicating that this island is composed of more than one monolayer of Fe within the bulk of the island. The contrast of the smaller islands is identical to the contrast of the tip of the larger island (within the signal-to-noise limits of these measurements) indicating identical Fe island thicknesses. AE images and contour maps derived from the Cu (Figs. 4c and 4d) and Fe (Figs. 4e and 4f) Auger electron signals can be directly correlated with the SE

image of
incident e
Auger ele
with the r
for each 2
20 eV hig
subtractin
image is
proportion
and Fe L
signal, wh
contrast
composed
pictured

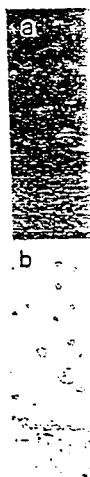


Fig. 4: A
(a) second
Cu LMA
contour
correspo
that the

Figure 5
with 1.7
correlate
Cu and
indicate
the SE y
conclude
contrast
We have
film at
locally

Fe/Cu(100) films are
response (not shown).
resis loop in the polar
mediate thicknesses, 3.5
is are observed. While
the anisotropy indicating
Figs. 3(e) and 3(f), lose
the easy-axis. As-grown
linearly with thickness
ative. Film thicknesses
with prior observations
the lattice constant of the
lattice constant to within

film coverages,
ace island formation
observed locally by
g the SE images with
d Fe AE images. One
of spatially correlated
displayed in Figure 4
ML thick Fe film. SE
e sensitive to both the
ction and topography
face. The SE image in
illustrates supersurface
ands with the
iding contour plot
figure 4b. The large
5 nm in diameter) has
ontours near its upper
unt indicating that this
omposed of more than
layer of Fe within the
e island. The contrast
ller islands is identical
trast of the tip of the
nd (within the signal-
limits of these
nents) indicating
Fe island thicknesses.
s and contour maps
om the Cu (Figs. 4c
d Fe (Figs. 4e and 4f)
ctron signals can be
related with the SE

face magneto-optical
ongitudinal and polar
polar - 3.5 ML, (d)
l measurements made

image of the Fe islands. The AE images are produced by rastering the finely focused 100 keV incident electron beam across the sample surface and collecting most of the Fe (Cu) LMM peak Auger electrons using a spectrometer with a 1.5 eV window which is selected to pass electrons with the respective energy thus generating a two-dimensional surface map. A background map for each Auger map is subsequently acquired by selecting the pass band of the spectrometer to lie 20 eV higher than the Auger peak energy. The images shown in Figs. 4c and 4e result from subtracting the background map from the peak map, such that the intensity within each pixel of the image is proportional to the number of counts within a particular Auger peak, and, therefore, proportional to the number of atoms probed by the incident beam (the sensitivity factors for the Cu and Fe LMM peaks are almost identical). The black areas in Fig. 4c indicate the lack of a Cu signal, while the white areas in Fig. 4e indicate the presence of Fe. It is evident by correlating the contrast in the images and contour maps that the large island and several smaller islands are composed of Fe. Since the signal-to-noise ratio is much better in the SE image, the island density pictured in Fig. 4a likely characterizes the surface.

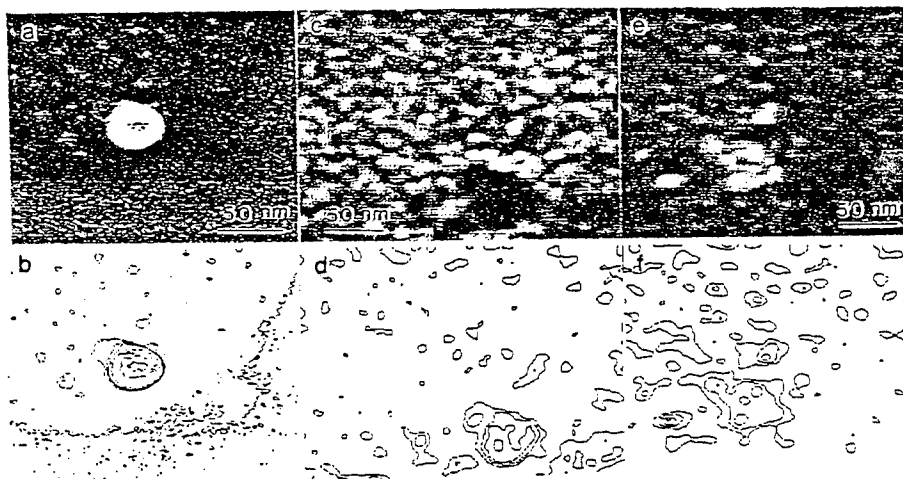


Fig. 4: After deposition of 0.33 ML of Fe at room temperature supersurface islands are observed: (a) secondary electron (SE) image, (b) contour map of SE image indicating island positions, (c) Cu LMM Auger electron (AE) image indicating Cu depletion (black) regions, (d) corresponding contour map of the Cu AE image, (e) Fe LMM AE image indicating Fe (white) islands, and (f) the corresponding contour map of the Fe AE image. The correlation of these three signals indicates that the islands have formed upon the Cu surface. These three images have identical scale factors.

Figure 5a-c displays SE, Cu AE and Fe AE images respectively, all in registry for a Cu substrate with 1.7 ML of Fe deposited at room temperature. The bright regions in the SE image are not correlated with any structure in the Cu (Fig. 5b) or Fe (Fig. 5c) AE images. However, these same Cu and Fe AE images with superimposed contour plots, shown in Figs. 5d and 5e respectively, indicate the regions depleted of Cu are rich in Fe. Since there is no contrast in the SE image, and the SE yield for fcc Fe and Cu are practically identical ($\delta_{Fe} = \delta_{Cu} = 0.38$ at 20 keV [33]), we conclude that there is no topographic structure on the surface in this region, indicating that the contrast observed in the AE images is a result of two-dimensional subsurface island formation. We have also observed both types of island growth as well as layer-by-layer growth in the same film at different positions along the film. This indicates that these phenomena are controlled by locally varying template surface conditions.

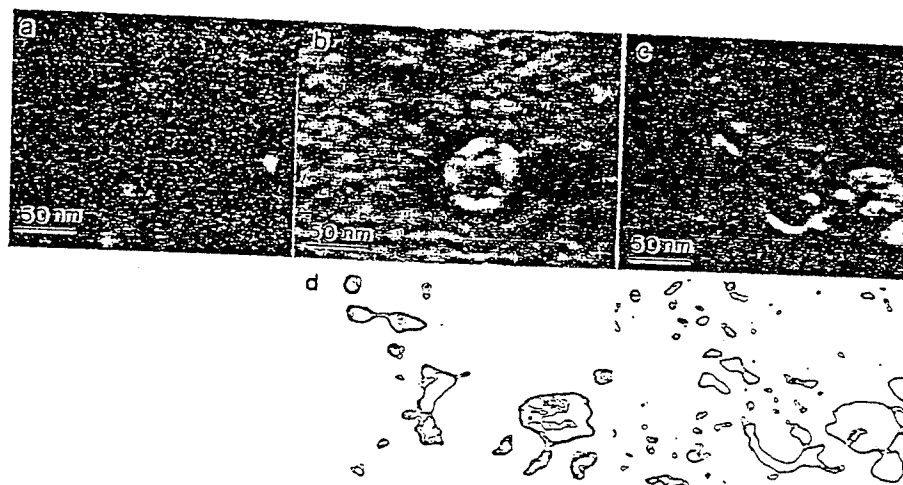


Fig. 5: After deposition of 1.7 ML of Fe at room temperature, subsurface islands are observed. (a) Secondary electron image, (b) Cu LMM Auger electron (AE) image indicating Cu depletion regions (black), and (c) Fe LMM AE image indicating Fe rich regions (white). The correlation of the structure in (b) and (c) and the lack of any contrast in (a) indicates that these islands are within the surface of the substrate. Contour plots for (b) and (c) are shown in (d) and (e) respectively, directly beneath the corresponding image. These three images have identical scale factors.

Our observations suggest that in the regions where subsurface islands occur, a vertical Fe-Cu atomic site exchange occurs. This process continues until the driving force causing the exchange diminishes. We observed this Fe coverage to be thicker than 2 ML, beyond which continuous Fe films grew. The lack of ferromagnetic ordering observed in this sub-2 ML regime is not inconsistent with the observed growth process. In order for the moment of an Fe island to be stable against thermal fluctuations, it must have a minimum size. Assuming a Boltzmann-type probability distribution, it is straight forward to show that most of the Fe islands, which are ~4 nm in diameter, are too small for the moments be unaffected by thermal energy..

We now turn our attention to the growth of Fe on CaF_2 . Presently, the majority of solid state devices are fabricated using Si as the semiconducting material due to the existence of its native oxide, SiO_2 . The lack of an atomically smooth SiO_2 -Si interface does, however, impede the production of three dimensional Si-based devices. Rough interfaces not only decrease the mobility of carriers in devices, but can also destroy the three dimensional epitaxial ordering of subsequent depositions. CaF_2 has been noted as a suitable insulator which may be grown epitaxially and atomically smooth on Si(111) substrates. A small lattice mismatch (0.6% at 298 K) between CaF_2 and Si, a relatively large band gap (12.1 eV) for electronic isolation, and a larger dielectric constant (6.8) than SiO_2 (3.9) for an increased electric field at the insulator-semiconductor device interface are but a few of the many reasons for considering CaF_2 as an obvious replacement for the native SiO_2 . In addition, CaF_2 layers may be used as a buffer region such that devices utilizing highly reactive metals such as Fe are not able to form compounds with the Si substrate. The deposition of Fe would enable the fabrication of fully integrated electronic and magnetic devices on a single substrate. Magnetic sensors, high speed microwave waveguides, and non-volatile memories are just three of the many applications which may result from constructing solid state devices using Fe, CaF_2 , and Si.

For very slow under equilib imbalances.

terms of the s

(γ). When γ

surface. Fe a

550 erg/cm²

formation of

paramagnetic

exhibit giant

critical radiu

isolated ferro

noble metal

addition, sine

may be contr

surface comp

to residual ox

the fabricatio

SE microsc

(radiatively)

obvious sur

spectroscopy

the CaF_2 sur

temperatures

changes have

shown in Fig

many sample

almost triang

from the reli

surface mode

at 300 °C or

small, local

distributions

using an ele

backscatterin

was typically

The initial s

example of

The relative

is clearly di

between the

temperature

grown films

analysis peri

deposition o

average Fe

population v

A 23% cov

7.4×10^{12} is

0.6 nm; (7)

image analy



face islands are observed. The correlation of these islands are within (d) and (e) respectively, critical scale factors.

is occur, a vertical Fe-Cu force causing the exchange beyond which continuous Fe sub-2 ML regime is not present of an Fe island to be summing a Boltzmann-type islands, which are ~4 nm gy.

the majority of solid state the existence of its native does, however, impede the only decrease the mobility al ordering of subsequent be grown epitaxially and % at 298 K) between CaF₂ a larger dielectric constant conductor device interface replacement for the native at devices utilizing highly substrate. The deposition of netic devices on a single on-volatile memories are lid state devices using Fe.

For very slow growth rates the adsorbate topology is expected to approximate structures produced under equilibrium conditions. In this regime, the growth mode is controlled by surface energy imbalances. As Bauer has already set forth [34], a system in equilibrium can be characterized in terms of the surface energy of the adsorbate (γ_a), substrate (γ_s), and the interface between them (γ_i). When $\gamma_a + \gamma_i > \gamma_s$ the deposited material is not expected to spread evenly over the substrate's surface. Fe and CaF₂(111) are known to possess surface energies of 2475 erg/cm² [35] and 450-550 erg/cm² [36], hence, Fe island formation on CaF₂ is expected. We are interested in the formation of monodisperse transition metal island size distributions because ferromagnetic or paramagnetic granules embedded in a three-dimensional noble metal matrix have been shown to exhibit giant magnetoresistive behavior if the granules are properly spaced and smaller than some critical radius [37]. This leads to the natural extension whereby a two-dimensional array of isolated ferromagnetic particles, such as Fe islands on an insulating CaF₂ substrate, covered by a noble metal is expected to yield two-dimensional giant magnetoresistance (GMR) effects. In addition, since CaF₂ can be chemically altered by electron beam exposure [38], growth modes may be controlled for selected regions of the surface prior to metal deposition by modifying the surface composition with an electron beam. A further increase in electron irradiation and exposure to residual oxygen allows the CaF₂ to be used as an electron beam resist [38], thereby expediting the fabrication of nm-size and low dimensional magnetic devices.

SE microscopy (100 keV and ~10 pA incident beam current), performed before and after (radiatively) annealing the CaF₂/Si(111) substrates at 300 °C for 60 minutes, revealed that areas of obvious surface contamination were not reduced by heating. Broad-beam Auger electron spectroscopy (AES) displayed no statistically significant changes in the chemical composition of the CaF₂ surface after annealing for 60 minutes at temperatures up to 400 °C. Higher annealing temperatures do, however, produce significant changes in the surface morphology. These changes have been observed with SE microscopy. An unannealed CaF₂/Si(111) specimen is shown in Fig. 6a. The saw-toothed step edge visible in Fig. 6a is a typical surface feature of the many samples observed. Fig. 6b indicates that, after a 60 minute, 400 °C anneal, numerous, almost triangularly arranged pits are formed. These morphological changes may have resulted from the relief of stresses present during the growth of the CaF₂ [39]. In order to prevent severe surface modifications (pitting) during cleaning, the substrates were either annealed for 60 minutes at 300 °C or for 24 hours at 170 °C prior to the Fe deposition. Obvious contamination occupied small, localized regions of the total CaF₂ surface area (10-30%), such that Fe island size distributions could be determined from regions between the contaminated areas. Fe was deposited using an electron beam evaporator. The evaporation rate was confirmed by Rutherford backscattering, AES, and quartz-crystal microbalance techniques. The pressure during growth was typically less than 2×10^{-9} mbar with the substrates held at either room temperature or 140 °C.

The initial stage of Fe/CaF₂ growth proceeds by three dimensional islanding. Fig. 6c is an example of a 60 minute Fe deposition at a rate of 0.11 Å/min on a room temperature substrate. The relatively even distribution of 2.0 nm diameter Fe islands on a 100 Å thick CaF₂(111) surface is clearly displayed. Particle size analysis of the SE images revealed no statistical difference between the diameters and spatial distribution of Fe islands grown on 140 °C and room temperature CaF₂/Si(111) substrates. A post-growth anneal of 140 °C on room temperature grown films did not produce a noticeable change in the Fe island size distribution. Statistical analysis performed on a large variety of images yielded the following information for a 60 minute deposition of Fe (0.11 Å/min) on room temperature or 140 °C CaF₂/Si(111) substrates: (1) An average Fe island diameter of 2.0 ± 0.3 nm; (2) A range of Fe island diameters where 85% of the population will lie within 2.0 ± 1.0 nm; (3) An average Fe island separation of 2.0 ± 0.4 nm; (4) A 23% coverage of CaF₂(111) with Fe islands; (5) The number of Fe islands per unit area is 7.4×10^{12} islands/cm²; (6) The mean distance between Fe island centers is approximately 3.7 ± 0.6 nm; (7) No geometric ordering of the islands was observed based on fast Fourier transform image analysis.

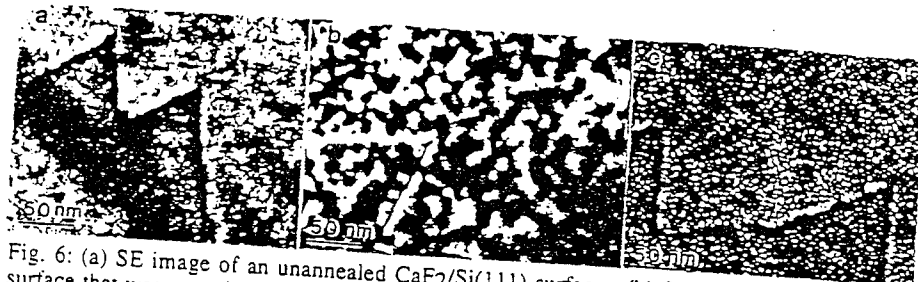


Fig. 6: (a) SE image of an unannealed $\text{CaF}_2/\text{Si}(111)$ surface. (b) SE image of $\text{CaF}_2/\text{Si}(111)$ surface that was annealed for 60 minutes at 400 C. Morphological changes are apparent by the many triangularly oriented pits now covering the entire surface. (c) A 60 minute deposition of Fe at a rate of 0.011 nm/min produces a monodisperse island size distribution.

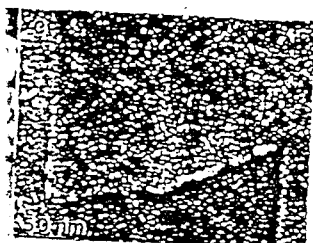
A simple energy calculation indicates that a hemispherically shaped, unstressed, and magnetically ordered Fe particle must contain a single magnetic domain for diameters on the order of a few tens of nanometers. This transition is a result of domain formation becoming energetically unfavorable as the magnetic particle becomes smaller due to the domain boundary energy becoming a large percentage of the total energy. The islands observed in Fig. 6c are smaller than the critical single domain size and separated by less than the mean free path of conduction electrons in metals (near 30 nm at room temperature for Cu [40]). These properties make this system of nm-size Fe islands on an insulator, when covered by a noble metal, an excellent candidate for room temperature GMR studies [41].

CONCLUSIONS

In situ, magnetic and structural characterization of ultrathin films of Fe on Cu(100) was performed using SMOKE, RHEED, broad-beam AES, SE imaging, and AE imaging. Results indicate that room temperature grown films are non-magnetic below 2.1 ML, are ferromagnetic between 2.3 and 5 ML, and are no longer ferromagnetic greater than 5 ML but less than 10 ML. SE and AE images reveal localized alloying and simultaneous multilayered growth for films less than 2 ML and no gross structural changes for films of order 10 ML. AES reconfirms a simultaneous multilayered growth mode due to the lack of breaks in the normalized MVV Cu peak-to-peak height curve as a function of evaporation time. Broad-beam AES was determined to be inadequate for determining the oxide contamination of Cu crystal surfaces because of a lack of detection sensitivity, and may account for the variability in some growth/magnetic properties studies in the fcc Fe/Cu(100) system. Both supersurface islanding and subsurface islanding through vertical atomic site exchange in room temperature grown films of fcc Fe/Cu(100) in the 0-2 ML regime was observed. These observations are not inconsistent with the lack of ferromagnetism observed in room temperature grown sub-2 ML fcc Fe/Cu(100) ultrathin films. A narrow size distribution of 2.0 nm diameter Fe islands was grown on $\text{CaF}_2/\text{Si}(111)$ surfaces held at or near room temperature. This system, an arrangement of possibly single domain particles separated by less than the mean free path of conduction electrons in metals, is an exciting new candidate for GMR studies.

ACKNOWLEDGEMENTS

The authors wish to acknowledge thoughtful discussions with S. Bader, P. Bennett, M. Hart, D. Loretto, W. Petuskey and J. Venables. We are also indebted to D. Loretto of Lawrence Berkeley Laboratory for supplying the $\text{CaF}_2/\text{Si}(111)$ samples. This work is supported by the Office of Naval Research under grant No. N00014-93-1-0099 and the National Science Foundation under grant No. DMR 89-14761. The microscopy was performed at the National Science Foundation supported Center for High Resolution Electron Microscopy at Arizona State University, grant No. DMR-91-15680.



(b) SE image of $\text{CaF}_2/\text{Si}(111)$
cal changes are apparent by the
c) A 60 minute deposition of Fe
tribution.

ed, unstressed, and magnetically
neters on the order of a few tens
oming energetically unfavorable
ndary energy becoming a large
e smaller than the critical single
uction electrons in metals (near
is system of nm-size Fe islands
ate for room temperature GMR

Fe on Cu(100) was performed
maging. Results indicate that
re ferromagnetic between 2.3
less than 10 ML. SE and AE
rowth for films less than 2 ML
S reconfirms a simultaneous
lized MVV Cu peak-to-peak
s determined to be inadequate
ecause of a lack of detection
netic properties studies in the
etic islanding through vertical
ce islanding through vertical
u(100) in the 0-2 ML regime
of ferromagnetism observed
s. A narrow size distribution
aces held at or near room
in particles separated by less
ing new candidate for GMR

ter, P. Bennett, M. Hart, D.
retto of Lawrence Berkeley
supported by the Office of
Science Foundation under
ational Science Foundation
State University, grant No.

REFERENCES

1. N.D. Mermin, H. Wagner, Phys. Rev. Lett. **17**, 1133 (1966).
2. L.J. Schwartzendrubber, Binary Phase Diagrams : vol. 2, (Publisher, 1990).
3. O.N. Mryasov, A.I. Liechtenstein, L.M. Sandratskii, V.A. Gubanov, J. Phys.: Condens. Matter **3**, 7683 (1991); G.L. Krasko, G.B. Olson, Phys. Rev. **B40**, 11536 (1989); T. Kraft, M. Methfessel, M. van Schilfgaarde, M. Scheffler, Phys. Rev. **B47**, 9862 (1993); V.L. Moruzzi, P.M. Marcus, K. Schwarz, P. Mohn, Phys. **B34**, 1784 (1986).
4. C. Liu, E.R. Moog, S.D. Bader, Phys. Rev. Lett. **60**, 2422 (1988); C. Liu, E.R. Moog, S.D. Bader, J. Appl. Phys. **64**, 5325 (1988); C. Liu, S.D. Bader, J. Vac.Sci. Technol. **A8**, 2727 (1990); S.D. Bader, Proc. IEEE **78**, 909 (1990).
5. W.R. Bennett, W. Schwarzacher, W.F. Egelhoff Jr., Phys. Rev. Lett. **65**, 3169 (1990).
6. D. Pescia, M. Stamparoni, G.L. Bona, A. Vaterlaus, R.F. Willis, F. Meier, Phys. Rev. Lett. **58**, 2126 (1987).
7. D.P. Pappas, K.-P. Kamper, H. Hopster, Phys. Rev. Lett. **64**, 3179 (1990).
8. D.P. Pappas, K.-P. Kamper, B.P. Miller, H. Hopster, D.E. Fowler, A.C. Luntz, C.R. Brundle, Z.-X. Shen, J. Appl. Phys. **69**, 5209 (1991).
9. W.A.A. Macedo, W. Keune, Phys. Rev. Lett. **61**, 475 (1988).
10. F.J. Himpsel, Phys. Rev. Lett. **67**, 2363 (1991).
11. R. Allenspach, A. Bishof, Phys. Rev. Lett. **69**, 3385 (1992).
12. P. Xhonneux, E. Courtens, Phys. Rev. **B46**, 5561 (1992).
13. J. Thomassen, F. May, B. Feldmann, M. Wuttig, H. Ibach, Phys. Rev. Lett. **69**, 3831 (1992).
14. W.A. Jesser, J.W. Mathews, Phil. Mag. **15**, 1097 (1967); Phil. Mag. **17**, 461 (1968).
15. S.A. Chambers, T.J. Wagener, J.H. Weaver, Phys. Rev. **B36**, 8982 (1987).
16. D.A. Steigerwald, W.F. Egelhoff Jr, Surf. Sci. **192**, L887 (1987); D.A. Steigerwald, F. Jacob, W.F. Egelhoff Jr., Surf. Sci. **202**, 472 (1988).
17. H. Glatzel, Th. Farster, B.M.U. Scherzer, V. Dose, Surf. Sci. **254**, 58 (1991).
18. A. Brodde, H. Neddermeyer, Ultramicro. **42-44**, 556 (1991).
19. H. Magnan, D. Chandesris, B. Villette, D. Heckmann, J. Lecante, Phys. Rev. Lett. **67**, 859 (1991).
20. G. Hembree, J. Drucker, L. Hong, M. Krishnamurthy, and J. A. Venables, Appl. Phys. Lett. **58**, 1991.
21. G. G. Hembree and J. A. Venables, Ultramicroscopy **47**, 109 (1992); J. Liu, G. G. Hembree, G. E. Spinnler, and J. A. Venables, Surface Science Lett. **262**, L111 (1992); J. Liu, G. G. Hembree, G. E. Spinnler, and J. A. Venables, Catalysis Letters **15**, 133 (1992).
22. M. Krishnamurthy, J. Drucker, and J. Venables, J. Appl. Phys. **69**, 6461 (1991).
23. J. Drucker, M. Krishnamurthy, and G. Hembree, Ultramicroscopy **35**, 323 (1991).
24. G. G. Hembree, P. A. Crozier, J. S. Drucker, M. Krishnamurthy, J. A. Venables, and J. M. Cowley, Ultramicroscopy **31**, 111 (1989).
25. J. A. Venables, J. M. Cowley, and H. S. von Harrach, Inst. Phys. Conf. Ser. **90**, 85 (1987).
26. P. Kruit and J. A. Venables, Ultramicroscopy **25**, 183 (1988).
27. P. Kruit, Adv. Opt. Electron Microsc. **12**, 93 (1991).
28. M. R. Scheinfein, unpublished.
29. Crystals were custom fabricated by Virgil Straughn, Monocrystals Inc. Cleveland, OH.
30. J. Drucker, J. Appl. Phys. **70**, 2806 (1991).
31. J. A. Venables, D. R. Batchelor, M. Hanbücken, C. J. Harland, and G. W. Jones, Phil. Trans. R. Soc. Lond. A **318**, 243 (1986).
32. F. Grønlund and P. E. H. Nielsen, Surface Science **30**, 388 (1972).
33. G. W. Goetze, A. H. Boerio, and M. Green, J. Appl. Phys. **35**, 482 (1964); G. W. Goetze, Adv. Electron. Electron Phys. **22**, 219 (1968).
34. L. Reimer, Scanning Electron Microscopy, (Springer-Verlag, Berlin, 1985).
35. E. Bauer, Z. Krist. **110**, 372 (1958).
36. F. R. de Boer, R. Boom, W. C. M. Mattens, A. R. Miedema, and A. K. Niessen, Cohesion in Metals Transition Metal Alloys (North-Holland Elsevier Science Publishers, NY, 1988).

36. J. J. Gilman, J. Appl. Phys. 31, 2208 (1960). G. C. Benson and T. A. Claxton, Can. J. Phys. 41, 1287 (1963). P. W. Tasker, J. Phys. (Paris) 41, C6-488 (1980).
37. J. Q. Xiao, J. S. Jiang, and C. L. Chien, Phys. Rev. Lett. 68, 3749 (1992).
38. T. R. Harrison, P. M. Mankiewich, and A. H. Dayem, Appl. Phys. Lett. 41, 1102 (1982). P. M. Mankiewich, H. G. Craighead, T. R. Harrison, and A. H. Dayem, Appl. Phys. Lett. 44, 468 (1984). M. Scheinfein and M. Isaacson, J. Vac. Sci. Technol. B 4, 326 (1986).
39. Private communication with D. Loretto: Bright field transmission electron microscopy performed on the $\text{CaF}_2/\text{Si}(111)$ samples revealed a non uniform distribution of line defects at the $\text{CaF}_2\text{-Si}(111)$ interface. This is an indication that stress relief occurred during the CaF_2 growth. In comparison, an unrelaxed film will display a parallel array of line defects corresponding to the original steps on the $\text{Si}(111)$ surface.
40. C. Kittel, *Introduction to Solid State Physics, fourth edition* (John Wiley & Sons, 1971), page 259.
41. C. L. Chien, J. Appl. Phys. 69, 5267 (1991). A. E. Berkowitz, J. R. Mitchell, M. J. Carey, A. P. Young, S. Zhang, F. E. Spada, F. T. Parker, A. Hutten, and G. Thomas, Phys. Rev. Lett. 68, 3745 (1992). A. E. Berkowitz, J. R. Mitchell, M. J. Carey, A. P. Young, D. Rao, A. Starr, S. Zhang, F. E. Spada, F. T. Parker, A. Hutten, and G. Thomas, J. Appl. Phys. 73, 5320 (1993).

Ultrahigh-vacuum scanning electron microscopy characterization of the growth of Fe on $\text{CaF}_2/\text{Si}(111)$: Selective nucleation on electron-beam modified surfaces

K. R. Heim, G. G. Hembree, and M. R. Scheinlein
Box 871504, Department of Physics and Astronomy, Arizona State University, Tempe, Arizona 85287-1504

(Received 11 November 1993; accepted for publication 31 August 1994)

The initial stages of Fe island growth on electron-beam modified and unmodified $\text{CaF}_2/\text{Si}(111)$ surfaces were studied with a nanometer lateral spatial resolution ultrahigh-vacuum scanning electron microscope. Fe coverages between 7 and 8 ML (deposition rates from 0.12 to 0.19 ML/min, 1 ML = 7.7×10^{14} atom/cm²) grown on room temperature through 300 °C $\text{CaF}_2/\text{Si}(111)$ relaxed and unrelaxed substrates produced a relatively uniform distribution of islands that cover 23% of the substrate with an island density of 7.4×10^{12} island/cm². Chemical or defect dominated Fe growth on the $\text{CaF}_2/\text{Si}(111)$ substrates is indicated by the temperature independence of the Fe island distributions for 20 °C < T < 300 °C. Substrate temperatures near 400 °C yielded mottled surfaces and an altered island distribution relative to those formed during growth at temperatures between 20 and 300 °C. Parallel step edges separated by 25–75 nm were observed for unrelaxed films of CaF_2 on Si(111), while relaxed CaF_2 films exhibited a saw-toothed step pattern. Fe coverages of $\Theta = 21.4$ ML produced a percolation network of connected islands rather than a continuous film covering the CaF_2 substrate. The production of nanometer-sized surface structures was evaluated for electron-beam modified growth of Fe on $\text{CaF}_2/\text{Si}(111)$ substrates. Pregrowth (100 keV, 8.2–140 pA) electron irradiation doses as low as 1.14 C/cm² altered the Fe film morphology on the selectively irradiated regions. Areas dosed with electron irradiation prior to Fe growth were more stable to the damaging effects of post-growth electron irradiation as compared to regions that had not been exposed.

I. INTRODUCTION

Recent progress in the experimental study of the growth and characterization of metals on insulators has been motivated by expectations that these materials will improve upon our current solid-state device technology. Components such as quantum-interference high-speed electron devices,¹ triple-barrier resonant tunneling diodes,² hot electron transistors,³ and metal-epitaxial insulator-semiconductor field-effect transistors⁴ have been fabricated or proposed using metals, insulators, and semiconductors. Presently, the majority of solid state devices are fabricated using Si as the semiconducting material due to the existence of its native oxide, SiO_2 . The lack of an atomically smooth SiO_2 -Si interface does, however, impede the production of three-dimensional Si-based devices. Rough interfaces not only decrease the mobility of carriers in devices, but can also destroy the three-dimensional epitaxial ordering of subsequent depositions. CaF_2 has been considered as a suitable replacement for SiO_2 since it can be grown epitaxially and atomically smooth on Si(111) substrates.⁵ A small lattice mismatch (0.6% at 298 K) between CaF_2 and Si, a relatively large band gap (12.1 eV) for electronic isolation, and a larger dielectric constant (6.8) than SiO_2 (3.9) for an increased electric field at the insulator-semiconductor device interface are but a few of the many reasons for considering CaF_2 as an obvious replacement for the native SiO_2 .⁵ In addition, CaF_2 layers may be used as a buffer region such that devices utilizing highly reactive metals such as Fe are not able to form compounds with the Si substrate. The patterned deposition of Fe on $\text{CaF}_2/\text{Si}(111)$ would enable the fabrication of fully integrated electronic

and magnetic devices on a single substrate. Magnetic sensors, high-speed microwave wave guides, and nonvolatile memories (e.g., Ref. 6) are just three of the many applications which may result from constructing solid-state devices using Fe, CaF_2 , and Si.

Adsorbate topology should be characterized by an approximately equilibrium configuration for very slow growth rates. In this regime, the growth mode is controlled by surface energy imbalances. Bauer has characterized⁷ a system in equilibrium in terms of the surface energy of the adsorbate (γ_a), substrate (γ_s), and the interface between them (γ_i). When $\gamma_a + \gamma_i > \gamma_s$, the deposited material is not expected to spread evenly over the substrate's surface. Fe and $\text{CaF}_2(111)$ are known to possess surface energies of 2475 erg/cm² (Ref. 8) and 450–550 erg/cm² (Ref. 9), hence, Fe island formation on CaF_2 is expected. Since CaF_2 can be chemically altered by electron beam exposure,¹⁰ growth modes may be controlled for selected regions of the surface prior to metal deposition by modifying the surface composition with an electron beam. A further increase in electron irradiation and exposure to residual oxygen allows the CaF_2 to be used as an electron beam resist,¹⁰ thereby expediting the fabrication of nanometer-sized and low-dimensional magnetic devices.

II. SUBSTRATE CHARACTERIZATION

In this paper, nanometer lateral spatial resolution structural measurements obtained during the initial stages of growth for the Fe/ $\text{CaF}_2/\text{Si}(111)$ system are reported. The growth and preparation conditions for the CaF_2 on Si(111) substrates have been described in detail elsewhere.¹¹

FIG. 1. Secondary electron images of a relaxed $\text{CaF}_2/\text{Si}(111)$ specimen (a) before annealing and (b) after annealing for 1 h at 400 °C. Morphological changes are apparent: by the many triangularly oriented pits now covering the entire CaF_2 surface. The CaF_2 film is approximately 10 nm thick. Saw-toothed step edges are a common surface feature for relaxed CaF_2 films.

Samples of 10-nm-thick [33 triple layers (TL), 1 TL=0.315 nm¹²] relaxed and unrelaxed $\text{CaF}_2/\text{Si}(111)$ ¹³ were cut into 3 mm disks with an ultrasonic drill. The samples were placed in an ultrahigh-vacuum (UHV) chamber which was baked at 170 °C for more than 24 h resulting in a base pressure less than 5×10^{-11} mbar. Our vacuum chamber is equipped with standard surface science preparation, deposition, and analysis instrumentation,¹⁴ an *in situ* surface magneto-optic Kerr effect light scattering station and is mechanically connected to a modified Vacuum Generators HB501-S Ultrahigh-vacuum (UHV) STEM. This UHV instrument has been constructed for *in situ* processing and subsequent surface observation with nanometer resolution secondary electron (SE) and Auger electron microscopy.

SE microscopy (100 keV and ~10 pA incident beam current), using a through-the-lens detection scheme,¹⁵ performed before and after radiatively annealing the $\text{CaF}_2/\text{Si}(111)$ substrates at 300 °C for 60 min, revealed that areas of obvious surface contamination were not reduced by heating. Broad-beam Auger electron spectroscopy (AES) displayed no statistically significant changes in the chemical composition of the CaF_2 surface after annealing for 60 min at temperatures up to 400 °C. Higher annealing temperatures do, however, produce significant changes in the surface morphology. These changes have been observed with SE microscopy. An unannealed $\text{CaF}_2/\text{Si}(111)$ specimen is shown in Fig. 1(a). The saw-toothed step edge visible in Fig. 1(a) is a typi-

FIG. 2. Secondary electron images of an (a) unrelaxed and a (b) relaxed 10 nm thick CaF_2 film grown on $\text{Si}(111)$. Parallel step edges are a typical surface feature for unrelaxed films, while saw-toothed step edges dominate the surface of relaxed films. Dark and light bands which cover the relaxed film shown in (b) result from secondary electrons generated at the CaF_2 -Si interface. These bands remain unchanged as they pass through the saw-toothed step edges and are also nearly equally spaced to the parallel steps observed in (a).

cal surface feature of the many relaxed samples that were observed. Stress relief during growth results in misfit dislocations at the CaF_2 - $\text{Si}(111)$ interface.¹¹ These dislocations greatly affect the growth of subsequent CaF_2 layers. A triangular array of edge dislocations, comprising the three possible dislocations with $1/6\langle 112 \rangle$ Burgers' vectors, yields the observed triangular step edges for CaF_2 films that have reverted to the bulk-like, undistorted phase. As an example, Fig. 1(b) illustrates that after a 60 min, 400 °C anneal, numerous, almost triangularly arranged pits are formed. These morphological changes may have resulted from the relief of stresses present during the growth of the CaF_2 .¹⁶ In contrast, unrelaxed specimens of a similar thickness do not exhibit such dramatic morphological changes upon annealing to 400 °C, as compared to the relaxed specimens. Unrelaxed, tetragonally distorted CaF_2 films result in a nearly parallel and regularly spaced array of line defects. The line defects arise from the $\frac{1}{3}[111]$ steps (0.31 nm) initially present on the $\text{Si}(111)$ substrates with small miscut angles ($<1^\circ$).

In order to prevent severe surface modifications (pitting) during cleaning, the substrates were either annealed for 60 min at 300 °C or for 24 h at 170 °C prior to the Fe deposition. Two clean $\text{CaF}_2/\text{Si}(111)$ surfaces are shown in Fig. 2. Figure 2(a) reveals the relatively parallel step edges that are commonly observed on an unrelaxed CaF_2 surface. These

steps are typically separated by 25–75 nm. Although the structure of step edges on a relaxed CaF_2 surface is generally linear and parallel, high-resolution SE microscopy reveals jagged, saw-toothed detail along these edges, as depicted in Fig. 2(b). In addition, bands of dark and light contrast are seen to follow the step edges on the relaxed CaF_2 surfaces. These bands are approximately the same width as the separation between step edges observed on unrelaxed surfaces [Fig. 2(a)]. This contrast does not appear to be a surface feature, but may be the result of secondary electrons generated at the CaF_2 -Si interface. Research conducted with submicrometer size MgO cubes has shown that step edges can be observed at the adsorbate-substrate interface through 40 nm of insulating MgO.¹⁷ This data is consistent with a published value of 75 nm for the maximum escape depth of secondary electrons in insulators.¹⁹ The penetration depth of 100 keV incident electrons is extremely large ($\gg 1 \mu\text{m}$) compared to the CaF_2 overlayer thickness (0.01 μm). Since the escape depth of secondary electrons in insulators is large, secondary electrons generated at the CaF_2 -Si interface may be detected. This signal provides information about the insulator-semiconductor interface. The dark and light bands commonly pass (unchanged) through the saw-toothed step edges [Fig. 1(a)] and contaminated regions. This is an indication that the contrast bands are not due to surface effects, rather, they originate at the CaF_2 -Si interface. The density of dark and light bands is consistent with the step density formed on Si(111) surfaces miscut by less than 0.5° from the [111] direction.

III. Fe DEPOSITION

Obvious contamination occupied small, localized regions of the total CaF_2 surface area (10%–30%), such that Fe island size distributions could be determined from regions between the contaminated areas. Fe was deposited at a rate of 0.12–0.19 ML/min [$1 \text{ (ML)} = 7.7 \times 10^{14} \text{ atom/cm}^2$] using an electron beam evaporator. The evaporation rate was measured by Rutherford backscattering, AES,¹⁴ and quartz-crystal microbalance techniques. The base pressure of the system was less than 5×10^{-11} mbar but increased to 2×10^{-9} mbar during Fe growth. The substrates were held at a constant temperature between 20 and 400 °C.

The initial stage of Fe/ CaF_2 growth proceeds by three-dimensional islanding on both relaxed and unrelaxed CaF_2 surfaces. Figure 3(a) is an example of $\Theta = 7.5$ ML of Fe deposited (rate = 0.12 ML/min) on a relaxed, room temperature substrate. The relatively even distribution of 2.0 nm diameter Fe islands on a 10-nm-thick CaF_2 (111) surface is clearly displayed. Inset in Fig. 3(a) is the corresponding Fe island size distribution. Similarly, the unrelaxed 10-nm-thick CaF_2 film shown in Fig. 3(b) yielded a statistically equivalent Fe island distribution for $\Theta = 7.6$ ML (rate = 0.17 ML/min) of Fe grown at room temperature. Particle size analysis of the SE images revealed no statistical difference between the diameters and spatial distribution of Fe islands grown on CaF_2 /Si(111) substrates held at room temperature through 300 °C. A post-growth anneal of 140 °C on room temperature grown films did not produce a noticeable change in the Fe island size distribution. Upon further deposition, the Fe

36p

FIG. 3. A (a) $\Theta = 7.5$ ML and (b) $\Theta = 7.6$ ML Fe film grown on room temperature. (a) relaxed and (b) unrelaxed CaF_2 /Si(111) produces an equivalent well-defined Fe island distribution for both surfaces. The ordinate and the abscissa of the inset histogram in (a) are "number of Fe islands" and "diameter of Fe islands (nm)," respectively. The vertical scale varies from 0 to 25 while the horizontal scale extends from 0 to 5. For greater coverages, such as $\Theta = 21.4$ ML shown in (c), the Fe film results in a percolation network. Part of a saw-toothed step edge is visible in the upper left corner of (a). The ~ 4 nm black region in the upper center portion of (a) is a pinhole. A nonexistent denuded zone surrounding this area indicates that few, if any, Fe atoms pass through the pinhole.

films form a percolation network of Fe islands rather than increasing the average Fe island diameter. For the purpose of comparison, the resulting island percolation network for $\Theta = 21.4$ ML of Fe on unrelaxed, room temperature CaF_2 is shown in Fig. 3(c).

Statistical analysis performed on a large variety of images yielded the following information for Fe coverages between 7 and 8 ML grown on CaF_2 /Si(111) substrates maintained at a constant temperature of 20 °C through 300 °C: (1) An average Fe island diameter of 2.0 ± 0.3 nm; (2) a range of Fe island diameters where 85% of the population will lie

within 2.0 ± 1.0 nm; (5) an average Fe island separation of 2.0 ± 0.4 nm; (6) a 23% coverage of $\text{CaF}_2(111)$ with Fe islands; (7) the number of Fe islands per unit area is 7.4×10^{12} islands/cm²; (8) the mean distance between Fe island centers is approximately 3.7 ± 0.6 nm; (9) no geometric ordering of the islands was observed based on fast Fourier transform image analysis.

Figure 4 exhibits the island distributions on four different $\text{CaF}_2/\text{Si}(111)$ surfaces held at various temperatures during Fe growth. All of the CaF_2 films are approximately 10 nm in thickness and covered with $\Theta = 7-8$ ML of Fe. All of these films were observed at room temperature. Figures 4(a)-4(d) are SE images taken of surfaces which were grown while the substrates were held at a temperature of 20, 140, 300, and 400 °C, respectively. As can be seen in Figs. 4(a)-4(c), the Fe island size and spatial distributions are nearly identical for Fe films grown on substrates held between room temperature and 300 °C. Higher substrate temperatures, such as 400 °C, yielded a more mottled surface with greater separation between Fe islands of a similar size, as is evident in Fig. 4(d). CaF_2 decomposition at 400 °C [as already shown in Fig. 1(b)], rather than an increase in Fe adatom diffusion length, is responsible for the modified nucleation density. The lack of a temperature dependence on the Fe island size and spatial distributions, for those films grown between 20 and 300 °C, implies that the island nucleation density is not determined by a diffusion length. A more probable explanation for the temperature independent distribution is the existence of Fe-receptive chemical bonds or atom-trapping defects on the substrate. The island diameter grows once a single adsorbate atom nucleates at one of these sites. Island growth occurs because the available atomic sites have become saturated and the Fe atoms are able to travel to and bond with pre-existing Fe islands.¹⁹ The production of labyrinthian structures at higher coverages, rather than larger islands, is consistent with the fact that diffusion lengths for Fe on Fe are larger than the mean Fe island size.

We are interested in assessing the feasibility of fabricating nanometer-dimension micromagnetic devices integrated into Si-based technology, and hence, we consider the magnetic properties of these films. A simple energy calculation indicates that a hemispherically shaped, unstressed, and magnetically ordered Fe particle must contain a single magnetic domain for diameters on the order of a few tens of nanometers. This transition is a result of domain formation becoming energetically unfavorable as the magnetic particle becomes smaller due to the domain boundary energy becoming a large percentage of the total energy. The islands observed in Figs. 3(a) and 3(b) are smaller than the critical single domain size and separated by less than the mean-free path of conduction electrons in metals (near 30 nm at room temperature for Cu²⁰). These properties make this system of nanometer-sized Fe islands on an insulator, when covered by a noble metal, an excellent candidate for room-temperature giant magnetoresistance (GMR) studies.^{21,22}

Due to field limitations, *in situ* surface magneto-optic Kerr effect (SMOKE) measurements were unsuitable in the detection of a magnetic signal for this metal/insulator system. Our facility is capable of detecting magnetization varia-

47.6p

FIG. 4. Fe island distributions for four different $\text{CaF}_2/\text{Si}(111)$ s held at a constant temperature of (a) 20, (b) 140, (c) 300, and (d) during growth. All of the CaF_2 films are approximately 10 nm : covered with $\Theta = 7-8$ ML of Fe. A relaxed CaF_2 film was used as a in (b). Lack of temperature dependent Fe island distributions fo ($20^\circ\text{C} < T < 300^\circ\text{C}$) indicates that Fe atom mobility is not diffu uted during growth. CaF_2 decomposition at higher temperatures : sible for the change in nucleation density observed in (d).

FIG. 5. Secondary electron formed under the same conditions as Fig. 3(a) but in a region where some CaF_2 has locally lifted off of the $\text{Si}(111)$ substrate. Fe islands are visible on the $\text{CaF}_2/\text{Si}(111)$ surface (top), the oxidized $\text{Si}(111)$ surface (bottom), and the inverted CaF_2 surface (right). A qualitative difference in Fe mobility can be realized by comparing the mean interisland separation in the top and bottom regions.

tions resulting from Fe thickness changes as small as 0.22 Å for ultrathin films of face-centered-cubic $\text{Fe}/\text{Cu}(100)$.¹⁴ Therefore, since no signal was detected, we conclude that ferromagnetism in the island array is not present. A simple Langevin paramagnetism calculation indicated that a superparamagnetic signal would not be apparent using our maximum applied magnetic field of approximately 1 kOe for islands with a diameter less than 2.8 nm, hence, we are not able to distinguish between super-paramagnetic and nonmagnetic behavior. This would imply that a larger field and more sensitive detection equipment (as with a SQUID) is necessary to observe the expected Fe island superparamagnetic behavior. Research in our laboratory concerned with covering the Fe islands with a noble metal, such as Ag, has recently begun. Preliminary results indicate a significant enhancement of the superparamagnetic signal after Ag has been deposited *in situ*. This enhancement may result from an increased effective island size or an increase in the average magnetic moment per Fe island. Although not shown, SE microscopy performed after the Ag deposition revealed that the Ag formed islands on top of the $\text{Fe}/\text{CaF}_2/\text{Si}(111)$ surface. These new, larger Ag islands may serve to thermally stabilize the effective magnetic moment of the many smaller Fe islands which were enveloped. The result of thermal stability at the same measurement temperature (20 °C) is consistent with the observed superparamagnetic response from the larger Ag/Fe islands.

Occasionally, CaF_2 defects that are approximately 100 nm in width are observed during electron microscopy. Figure 5 displays a SE image of Fe islands on a 10-nm-thick relaxed $\text{CaF}_2/\text{Si}(111)$ surface and an oxidized $\text{Si}(111)$ surface. The oxidized Si region is visible because the CaF_2 had locally lifted off of the Si crystal, perhaps during 3 mm disk preparations. The existence of Fe islands on the SiO_2 region, while also possessing a similar diameter as those on the CaF_2 region, suggests that the thermodynamically favorable reaction of iron silicide formation did not occur with the insulating and less reactive SiO_2 surface. The qualitative difference in Fe mobility for the two distinct regions is made apparent by

the difference in mean inter-island separation. In addition, the position stability of the Fe islands shown in Fig. 5 was monitored as a function of electron-beam exposure. A SE image formed by subtracting two images of the same area taken after a total electron dose of 6000 C/cm^2 revealed that the Fe islands remained fixed in position on both the CaF_2 and the SiO_2 regions.

Although the Fe island distributions are due to chemical or defect dominated growth, Fe is not expected to form compounds with CaF_2 . Thermochemical considerations reveal that Fe is much less reactive with CaF_2 than with NaCl .²³ Wassermann *et al.* and Matthews²⁴ found that the Fe/NaCl system does not initiate compound formation at the interface, hence, there is a high probability of maintaining chemically distinct Fe and CaF_2 regions when Fe is deposited under UHV conditions on CaF_2 substrates held at or below 700 °C. This does not preclude the existence of other channels for Fe compound formation. For example, it is possible that the 10-nm-thick CaF_2 does not completely inhibit iron silicide formation. Pinholes, located within the CaF_2 film, may be a conduit for mass transfer. Although black, round-shaped regions (pinholes) were observed via SE microscopy, the absence of denuded zones surrounding these black areas and the resulting uniform Fe island distribution over the complete CaF_2 surface seems to suggest little, if any, chemical reactivity [see the ~4 nm dark, triangular region near the top of Fig. 3(2)]. Nonetheless, based on a hemispherical model of Fe islands, particle size analysis implies that at least 20% of the Fe is unaccounted for. This deficiency may be attributed to the model employed. Cylindrical-shaped islands with an axis length equal to the radius would enclose a volume 50% larger than a hemispherical island of the same radius. Certainly, islands which are slightly hemispherical at the top and cylindrical at the base would indicate that all the Fe is, in fact, accounted for. Another possible explanation for the apparent absence of Fe could be that the film actually grows in the Stranski-Krastanov mode. The first ML may form a continuous film but later, as the depositions continue, develops into a mostly islanded system. These islands then allow for contrast due to topography and are observed in the SE images. Due to the electron-beam-induced damage caused by the incident electron probe and a proportionally small number of Auger electrons (within an energy window) relative to the total number of emitted secondary electrons, high-resolution Auger electron microscopy was not sensitive enough at low electron doses to determine whether or not the first ML was, in fact, continuous rather than islanded.

IV. ELECTRON IRRADIATION AND PATTERN FORMATION

The effects on film morphology due to electron-beam exposure before and after Fe deposition were explored. Unrelaxed 10-nm-thick CaF_2 films were selectively irradiated with 8.2–140 pA, 100 keV electrons. The intent was to preferentially grow nanoscale structures by changing the surface energy of the substrate through the conversion of CaF_2 into a metallic, higher surface energy, Ca-rich surface.¹⁰ As a result, the growth mode of the Fe would then be modified in the irradiated regions.

FIG. 6. Pregrowth electron-beam irradiated regions were observed at lower magnification (a) before and (b) after $\Theta = 21.4$ ML of Fe had been deposited. These equivalent regions of the same crystal display large differences in secondary electron contrast. Surface imperfections located at the lower left of (a) were no longer visible after the Fe deposition (b). In contrast, electron-beam exposed regions remain apparent before and after the Fe deposition. The two right-most irradiated regions in (a) best reveal the proximity effects of electronic charge dissipation. A pre-growth electron dose of 5.78 C/cm^2 changes the Fe film's morphology, as depicted in (c). The much more distinct and separated region of (c) below the dashed, white line was not exposed to irradiation prior to the Fe growth, as had the upper region. The top-most area of (c) is slightly more continuous and less distinct because of the morphological changes that resulted from the 100 keV, 140 pA pre-growth electron irradiation.

Figure 6(a) displays the decreased secondary electron yield for eleven regions which were methodically dosed with 100 keV, 140 pA electrons. From left to right, the charge per unit area impinged upon the sample was 1.44, 5.78, 2.89, 4.81, 7.22, 14.4, 14.4, 28.9, 57.8, 144, and 217 C/cm^2 . The two right-most irradiated regions best reveal the proximity effects of electronic charge dissipation. Proximity effects adjacent to exposed regions obfuscate the comparison between unexposed and exposed film morphology. As depicted in Fig. 6(b), a $\Theta = 21.4$ ML deposition of Fe greatly diminishes image contrast. Although Figs. 6(a) and 6(b) were acquired at the same location, surface imperfections which were visible on the clean CaF_2 surface became imperceptible after the Fe was deposited. The Fe did not, however, mask the presence of the pre-growth irradiated areas. Figure 6(c) illustrates the results of a pre-growth electron dose of 5.78 C/cm^2 on the Fe film morphology. The surface structure shown in the lower portion of the image (below the dashed line), which was not

FIG. 7. Secondary electron images depict the pre-growth and post-growth electron-beam induced effects on Fe film morphology. A $\text{CaF}_2/\text{Si}(111)$ film was selectively exposed to 4.56 C/cm^2 of electron irradiation prior to the Fe growth. This region is enclosed by the dotted white line in (a). After $\Theta = 7.1$ ML room-temperature deposition of Fe, most of the substrate surface is covered with 2-nm-diam Fe islands. The region which had been irradiated before the Fe growth, however, is much more continuous than the surrounding area. A post-growth electron dose of 355 C/cm^2 (enclosed by the dashed white line) greatly affected the Fe film morphology for regions that had not been irradiated before growth (B). Conversely, post-growth irradiation did not affect the Fe film morphology for areas which had been exposed to electron irradiation prior to the Fe growth (A). A lower magnification secondary electron image of (a) is shown in (b). Two complete regions of pre-growth irradiation are visible in (b). A step edge which runs nearly vertical can be seen to the left of the center-most irradiated region in (b).

exposed to irradiation, appears more distinct and separated than the upper region.

As a second example, a $\Theta = 7.1$ ML film of Fe grown on a room-temperature $\text{CaF}_2/\text{Si}(111)$ substrate, which had been patterned with an electron beam, produced a uniform distribution of Fe islands over most of the CaF_2 surface. This film also displayed an expected change in morphology for those regions which had been irradiated with more than 1.14 C/cm^2 before the Fe deposition. Figure 7(a) portrays the effects of pre-growth and post-growth electron irradiation effects on the Fe film's morphology. The lower left portion of Fig. 7(a) (enclosed by the dotted white line) is a region which had been subjected to 4.56 C/cm^2 before the Fe growth. The Fe on the pre-growth exposed region is much more continuous than on the region which was not exposed. The contrast observed for this region may be due to island formation atop a continuous ultra-thin film of Fe. If, for example, the pre-growth exposed region consisted of islands on a finer scale it would be expected that the film would

suffer similarly to the effects of post-growth electron irradiation, as is evident near the center of Fig. 7(a). The area within the dashed white line of Fig. 7(a) was subjected to 355 C/cm^2 of electron irradiation following the Fe deposition. By comparing the intersection of the two highlighted regions (A) with that of the remaining area within the dashed white line (B), qualitative arguments of Fe island position stability can be set forth. The pregrowth irradiated area (A) is more stable to post-growth electron irradiation. In fact, very little morphological change is observed for the pregrowth irradiated area except near the border of the dosed/undoped region. The occurrence of more damage near the edges is simply due to an insufficiently distinct separation of the two regions during exposure. Electronic charge dissipation and mechanical instabilities (over the course of several tens of minutes) allowed slightly more area to be affected by the electron beam than intended. Figure 7(b) is a lower magnification SE image obtained immediately after Fig. 7(a). Two complete regions of pregrowth irradiation are visible along with part of a third area. Since insulators generally have higher secondary electron yields than metals,²⁵ the regions of pregrowth irradiation which are now more metallic (due to the fluorine desorption) appear darker than the surrounding areas. The brighter region in the center of Fig. 7(b) is due to post-growth electron irradiation and was formed when the image shown in Fig. 7(a) was obtained. This bright contrast, though not always observed, probably results from a redistribution of CaF_2 under specific post-growth electron exposures. As stated earlier, high-resolution Auger electron microscopy would, in this case, drastically change the surface before an adequate analysis of the surface chemical composition could be ascertained. Only for greater coverages, such as a $\Theta=21.4 \text{ ML}$ film, does post-growth electron-beam-induced damage remain negligible. For instance, both the pregrowth exposed region and the unexposed region of the $\Theta=21.4 \text{ ML}$ Fe film shown in Fig. 6(c) were able to withstand 343 C/cm^2 of post-growth electron irradiation with no obvious morphological change, unlike what was observed for the $\Theta=7.1 \text{ ML}$ (355 C/cm^2) regime shown in Fig. 7(a).

We have shown that pregrowth (100 keV, 8.2–140 pA) electron irradiation doses as low as 1.14 C/cm^2 altered the Fe film morphology on selectively irradiated regions of $\text{CaF}_2/\text{Si}(111)$. Post-growth electron irradiation inflicts much less damage on pregrowth irradiated regions as compared to areas that were not exposed. Proximity effects limited the minimum size of selectively irradiated regions. Although the nucleation of Fe films on nonirradiated surfaces were not drastically different in morphology from those irradiated with the electron beam, our studies on the $\text{Fe}/\text{CaF}_2/\text{Si}(111)$ system have laid the foundation for future research into electron-beam induced preferential nucleation and growth. A systematic study is currently under way to further investigate the effectiveness of creating nanometer-sized magnetic structures on other insulating materials which are easily decomposed by electron-beam irradiation.

V. CONCLUSIONS

Fe was deposited (0.12–0.19 ML/min) onto electron-beam modified and unmodified $\text{CaF}_2/\text{Si}(111)$ substrates so

that the efficacy of patterning mesoscopic magnetic devices on Si-based substrates could be determined. Relaxed films yielded saw-toothed step edges while unrelaxed films resulted in parallel step edges separated by 25–75 nm. A narrow size distribution of 2.0-nm-diam Fe islands was grown on 10-nm-thick films of relaxed and unrelaxed $\text{CaF}_2/\text{Si}(111)$ surfaces held at or near room temperature ($20^\circ\text{C} < T < 300^\circ\text{C}$). An observed temperature independence of Fe island distributions over this range denies the existence of diffusion limited growth. Chemical or defect dominated nucleation is thought to be the controlling factor for growth of Fe on $\text{CaF}_2/\text{Si}(111)$. This system, an arrangement of possibly single domain particles separated by less than the mean-free path of conduction electrons in metals, is an exciting new candidate for GMR studies. Fe coverages of $\Theta=21.4 \text{ ML}$ produced a percolation network of connected islands rather than a continuous film covering the CaF_2 surface. Pregrowth (100 keV, 8.2–140 pA) electron irradiation as low as 1.14 C/cm^2 altered the Fe film morphology on the selectively irradiated regions. Areas dosed with electron irradiation prior to Fe growth were more stable to the damaging effects of post-growth electron irradiation as compared to regions that had not been exposed. Further work must be completed to determine whether the Fe is magnetic, affected by the inherent oxygen contamination, chemically separated from the Si, and controllable so that various size islands may be formed by changing the deposition rate, substrate temperature, substrate surface energy, and quantity of Fe deposited.

The authors wish to acknowledge thoughtful discussions with D. Loretto, J. Venables, J. Drucker, P. Bennett, and W. Penuskey. We are also indebted to D. Loretto of Lawrence Berkeley Laboratory for supplying the $\text{CaF}_2/\text{Si}(111)$ samples. This work is supported by the Office of Naval Research under grant No. N00014-93-1-0099. The microscopy was performed at the National Science Foundation supported Center for High Resolution Electron Microscopy at Arizona State University, grant No. DMR-91-15680.

¹ T. Sakaguchi, M. Watanabe, and M. Asada, *IEICE Trans. E* 74, 3326 (1991).

² M. Watanabe, T. Suemasu, S. Muratake, and M. Asada, *Appl. Phys. Lett.* 62, 300 (1993).

³ S. Muratake, M. Watanabe, T. Suemasu, and M. Asada, *Electron. Lett.* 28, 1002 (1992); T. Suemasu, M. Watanabe, M. Asada, and N. Suzuki, *Electron. Lett.* 28, 1432 (1992).

⁴ T. P. Smith, J. M. Phillips, W. M. Augustyniak, and P. J. Stiles, *Appl. Phys. Lett.* 45, 907 (1984).

⁵ L. J. Schowalter and R. W. Fathauer, *CRC Crit. Rev. Solid State Mater. Sci.* 15, 367 (1989).

⁶ E. Schloemann, R. Tustison, J. Weissman, H. J. Van Hook, and T. Varitimos, *J. Appl. Phys.* 63, 3140 (1988).

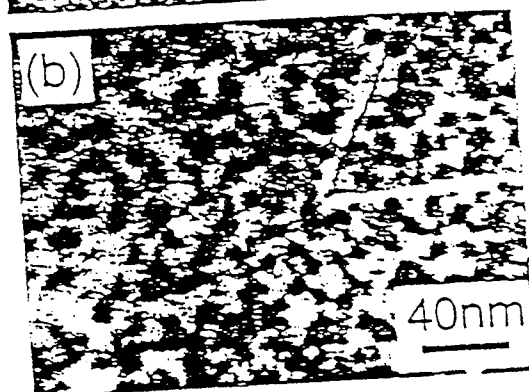
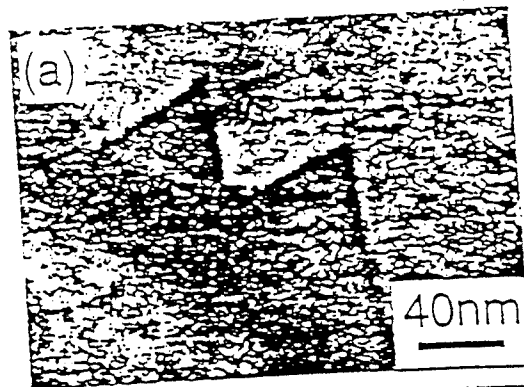
⁷ E. Bauer, *Z. Krist.* 110, 372 (1958).

⁸ F. R. de Boer, R. Boom, W. C. M. Matens, A. R. Miedema, and A. K. Niessen, *Cohesion in Metals Transition Metal Alloys* (North-Holland Elsevier Science, New York, 1988).

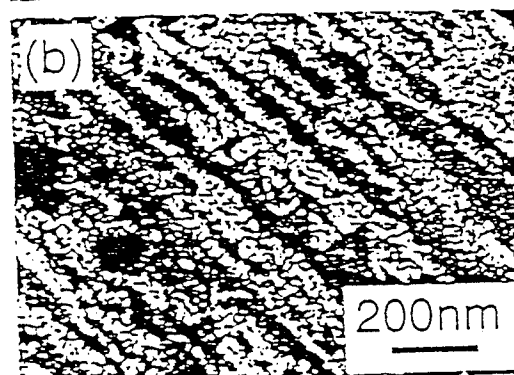
⁹ J. J. Gilman, *J. Appl. Phys.* 31, 2208 (1960); G. C. Benson and T. A. Claxton, *Can. J. Phys.* 41, 1287 (1963); P. W. Tasker, *J. Phys. (Paris)* 41, C6-488 (1980).

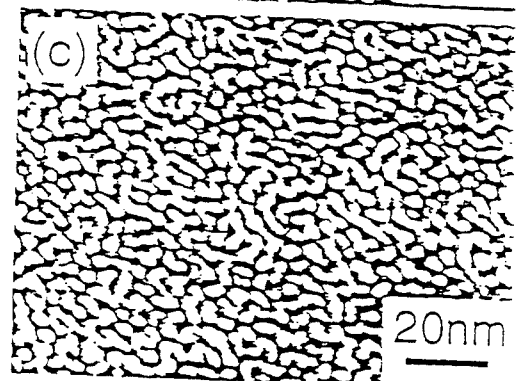
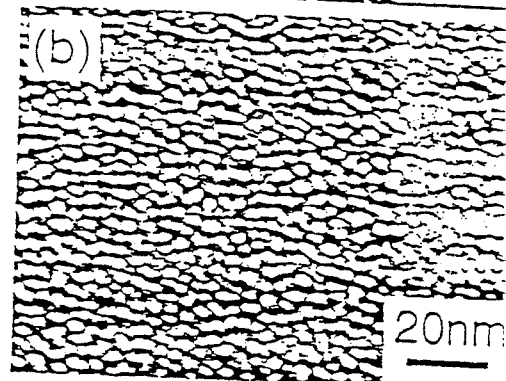
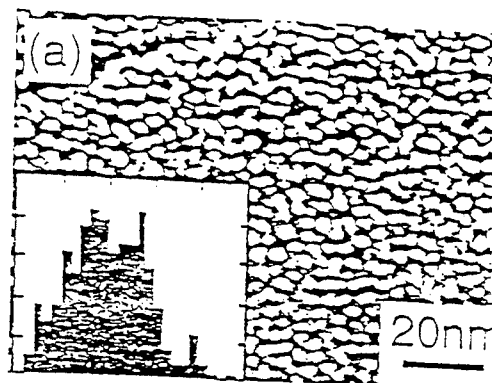
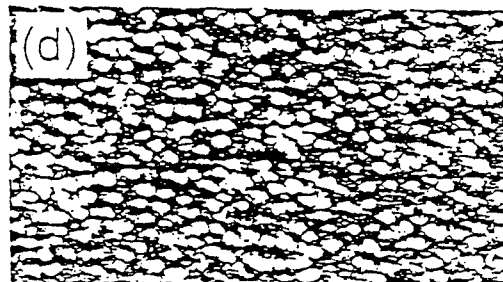
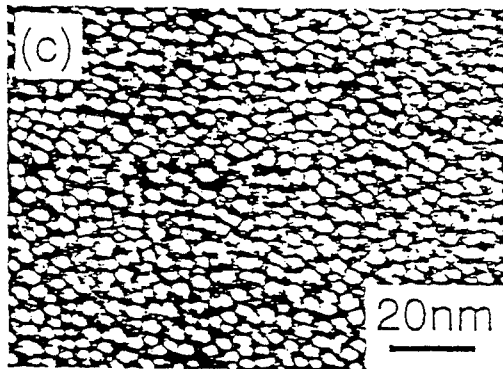
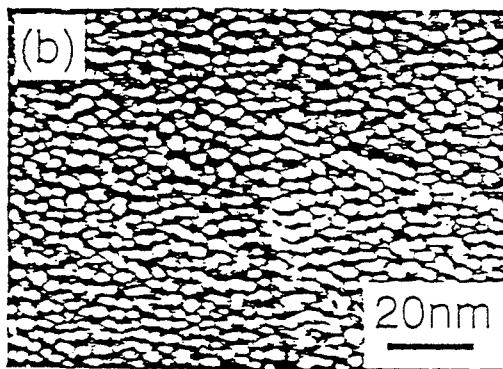
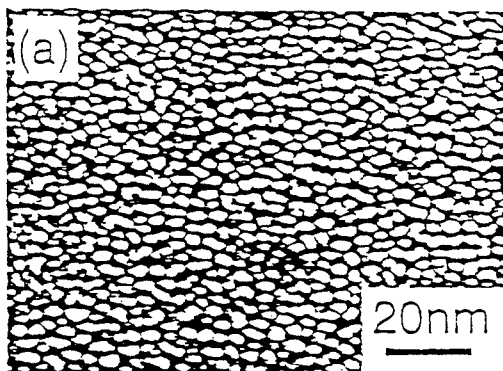
¹⁰ T. R. Harrison, P. M. Mankiewich, and A. H. Dayem, *Appl. Phys. Lett.* 41, 1102 (1982); P. M. Mankiewich, H. G. Craighead, T. R. Harrison, and A. H. Dayem, *Appl. Phys. Lett.* 44, 468 (1984); M. Scheinfein and M. Isaacson, *J. Vac. Sci. Technol. B* 4, 326 (1986); S. Kanemaru, H. Ishiura, and

- S. Furukawa, *J. Appl. Phys.* 63, 1060 (1988); A. Izumi, K. Tsutsui, and S. Furukawa, *J. Appl. Phys.* 75, 2307 (1994).
- ¹¹ C. A. Lucas and D. Loreto, *Appl. Phys. Lett.* 60, 2071 (1992); C. A. Lucas, G. C. L. Wong, and D. Loreto, *Phys. Rev. Lett.* 70, 1826 (1993); G. C. L. Wong, D. Loreto, E. Rotenberg, M. A. Olmstead, and C. A. Lucas, *Phys. Rev. B* 48, 5716 (1993).
- ¹² One $\text{CaF}_2(111)$ triple layer (TL) represents the F-Ca-F repeat unit in the $[111]$ direction. Each triple layer contains 7.735×10^{14} Ca atom/cm² and 1.547×10^{15} F atom/cm².
- ¹³ The $\text{CaF}_2/\text{Si}(111)$ samples were kindly provided by D. Loreto of Lawrence Berkeley Laboratory.
- ¹⁴ K. R. Heim, S. D. Healy, Z. J. Yang, J. S. Drucker, G. G. Hembree, and M. R. Scheinfein, *J. Appl. Phys.* 74, 7422 (1993).
- ¹⁵ P. Kruit and J. A. Venables, *Ultramicroscopy* 25, 183 (1988); P. Kruit, *Adv. Opt. Electron Microsc.* 12, 93 (1991); G. Hembree, J. Drucker, C. Luo, M. Krishnamurthy, and J. Venables, *Appl. Phys. Lett.* 58, 1890 (1991); G. G. Hembree and J. A. Venables, *Ultramicroscopy* 47, 109 (1992); J. Liu, G. G. Hembree, G. E. Spinnler, and J. A. Venables, *Surface Science Lett.* 262, L111 (1992); J. Liu, G. G. Hembree, G. E. Spinnler, and J. A. Venables, *Catalysis Lett.* 15, 133 (1992).
- ¹⁶ Private communication with D. Loreto: Bright field transmission electron microscopy performed on the $\text{CaF}_2/\text{Si}(111)$ samples revealed a non uniform distribution of line defects at the CaF_2 - $\text{Si}(111)$ interface for some of the samples. This is an indication that stress relief occurred during the CaF_2 growth. In comparison, an unrelaxed film will display a parallel array of line defects corresponding to the original steps on the $\text{Si}(111)$ surface.
- ¹⁷ J. Liu, G. G. Hembree, G. E. Spinnler, and J. A. Venables, *Ultramicroscopy* 52, 369 (1993).
- ¹⁸ H. Seiler, *J. Appl. Phys.* 54, R1 (1983).
- ¹⁹ More specific details about the growth mechanisms for this system will be published in a subsequent paper by K. R. Heim, G. G. Hembree, M. R. Scheinfein, and J. A. Venables.
- ²⁰ C. Kittel, *Introduction to Solid State Physics*, 4th ed. (Wiley, New York, 1971), p. 259.
- ²¹ J. Q. Xiao, J. S. Jiang, and C. L. Chien, *Phys. Rev. Lett.* 68, 3749 (1992).
- ²² C. L. Chien, *J. Appl. Phys.* 69, 5267 (1991); A. E. Berkowitz, J. R. Mitchell, M. J. Carey, A. P. Young, S. Zhang, F. E. Spada, F. T. Parker, A. Hutten, and G. Thomas, *Phys. Rev. Lett.* 68, 3745 (1992); A. E. Berkowitz, J. R. Mitchell, M. J. Carey, A. P. Young, D. Rao, A. Start, S. Zhang, F. E. Spada, F. T. Parker, A. Hutten, and G. Thomas, *J. Appl. Phys.* 73, 5320 (1993); K. R. Coffey, T. L. Hylton, M. A. Parker, and J. K. Howard, *Appl. Phys. Lett.* 63, 1579 (1993).
- ²³ Calculations were made to determine the change in the Gibbs energy during formation reactions of Fe with CaF_2 and Fe with NaCl (both at 700 and 1000 K). The results indicate that a chemical reaction beginning with gaseous reactants is more likely than those beginning with solid reactants, although both cases favored an Fe-NaCl reaction over an Fe- CaF_2 reaction. This, coupled with the fact that NaCl has a much higher vapor pressure than CaF_2 (3.2×10^{-7} vs 5.4×10^{-22} at 700 K and 3.4×10^{-2} vs 1.9×10^{-10} at 1000 K, with pressure in mbars), suggests that a gaseous reaction involving NaCl is more probable than that with CaF_2 .
- ²⁴ E. F. Wassermann and W. Sander, *J. Vac. Sci. Technol.* 6, 537 (1969); J. W. Matthews, *J. Vac. Sci. Technol.* 3, 133 (1966).
- ²⁵ G. W. Goetze, A. H. Boerio, and M. Green, *J. Appl. Phys.* 35, 482 (1964); G. W. Goetze, *Adv. Electron. Electron Phys.* 22, 219 (1968).

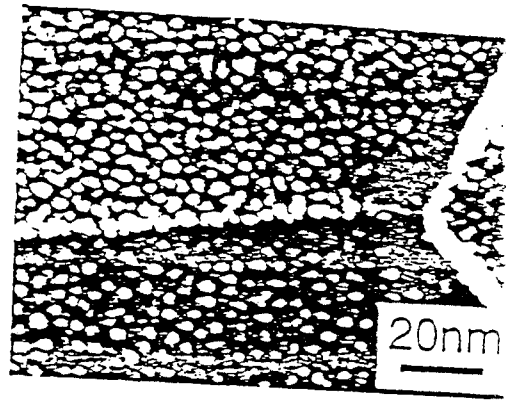


JAP/047424/Fig 1/100 HT

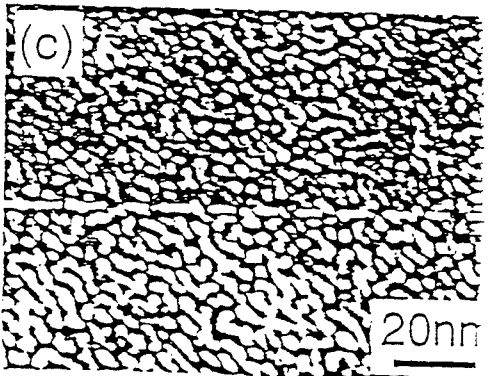
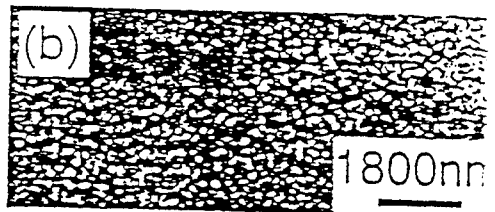
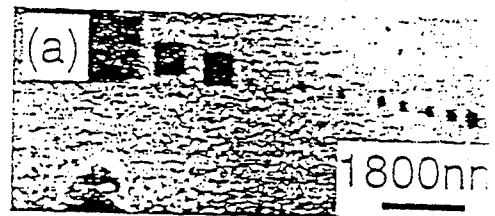
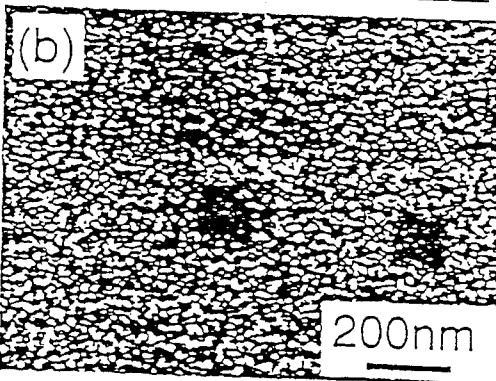
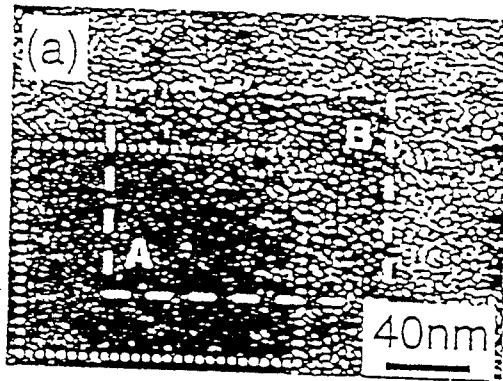




JAP/047424/E63/1001



JAP/047424/F65/100/



90° domains in Co/Cu giant magnetoresistance superlattices

Z. J. Yang and M. R. Scheinfein^{a)}

Department of Physics and Astronomy, Arizona State University, PSF-470 Box 871504,
Tempe, Arizona 85287-1504

(Received 29 August 1994; accepted for publication 4 November 1994)

The magnetic properties of Co/Cu superlattices grown in a dual-beam electron evaporation chamber have been investigated with the three-axis magneto-optical Kerr effect and magnetoresistance measurements. The magnetoresistance oscillates with a period of about 1 nm as a function of the Cu layer thickness. The magnitude of the component of the magnetization perpendicular to the field direction oscillates with the same period. The total magnetization, calculated from the two in-plane hysteresis loops, is used to determine that 90° domains are formed between ferromagnetic Co layers across the Cu spacer layers in the superlattice. The correlations between the 90° magnetization curves and magnetoresistance measurements suggest that the giant magnetoresistance in superlattices with imperfect interfaces results from the 90° orientation of domains within adjacent Co layers. © 1995 American Institute of Physics.

The strength and sign of the interlayer coupling coefficient in superlattices composed of ferromagnetic transition metals and nonmagnetic spacer layers has been correlated with magnetotransport measurements for a wide class of systems.¹ Experiments have been focused on the bcc Fe/Cr² and the fcc Co/Cu systems³⁻⁵ in an effort to confirm quantitative predictions on the orientation dependence of the interlayer coupling.⁶ Models based on Ruderman-Kittel-Kasuya-Yosida-like treatment which couple spanning vectors normal to the superlattice layers that join extremal points of the bulk Fermi surface have successfully predicted the oscillation periods of interlayer coupling. Magnetotransport models which rely on antiferromagnetic alignment of adjacent ferromagnetic layers have been used to interpret experimental data.⁷ Interlayer coupling can be complicated by surface and interface roughness, primarily due to conditions during growth.^{8,9} In addition to antiferromagnetic (or 180°) interlayer coupling, 90° interlayer coupling has been observed in epitaxial systems with wedge-shaped interlayers, including Fe/Cr/Fe(100) and Fe/Au/Fe(100).¹⁰⁻¹² Theoretical treatments attribute intrinsic 90° degree, or biquadratic coupling (which is to be contrasted to 90° domain orientation) between layers to spatial nanoscopic variations in the interlayer coupling arising from thickness variations.^{13,14} Intrinsic bilinear (180°) coupling in general coexists with the higher order biquadratic (90°) coupling.¹⁵ Evidence for 90° domains in the coupling in Co/Cu(001) superlattices has been recently observed in the nonsymmetric spin states from Kerr hysteresis loops at the second antiferromagnetic maximum¹⁶ due to the competing effects of anisotropy and exchange coupling. Elemental specific magnetic hysteresis loops extracted from magnetic circular dichroism experiments from Fe/Cu/Co trilayers indicates the presence of significant misalignment between the orientation of the magnetization in adjacent ferromagnetic layers.¹⁷ In this letter, we demonstrate the strong correlation between giant magnetoresistance (GMR) and 90°

domain formation between adjacent layers in electron beam evaporated Co/Cu superlattices as a function of the Cu interlayer spacing when the interfaces are imperfect.

We have prepared $[\text{Co}_{1.5 \text{ nm}}/\text{Cu}]_n$ ($9 < n < 13$) superlattices by evaporating on Si(100) oriented crystals, ~~Corning cover glass slides and holey carbon film covered grids.~~ 6.0-nm-thick Co layers were grown at 250 °C as buffer layers on the substrates. 4.5-nm-thick Co capping layers covered the superlattices, making the sandwich symmetric. ~~The total superlattice thickness ranged between 40 and 46 nm.~~ In this study all superlattices were grown at room temperature in a dual e-beam ultrahigh vacuum evaporation system. Deposition rates were 0.3–1 Å/s at base pressure 5×10^{-9} mbar. *In situ* thickness calibration using a quartz crystal microbalance was confirmed with Rutherford backscattering.

The crystallographic and superlattice structure was studied with x-ray diffraction (Cu-K_α radiation $\lambda = 0.15405$ nm) and plan-view scanning transmission electron microscopy (STEM). The large angle x-ray scattering data are characterized by a low intensity fcc (111)Co (Cu) peak indicating that the multilayers have a weak (111) out-of-plane texture. The width of this peak was used to estimate an average grain size between 8 and 10 nm, a result confirmed by STEM. Only first- and second-order small angle x-ray scattering (SAXS) peaks with superlattice character Kiessig fringes were observed indicating the interfaces were relatively rough, consistent with the STEM observations. The rms roughness of the interface estimated by fitting the SAXS spectra is ± 0.2 – 0.4 nm.¹⁸ The bilayer thicknesses calculated from SAXS Bragg peaks are in good agreement with the nominal values. ~~The observed broadening of the higher order Bragg peaks and the disappearance of the high-order low angle amplitudes may arise from interfacial interdiffusion and cumulative random variations in layer thickness.~~¹³

Magnetic measurements were made with the combined three-axis magneto-optical Kerr effect (MOKE) on 6-mm-diam circular samples. A detailed description of our MOKE system is given elsewhere.¹⁹ Longitudinal Kerr effect hysteresis

^{a)}Scheinfein@phyast.la.asu.edu

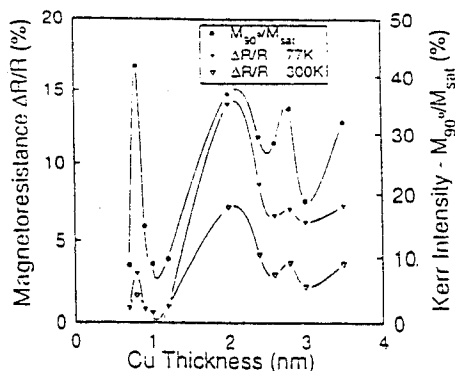


FIG. 1. MR at room temperature (open triangles) and at 77 K (solid triangles) are plotted as a function of the Cu interlayer thickness of the superlattice $[\text{Co}_{1.5}\text{nmCu}_n]_n$ ($9 < n < 13$). The maximum normalized magnetization oriented at 90° with respect to the field direction is also shown $M_{90^\circ}/M_{\text{sat}}$. The oscillations in the 90° oriented magnetization correspond with the oscillations in the MR data.

esis loops were obtained by orienting the superlattice's in-plane easy axis along the applied magnetic field direction in the scattering plane. The longitudinal in-plane magnetization is M_x . In order to obtain the transverse in-plane component of the magnetization, M_y , both the sample and the magnetic field are rotated until both the easy-axis and the applied field direction are perpendicular to the scattering plane. In this orientation, when the field is applied along the in-plane easy axis, the detector records magnetization in the scattering plane, M_y .¹⁹ Without modifying the position of any optical elements, calibrated M_x and M_y components of the magnetization can be recorded during the switching process. The components can be added together in quadrature as a measure of the total magnetization, M_z . When the normalized total magnetization differs from one, there are regions where the magnetization is misaligned. The misalignment can be due to domain formation within a given layer(s) of the superlattice, or may be due to small regions of antialignment between adjacent layers. As the light is attenuated during its traversal of the superlattice, the topmost layers will contribute more strongly to the detected Kerr signal.²⁰ In order to assess effects due to cumulative roughness in layered structures, Kerr effect hysteresis loops were measured from both sides of samples grown on glass substrates. No obvious difference was observed in hysteresis loops measured from the top or the bottom of the superlattice stack. The variation in the absolute value of the Kerr signal as samples are changed and the magnet and sample are rotated is less than 5%.

The MR was measured on both strip-shaped ($5 \times 8 \text{ mm}^2$) and patterned, dumbbell-shaped ($5 \times 0.2 \text{ mm}^2$) samples using the four-probe method at 300 and at 77 K with the field (up to 14 kOe) applied in the plane of film, and the in-plane current both transverse and parallel to the field. For pure Co thin films, anisotropy MR was observed. The maximum transverse MR is only 1% for 30-nm-thick films of pure Co. We define MR as $(R_H - R_{\text{sat}})/R_{\text{sat}}$, where R_{sat} is the saturation high-field resistance.

In Fig. 1, the MR at room temperature (open triangles) and at 77 K (solid triangles) are plotted as a function of the Cu interlayer thickness of the superlattice

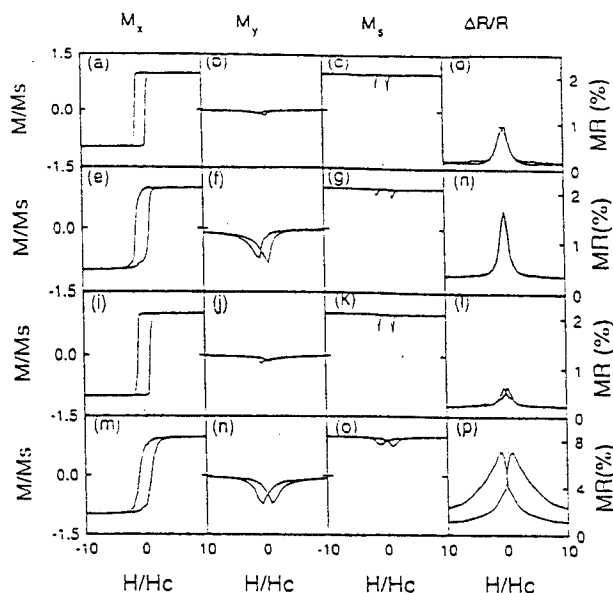


FIG. 2. Components of the magnetization along the easy-axis, M_x , and along the hard axis, M_y , are recorded during the switching process for fields applied along the easy axis. The normalized total (in-plane) magnetization, M_z , results from adding the two in-plane components together in quadrature. The MR data are shown in the far right-hand column. The Cu interlayer thickness is (a)–(d) 0.7 nm, (e)–(h) 0.8 nm, (i)–(l) 1.0 nm, and (m)–(p) 2.0 nm. $H_c = 35$ Oe, such that the maximum range on all plots is ± 350 Oe.

$\text{Co}_{4.5}\text{nm}[\text{Co}_{1.5}\text{nmCu}_n]/\text{Co}_{6.0}\text{nm}/\text{Si}(100)$ ($9 < n < 13$). The oscillation period of interlayer coupling is about 1 nm, within the accepted range of Cu spacer thickness values given the accuracy of our thickness calibration. Evident is the suppression of the first MR maximum and a reduction in the value for the MR,^{3,4} characteristic of films with rough interfaces.³ The maximum normalized magnetization oriented at 90° with respect to the field direction, M_y (or $M_{90^\circ}/M_{\text{sat}}$) is also shown. The peaks in the 90° oriented magnetization correspond with the peaks in the MR data at approximately t_{Cu} of 0.8, 2.0, and 2.8 nm. Only three peaks in the oscillating MR data are shown as the thickest superlattice grown had a Cu spacer thickness of $t_{\text{Cu}} = 3.5$ nm. Strong 90° coupling is still present at the first oscillation maximum even though the value of the MR is strongly suppressed.⁸

In order to illustrate the correlation between 90° coupling and MR in superlattices with rough interfaces, the two in-plane components of the magnetization extracted from longitudinal and "transverse"²¹ Kerr hysteresis loops are shown for selected films in Fig. 2 as a function of the normalized field. In all films examined, H_c was approximately 35 Oe. The longitudinal Kerr hysteresis loops detect the component of the in-plane magnetization along the easy axis, M_x , while the transverse Kerr hysteresis loops measure the component M_y , perpendicular to M_x .¹⁹ The normalized total (in-plane) magnetization, M_z , results from adding the two in-plane components together in quadrature. The MR data are shown in the far right column. The Cu spacer thickness is (a)–(d) 0.7 nm, (e)–(h) 0.8 nm, (i)–(l) 1.0 nm, and (m)–(p) 2.0 nm. Using the results in Fig. 1, the interlayer coupling in the first and third rows of Fig. 2 are seen to be ferromagnetic.

This conclusion is verified by the squareness of the hysteresis loops, ~~and the very small amount of magnetization M_y perpendicular to the easy axis during reorientation.~~ The resulting MR is small and comparable to the transverse MR results for pure Co films. The hysteresis loops in the second and fourth rows of Fig. 2 are shown for t_{Cu} at the first and second oscillation maxima. Typically, the coupling in these superlattices has been identified as antiferromagnetic.¹⁻⁸ In the case of rough interfaces, the stepped, compound easy-axis hysteresis loops resulting from antiferromagnetic coupling are not observed. Rather, the easy-axis hysteresis loops, M_x , are canted and rounded. However, during the switching process, the magnetization reorients itself along a direction 90° from the easy axis and the field direction as shown in Figs. 2(f) and 2(n). This is clear evidence that there is 90° domain formation in the superlattice, ~~which appears as 90° coupling.~~ The MR in Fig. 2(p) can be fit with the M_y magnetization curve, leaving a small residual (1%).

Should antialignment between domains with the layers or between the layers themselves be present, then the quadrature sum of the magnetization during the switching process should not be constant. The third column in Fig. 2 illustrates, within the accuracy of our Kerr measurements, that some regions of magnetization are misaligned in each case. The switching is not solely due to coherent rotation since little hard axis magnetization M_y is detected in the ferromagnetically coupled superlattices. In all cases studied here, there is no correlation between the percentage of misalignment, extracted from the magnitude of the dip in the M_x values, and the percentage of MR. ~~The field value at the position of the MR maxima [Fig. 2(p)] and the M_x minima [Fig. 2(o)] are the same [since M_y is also a maximum (Fig. 2(n))].~~ In all cases, the estimated change in M_x from saturation to H_c due to slope in the easy-axis hysteresis loops is less than 1%. Hence we conclude that the MR is correlated with 90° (with respect to the field and easy axes) orientation of domains or layers within the superlattice.

The switching behavior of the superlattice can be analyzed most simply as the coherent rotation of two exchange coupled layers with magnetocrystalline anisotropy, external magnetic field, and interlayer coupling energies. In order to incorporate roughness into this simple model, a parameter which describes the percentage of the films that are antiferromagnetically coupled is included. When the energy equations are expressed in dimensionless format, only two free parameters exist: the ratio of the ferromagnetic to antiferromagnetic interlayer coupling strength, and the percentage of the films that are antiferromagnetically coupled. No biquadratic exchange energy terms are necessary to have equilibrium magnetization orientation within domains in adjacent layers at right angles to each other during the switching process. When the percentage of antiferromagnetic coupling between the layers is about 20%, a value consistent with the data in the M_x curves of Fig. 2, ratios of the strengths of the ferromagnetic to antiferromagnetic coupling parameters need be in the range of 0.0–0.25 for 90° orientations to exist during switching. This is a reasonable range for this ratio.²² Although the computed magnetization curves, simulated from the simple model, differ from those actually measured,

domains

the trends suggest that 90° oriented domains are possible for reasonable values of the coupling parameters. Hence 90° coupling in these Co/Cu films results from favorably oriented (90°) domains resulting from incomplete antiferromagnetic coupling. The ferromagnetic component of the superlattices serve as the orientation (field) axis at zero field. In order to accurately model the data, domain formation within the layers must be included.^{17,23} ~~Accurate quantitative micro-magnetic structure determined by STEM electron holography^{23,24} can be used to address the issue of whether or not the domains are magnetically coupled throughout the entire superlattice.²⁵ Preliminary observations indicate the presence of 90° domain formation within the superlattice stack and the presence of domains within the layers themselves.²⁵~~

In conclusion, we have demonstrated the strong correlation between 90° and MR in Co/Cu superlattices, consistent with the predominance of the biquadratic energy terms expected in superlattices with rough interfaces. No apparent correlation between antiferromagnetic alignment (as extracted from total magnetization curves) and GMR was observed indicating that the GMR was due to 90° alignment of adjacent layers or domains.

We would like to acknowledge Gary Hembree, Kevin Heim, and Marian Mankos for technical assistance and thoughtful discussions. This work is supported by the Office of Naval Research under Grant No. N00014-93-1-0099.

- ¹M. N. Baibich, J. M. Broto, A. Fert, F. Nguyen Van Dau, F. Petroff, P. Etienne, G. Creuzet, A. Friederich, and J. Chazelas, *Phys. Rev. Lett.* 61 2472 (1988); S. S. P. Parkin, N. More, and K. P. Roche, *ibid.* 64, 2304 (1990); P. Grunberg, J. Barnas, F. Saurenbach, J. A. Fuss, A. Wolf, and M. Vohl, *J. Magn. Magn. Mater.* 93, 58 (1991); S. S. P. Parkin, *Phys. Rev. Lett.* 67, 3598 (1991).
- ²E. E. Fullerton, M. J. Conover, J. E. Mattson, C. H. Sowers, and S. D. Bader, *Phys. Rev. B* 48, 15 755 (1993); E. E. Fullerton, M. J. Conover, J. E. Mattson, C. H. Sowers, and S. D. Bader, *J. Appl. Phys.* 75, 6461 (1994); C. D. Potter, R. Schad, P. Belien, G. Berbanck, V. V. Moshchakov, Y. Bruynseraede, M. Schafer, R. Schafer, and P. Grunberg, *Phys. Rev. B* 49, 16 055 (1994).
- ³S. S. P. Parkin, R. Bhadra, K. P. Roche, *Phys. Rev. Lett.* 66, 2152 (1991).
- ⁴A. Fert, A. Barthelemy, P. Etienne, S. Lequien, R. Loloee, D. K. Lotis, D. H. Mosca, F. Petroff, W. P. Pratt, and P. A. Schroeder, *J. Magn. Magn. Mater.* 104–107, 1712 (1992); D. H. Mosca, F. Petroff, A. Fert, P. A. Schroeder, W. P. Pratt, Jr., and R. Loloee, *ibid.* 94, L1 (1991); Y. Chen, J. M. Florczak, and E. D. Dahlberg, *ibid.* 104–107, 1907 (1992).
- ⁵M. T. Johnson, P. J. H. Bloemen, R. Coehoorn, J. J. de Vries, N. W. E. McGee, R. Jungblut, A. Reinders, and J. aan de Stegge, *Mater. Res. Soc. Symp. Proc.* 313, 212 (1993); P. H. J. Bloemen, R. van Dalea, W. J. M. Jonge, M. T. Johnson, and J. aan Stegge, *J. Appl. Phys.* 73, 5972 (1993).
- ⁶P. M. Levy, K. Ounadjela, S. Zhang, Y. Wang, C. B. Sommers, and A. Fert, *J. Appl. Phys.* 67, 5914 (1990); J. Mathon, D. M. Edwards, R. B. Muniz, and M. S. Phan, *J. Magn. Magn. Mater.* 104–107, 1721 (1992); K. B. Hathaway, and J. R. Cullen, *ibid.* 104–107, 1840 (1992); P. Bruno and C. Chappert, *Phys. Rev. B* 46, 261 (1992); J. Mathon, M. Villeret, D. M. Edwards, and R. B. Muniz, *J. Magn. Magn. Mater.* 121, 2423 (1993).
- ⁷P. M. Levy, S. Zhang, and A. Fert, *Phys. Rev. Lett.* 65, 1643 (1990); S. Zhang, and P. M. Levy, *Phys. Rev. B* 47, 6776, (1993); P. M. Levy, H. E. Camblong, and S. Zhang, *J. Appl. Phys.* 75, 7076 (1994); J. L. Duvail, A. Fert, L. G. Pereira, and D. K. Lotis, *ibid.* 75, 7070 (1994).
- ⁸F. Giron, P. Boher, Ph. Houdy, F. Pierre, P. Beauvillain, C. Chappert, K. Le Dang, and P. Vieillet, *J. Magn. Magn. Mater.* 104–107, 1887 (1992); F. Giron, P. Boher, Ph. Houdy, P. Beauvillain, K. Le Dang, and P. Vieillet, *ibid.* 121, 318 (1993); P. P. Freitas, I. G. Trindade, L. V. Melo, J. L. Leal, N. Barradas, and J. C. Soares, *J. Appl. Phys.* 73, 5527 (1993).
- ⁹J. J. de Miguel, A. Cebollada, J. M. Gallego, R. Miranda, C. M. Schneider, P. Schuster, and J. Kirschner, *J. Magn. Magn. Mater.* 93, 1 (1991).

- ¹⁰ M. Rühig, R. Schäfer, A. Hubert, R. Mosier, J. A. Wolf, S. Demokritov, and P. Grünberg, *Phys. Status Solidi A* 125, 635 (1991).
- ¹¹ J. Unguris, R. J. Celotta, and D. T. Pierce, *J. Appl. Phys.* 75, 6437 (1994).
- ¹² M. E. Filipkowski, C. J. Gutierrez, J. J. Krebs, and G. A. Prinz, *J. Appl. Phys.* 73, 5963 (1993); Z. Celinski, B. Heinrich, and J. F. Cochran, *ibid.* 73, 5966 (1993).
- ¹³ J. C. Slonczewski, *Phys. Rev. Lett.* 67, 3172 (1991).
- ¹⁴ R. Ribas and B. Dieny, *J. Magn. Magn. Mater.* 121, 313 (1993).
- ¹⁵ M. E. Filipkowski, C. J. Gutierrez, J. J. Krebs, and G. A. Prinz, *J. Appl. Phys.* 73, 5963 (1993).
- ¹⁶ K. Brohl, S. DiNunzio, F. Schreiber, Th. Zeidler, and H. Zabel, *J. Appl. Phys.* 75, 6184 (1994).
- ¹⁷ Y. U. Idzerda, C.-T. Chen, S. F. Cheng, W. Vavra, G. A. Prinz, G. Meigs, H.-J. Lin, and G. H. Ho (unpublished).
- ¹⁸ J.-F. Bobo, B. Baylac, L. Hennes, O. Lenoble, M. Picuch, B. Raquet, and J.-C. Ousset, *J. Magn. Magn. Mater.* 121, 291 (1993); M. J. Pechan, J. F. Aukner, C. F. Majkrzak, D. M. Kelley, and I. K. Schuller, *J. Appl. Phys.* 75, 6178 (1994).

- ¹⁹ Z. J. Yang and M. R. Scheinfein, *J. Appl. Phys.* 74, 6810 (1993); Z. J. Yang, S. D. Healy, K. R. Heim, J. S. Drucker, G. G. Hembree, and M. R. Scheinfein *ibid.* 75, 5589 (1994).
- ²⁰ E. R. Moog, C. Lui, S. D. Bader, and J. Zak, *Phys. Rev. B* 39, 6949 (1989).
- ²¹ We use the notation transverse here to indicate that the field direction and easy axis are oriented in-plane and perpendicular to the polarization detection axis. We are not measuring the transverse Kerr effect which would require an additional rotation of 90° of the detection axis.
- ²² R. P. Erickson, *J. Appl. Phys.* 75, 6163 (1994); R. P. Erickson, K. B. Hathaway, and J. R. Cullen, *Phys. Rev. B* 47, 2626 (1993).
- ²³ M. Mankos, M. R. Scheinfein, and J. M. Cowley, *J. Appl. Phys.* 75, 7418 (1994); M. Mankos, M. R. Scheinfein, and J. M. Cowley, *Ultramicroscopy* (in press).
- ²⁴ M. Mankos, Z. J. Yang, M. R. Scheinfein, and J. M. Cowley, *IEEE Trans. Magn.* (in press).
- ²⁵ L. J. Heydemann, J. N. Chapman, and S. S. P. Parkin, *J. Phys. D* 27, 881 (1994).

52 small lines needed =

25 large lines

Lines removed

p1 - 70

p2 - 6

p3 - 15

31

Should just make it with

5 large lines to spare.

Absolute Magnetometry of Thin Cobalt Films and Co/Cu Multilayer Structures at Nanometer Spatial Resolution

Marian Mankos, Z.J. Yang, M. R. Scheinfein and J. M. Cowley

Department of Physics and Astronomy, Arizona State University, Tempe, AZ 85287-1504, U.S.A.

Abstract--The absolute measurement of magnetization in thin magnetic specimens at nanometer spatial resolution has been made possible by implementing two off-axis holography modes in a scanning transmission electron microscope (STEM). The absolute mode of STEM holography displays a linear change in phase difference for regions with constant magnetization and the slope determines the absolute value of magnetization in the specimen. The differential mode of STEM holography displays a constant value of phase difference for regions with constant magnetization, which simplifies the identification of magnetic structures in the specimen and the determination of domain wall profiles. Taking into account the high spatial resolution of a STEM instrument, STEM holography provides a valuable tool for quantitative investigations of magnetic structures at the nanometer level.

I. INTRODUCTION

Artificial magnetic structures and devices are attracting scientific interest due to their many unique properties which are often strongly influenced by their micromagnetic structure. Multilayer structures composed of magnetic layers separated by nonmagnetic spacers [1] exhibit characteristic properties like long range oscillatory coupling and giant magnetoresistance related to antiferromagnetic coupling [2], which depend critically on the composition and structure. Thin film stresses, alloy segregation, crystal defects and surface imperfections play an important role in these predominantly two-dimensional systems. At present many techniques for the observation of magnetic structure, including magneto-optical methods [3], magnetic force microscopy [4], the Bitter pattern method [5] and electron microscopy [6]-[8], are available. Electron microscopy is the only method to date capable of delivering micromagnetic and structural information at nanometer (point) spatial resolution. Electron microscopes equipped with high brightness and coherent field emission sources and efficient CCD detection systems and fast image processing techniques have accelerated the applications of electron holography [9], [10]. In this electron-optical technique, both the amplitude and phase of the transmitted electron waves are recorded whereas in conventional electron microscopy only the modulus of the transmitted wave is recorded. The relative phase shift, which can be retrieved from an electron hologram, contains absolutely calibrated information about the local distribution of scalar and vector potentials and can be used to explore the micromagnetic structure of thin magnetic specimens.

II. TECHNIQUE

In STEM holography [11], an electron wave emitted from the electron source is split by an electrostatic Moellenstedt biprism into two wave packets, which are transferred by the condenser lens and focused by the objective lens into two fine electron probes coherently illuminating the specimen. When the objective lens is operated at a large defocus, a relatively large area of the specimen is illuminated. The beam is held stationary (scanning switched off). The two wave packets interfere after passing through the specimen and form an interference pattern, a hologram, which is magnified subsequently by two postspecimen lenses and appears as a fringe-modulated double image in the detector plane. The recorded hologram is then reconstructed in the conventional way as in TEM holography: a fast Fourier transform of the hologram yields a diffractogram with two characteristic sidebands, whose separation depends inversely upon the spacing of the fringes. One sideband is isolated and its inverse Fourier transform reveals the amplitude and phase of the complex image wave, thus readily eliminating the conjugate image which obstructs the image in in-line holography. A detailed description of the theory, instrumentation and image processing has been published elsewhere [12], [13]. The contrast observed in the reconstructed holograms can be explained by analyzing the wave paths from the electron source through the specimen to the detector plane. If a specimen is present, the two split electron waves suffer additional phase shifts [12] due to the electromagnetic fields present. It can be shown that the additional phase shift caused by the specimen is [12]

$$\phi_1 - \phi_2 = \frac{1}{\hbar} \oint \mathbf{m} \cdot \mathbf{v} \cdot d\mathbf{l} - \frac{e}{\hbar} \iint \mathbf{B} \cdot d\mathbf{S}, \quad (1)$$

where \mathbf{v} is the velocity, \mathbf{B} the magnetic field and \mathbf{S} the oriented area enclosed by the two beam paths. From the first

term in eqn. (1), $\frac{1}{\hbar} \oint \mathbf{m} \cdot \mathbf{v} \cdot d\mathbf{l}$, the mean inner potential can be determined for a specimen of known geometry. The

second term of eqn. (1), $\frac{e}{\hbar} \iint \mathbf{B} \cdot d\mathbf{S}$, yields information

about the magnetization distribution in a magnetic specimen. In thin magnetic films of nearly constant thickness the first term contributes a constant value and the phase shift is dominated by the second term, the magnetic phase shift. The phase difference is then proportional to the magnetic flux enclosed by the two beam paths as they traverse the specimen. Two intrinsically different modes of STEM holography can be distinguished: an absolute mode and a

differential mode. In the absolute mode one of the wave passes through vacuum and the other through the specimen (Fig. 1a). Assuming a constant and zero phase in vacuum, we can absolutely calibrate the phase shift since the phase difference is always measured with respect to vacuum. The reconstructed phase difference represents the absolute phase shift caused by the specimen. In the case of a magnetic specimen the phase difference is evaluated from an area integral (as compared to a line integral for the mean inner potential evaluation) and therefore the phase difference, measured with respect to vacuum, represents the absolute phase shift caused by the enclosed area of the specimen. In a domain with uniform magnetization located near a hole in a film of constant thickness, the phase will change linearly with increasing distance from the edge as the enclosed flux increases, $\iint B \cdot dS \cong B_n x t$, where B_n is the averaged component of the magnetic field normal to the plane defined by the wavevectors of the two split waves, t is the constant thickness and x is the distance from the edge. The gradient of the phase will determine the magnitude of B_n in the domain. In the differential mode of STEM holography both of the split electron waves pass through the specimen. Here, the two virtual sources are separated by a very small distance when projected onto the sample, typically several tens of nm (Fig. 1b). The size of the illuminated area which contributes to the phase difference (through the magnetic flux), is approximately constant for any two points D' , D'' in the detector plane (illumination is almost parallel). The sensitivity to local changes in phase difference in the direction perpendicular to the fringes is limited in this mode by the separation of the two sources. Since the resolution limit in reconstructed holograms is about 2-3 times the cosine fringe spacing [10], a sufficient condition for maintaining the resolution is that the separation of the two dual images in the recorded hologram be less than approximately 3 fringes. If this condition is met, the reconstructed phase difference becomes a direct measure of the local magnetic structure. In this mode domains with constant magnetization in a constant thickness film are represented as regions of constant phase difference, in contrast to

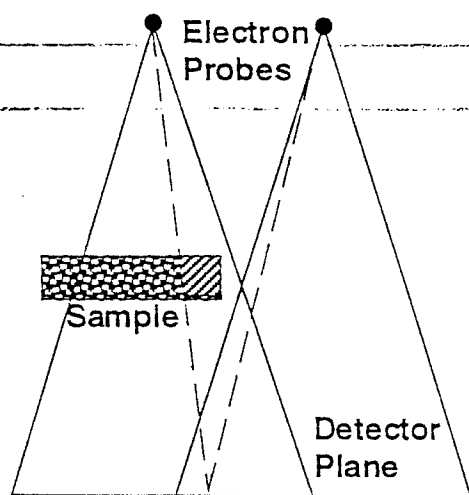


Figure 1.a. Absolute mode of STEM holography.

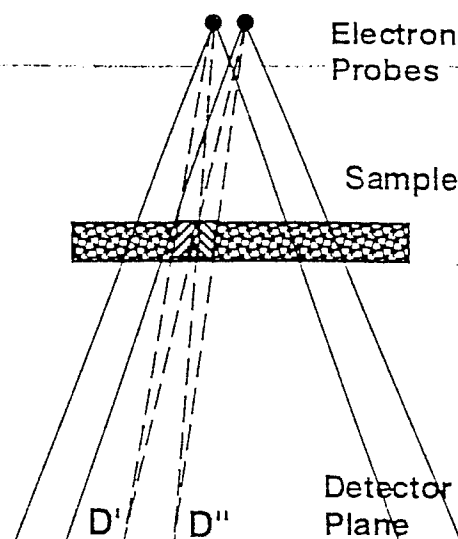


Figure 1.b. Differential mode of STEM holography.

the absolute mode, where the same domains would appear regions of linear phase difference.

III. EXPERIMENTAL RESULTS

We are interested in exploring the micromagnetic structure of giant magnetoresistance superlattice structures. It is well documented [1] that antiferromagnetic coupling between adjacent ferromagnetic layers in a superlattice composed of alternating ferromagnetic and nonmagnetic layers is present when giant magnetoresistance is observed. It is less clear whether the role of intralayer or interlayer electron scattering processes dominate the giant magnetoresistance effect. In this study, we wish to determine the orientation of domains in a superlattice, with an eye towards identifying whether or not domains penetrate through the ferromagnetic layers.

We have prepared several series of pure Co thin films and $[\text{Co}(t_{\text{Co}})/\text{Cu}(t_{\text{Cu}})]_n$ multilayers by evaporating on Corning cover glass substrates and holey carbon covered grids at room temperature in a dual e-beam UHV evaporation system. Deposition rates were 0.5–2 Å/s. The magnetoresistance was measured on patterned, dumbbell shaped samples using a four-probe method at room temperature with the field (up to 14 kOe) applied in the plane of film, and the current both transverse (TMR) and parallel (LMR) to the field. Magnetization curves were measured with the combined magneto-optical Kerr effect [14]. Both transverse Kerr effect and longitudinal Kerr effect hysteresis loops were measured along the easy axis and hard axis, respectively. Transverse Kerr effect hysteresis loops can be used to determine the symmetry of the in-plane anisotropy. Kinks in the longitudinal Kerr effect hysteresis loops indicated that some parallel alignment of adjacent Co layers was present in superlattices. For pure Co films, only anisotropy magnetoresistance (AMR) were observed in which MR minimum peaks appear at near the hysteresis loop zero field crossing.

To guarantee that accurate quantitative micromagnetic structure can be extracted using STEM holography, a preliminary quantitative study of pure Co films of vari-

thicknesses was done [12]. The magnitude of the saturation magnetization can typically be determined to better than 5% if the ferromagnetic film thickness is known. In Fig. 2a, an absolute hologram phase image is shown of a $\text{Co}(6\text{nm})/[\text{Cu}(3\text{nm})\text{Co}(1.5\text{nm})]_6/\text{Cu}(3\text{nm})$ superlattice. The thickness was calibrated with a quartz-crystal monitor, and the super-lattice periodicity was checked with low-angle x-ray scattering. A Fresnel image of the same part of the film is shown in Fig. 2b. Fresnel images show domain walls as either white or black lines. The regions between the walls are the domains.

We wish to identify whether or not the domains are ferromagnetically or antiferromagnetically coupled through the superlattice. We use the absolute calibration in the phase image in Fig. 2a where the contours indicate the direction of the in-plane component of the magnetization and the maximum phase gradient gives the thickness averaged magnetization. Assuming bulk magnetization of Co (18.17 kOe), the calculated maximum phase gradient for uniformly magnetized domains penetrating the bulk should be 0.0414 rad/nm . We number the domains starting at the edge of the hole and proceeding clockwise, 1 through 5 respectively. The maximum phase gradient of domains 1, 2, 3 and 5 are $0.041 \pm 0.0006 \text{ rad/nm}$ indicating that the domains penetrate the sandwich and are uniformly (ferromagnetically) aligned. The phase gradient in domain 4 is 0.0367 rad/nm . This value is 10% less than the uniformly magnetized value. If a single layer were antiferromagnetically aligned within this domain, the phase gradient would have to be 20% lower. Therefore, the magnetization in one of the layers (10% of the active thickness) is rotated 90° with respect to the magnetization in the other layers. When the components are added in quadrature weighted by the active Co layer thickness, the integrated magnetization is 10% lower than the aligned value.

In conclusion, with STEM based electron holography, we are able to determine the orientation of domains in a superlattice. It seems as though our goal of correlating giant magnetoresistance measurements with micromagnetic analysis in order to isolate the role of interlayer and intralayer scattering in these structures is feasible.

IV. ACKNOWLEDGMENT

This work was supported by the NSF under grant DMR-9110386, and the ONR under grant N00014-93-1-0099. The microscopy was performed in the Center for High-Resolution Electron Microscopy at Arizona State U. supported by the NSF grant DMR93-14326. We are grateful to M. R. McCartney, P. Perkes and J.K. Weiss (Emispec Systems) for help with the hologram reconstruction and image processing.

V. REFERENCES

- [1] M.N. Baibich et al., *Phys. Rev. Lett.* vol. 61, p. 2472 (1988).
- [2] S.D. Bader, *J. Magn. Magn. Mater.* vol. 100, p. 440 (1991).
- [3] M.J. Freiser, *IEEE Trans. Mag.* vol. 4, p. 152 (1968).
- [4] R. Allenspach, H. Salemink, A. Bischof and E. Weibel, *Z. Phys.* vol. B67, p. 125 (1987).
- [5] F. Bitter, *Phys. Rev.* vol. 38, p. 1903 (1931).
- [6] M.E. Hale, H.W. Fuller and H. Rubinstein, *J. Appl. Phys.* vol. 30, p. 789 (1959).
- [7] M.R. Scheinfein, J. Unguris, M.H. Kelley, D.T. Pierce, R.J. Celotta, *Rev. Sci. Instr.* vol. 61, p. 2501 (1990).
- [8] J.N. Chapman, *J. Phys D: Appl. Phys.* vol. 179, p. 629 (1984).
- [9] D. Gabor, *Nature* vol. 161, p.777 (1948).
- [10] A. Tonomura, *Electron Holography*, Springer Verlag Berlin Heidelberg 1993.
- [11] J.M. Cowley, *Ultramicroscopy* vol. 41, p. 335 (1992).
- [12] M. Mankos, M. R. Scheinfein and J. M. Cowley, *J. Appl. Phys.* vol. 75, p. 7418 (1993).
- [13] M. Mankos, A. A. Higgs, M. R. Scheinfein and J. M. Cowley, "Far-out-of-focus electron holography in a dedicated FEG STEM", *Ultramicroscopy*, unpublished.
- [14] Z.J. Yang and M.R. Scheinfein, *J. Appl. Phys.* vol. 74, p. 6810 (1994).



Fig. 2a. Phase image of Co/Cu multilayer acquired in absolute mode of STEM holography ($1.4\mu\text{m} \times 1.4\mu\text{m}$).

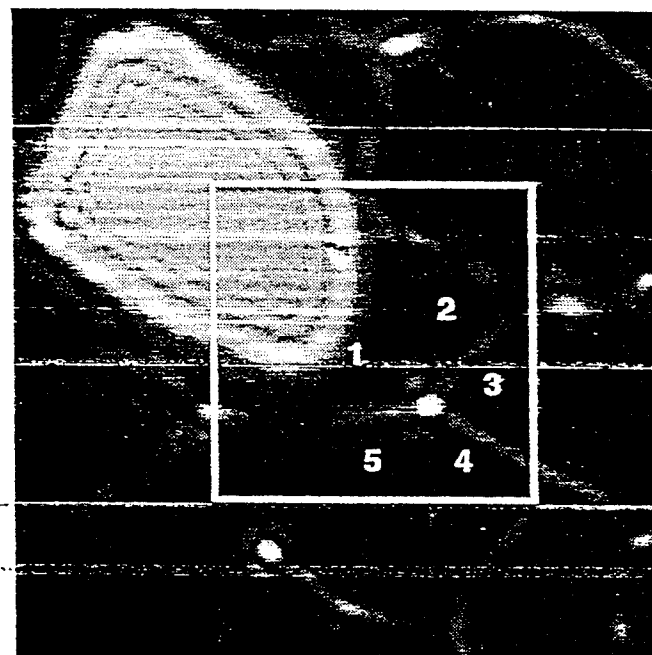


Fig. 2b. Fresnel image ($2.8\mu\text{m} \times 2.8\mu\text{m}$) of the same part of the film shown in a) with the marked region reconstructed in Fig. 2a.

Far-out-of-focus Electron Holography
in a dedicated FEG STEM

Marian Mankos, A. A. Higgs, M. R. Scheinfein and J. M. Cowley

Department of Physics and Astronomy, Arizona State University

Tempe, AZ 85287-1504, USA

Abstract:

Flexible operation of off-axis holography modes is achieved when a biprism is placed in the illumination system of a scanning transmission electron microscope, equipped with a field emission electron source. The separation of the two virtual sources created by the biprism can be varied by changing the voltage applied to the biprism or by simply changing the excitation of the condensor and/or objective lenses. Two distinct modes of holography are used to study the magnetic microstructure in thin magnetic films. In the absolute mode the phase difference changes linearly in regions of constant magnetization and thickness and the slope determines the magnitude of magnetization. In addition, this mode permits the determination of the mean inner potential of a solid of known geometry. In the differential mode the phase difference is constant in regions of constant magnetization, allowing a simple and straightforward determination of domain wall profiles. The contrast obtained in the holography modes is compared to well-known contrast in the Fresnel and Differential Phase Contrast modes of Lorentz microscopy. The combination of several Scanning Transmission Electron Microscopy based techniques presents a powerful tool for the investigation of magnetic microstructure.

1. Introduction.

Recent developments in information storage technology based on new sample preparation techniques, such as Molecular Beam Epitaxy (MBE), Metal-Organic Chemical Vapor Deposition (MOCVD), Electron Beam Lithography (EBL) and sputtering, permit the production of artificial structures with extraordinary accuracy. When the composition and geometry of these artificial structures is tightly controlled, devices designed for specific applications such as magnetic recording media, magnetic recording head cores and magnetic sensors can be fabricated. Properties such as coercivity, micromagnetic features, local magnetic moment and anisotropy can be manipulated at the nanometer level [1]. Layered structures, composed of alternating magnetic and non-magnetic thin films and monolayer thickness epitaxial films of magnetic elements on crystalline metallic, semiconductor and insulator substrates, have been produced. Characteristic properties of multilayer structures, like long range oscillatory coupling [2] and giant magnetoresistance related to antiferromagnetic coupling [3], depend critically on composition and structure, which in turn depend on the growth conditions. Similarly, the growth process of epitaxial films strongly influences the magnetic properties of interest : the easy axis of orientation of magnetization in a material can change from in-plane to perpendicular with subtle changes in structure and vary the shape of the hysteresis loop [4]. Crystal defects, thin film stresses, alloy segregation and surface imperfections play an important role in these predominantly two-dimensional systems. High spatial resolution magnetic contrast imaging techniques are required to solve the structure-properties relationships in these materials.

The HB-5 scanning transmission electron microscope (STEM) at Arizona State University, equipped with a field emission source, has been significantly modified to allow complex investigations of novel magnetic materials. A highly efficient detector system [5]

has been installed, allowing the operation of Fresnel and Differential Phase Contrast modes of Lorentz microscopy at the 1nm level [6, 7]. In addition, the far-out-of-focus scheme of STEM holography [8] has become available with the installation of an electron biprism. Qualitative and more importantly, quantitative information can be extracted from a hologram, thus allowing the absolute measurement of magnetization in a material at nm spatial (point) resolution. The mean inner potential, carrying information about the inner structure and composition of a solid, can be measured with high accuracy from off-axis holograms.

2. Principles of Operation.

2.1. Instrumentation.

The electron-optical scheme of the HB-5 STEM adapted for off-axis holography is shown in Fig.1. An electrostatic Möllenstedt biprism [9] is placed in the STEM illuminating system between the gun and condenser lens. The biprism is a glass rod, sputter-coated with a thin layer of platinum for electrical conductivity, approximately 0.5 μm in diameter and secured across a 3mm hole in a specially built aperture holder. The biprism is held at constant potential between 0V to 180V, supplied in our case by a continuously variable series of batteries. The aperture rod holding the biprism assembly is adjustable in the x and y directions (perpendicular to the optical axis) and is secured with a series of tension springs.

The electron wave emitted from the source is split by the biprism into two wave packets, which are transferred by the condenser lens and focussed by the objective lens into two fine electron probes coherently illuminating the specimen. Magnetic specimens must be located out of the objective lens in order to minimize the effect of the magnetic field of the objective lens. A finite-element calculation shows that the residual magnetic field of the

objective lens (operated at 12mm focal length) at the specimen position is approximately 50 gauss, which is sufficiently small for most applications. When the objective lens is operated at large defocus, a relatively large area of the specimen is illuminated. The beam is held stationary (scanning switched off). The two wave packets interfere after passing through the specimen and form an interference pattern, a hologram, which is subsequently magnified by two post-specimen lenses and appears as a fringe-modulated double image in the detector plane. The hologram is transferred from the YAG detector by a system of optical mirrors out of the vacuum chamber and recorded on a slow-scan CCD camera. The large dynamic range and high sensitivity of the CCD camera combined with the direct 14-bit digital image output significantly improve the recording process as compared to a low-light-level TV camera.

The fringe spacing and the separation of the twin images in the hologram are determined by the electrostatic voltage applied to the biprism and by the excitations of the condenser and objective lenses. This combination permits expanded flexibility of our system when compared to the classical TEM holography scheme. The maximum number of fringes per image is limited by the CCD array of 512 x 512 pixels : a minimum sampling of 4 pixels for one fringe spacing permits a maximum number of approximately 130 recordable fringes. The objective lens excitation determines the magnification (with both post-specimen lenses fully excited) of the shadow image : the smaller the defocus, the larger the magnification. With a weakly excited condenser lens, a minimum image separation of about 3-4 fringe spacings can be achieved at optimum recording conditions (optimum biprism voltage). For a strongly excited condensor lens, the maximum image separation is more than 150 fringe spacings. A typical set of calibration curves is shown in Fig.2. The separation of the images plays an important role in the explanation of the contrast observed in the holography modes which is described in sections 2.3 and 2.4. The biprism voltage is usually varied from 10V to 25V. For these small voltages only a

few fringes appear whereas, for higher voltages the fringes become too fine to sample with our finite resolution CCD array.

The recorded hologram is then reconstructed in the conventional way as for TEM holography [10]. A Fast Fourier Transform of the hologram yields a diffractogram with two characteristic sidebands, with a separation that depends inversely upon the spacing of the fringes. One sideband is isolated and its Inverse Fourier Transform reveals the amplitude and phase of the complex image wave, thus eliminating the conjugate image which obscures the image in in-line holography. In this paper we reconstruct only the phase image. The phase retrieval process yields only the principal values in the interval $[-\pi, +\pi]$. For strong phase objects, such as thin magnetic films, phase differences of tens of radians are common. The phase images reveal this periodicity in the form of characteristic 'wrapped' images. The wrapped images must be further processed in order to unwrap the actual phase by successive additions or subtractions of 2π rad. The reconstruction process is illustrated step by step in Fig.3.

2.2. Theory.

The contrast observed in the reconstructed holograms can be understood by tracing wave paths from the electron source through the specimen to the detector plane. An electron wave from the source is split by the biprism into two wave packets. The effect of the biprism can be represented by the formation of two coherent virtual sources Q' and Q'' , as shown in Fig.1. In the detector plane, the two wave packets interfere, and within the region of overlap the intensity distribution becomes a modulated pattern of cosine fringes

$$I_d(\mathbf{r}) = |a_A(\mathbf{r}) \exp(2\pi i \mathbf{k}_A \mathbf{r}) + a_B(\mathbf{r}) \exp(2\pi i \mathbf{k}_B \mathbf{r})|^2 =$$

$$= |a_A(\mathbf{r})|^2 + |a_B(\mathbf{r})|^2 + 2|a_A(\mathbf{r})||a_B(\mathbf{r})| \cos[2\pi(\mathbf{k}_A - \mathbf{k}_B) \cdot \mathbf{r} + (\varphi_1 - \varphi_2)], \quad (1)$$

where \mathbf{k}_A and \mathbf{k}_B are the wave vectors of the two interfering waves and $a_A(\mathbf{r})$, $a_B(\mathbf{r})$ are the corresponding amplitudes. Specific properties of the specimen are contained in the amplitude modulation and the phase difference of the two waves. With no specimen present the phase shift $\varphi_1 - \varphi_2 = 0$ and the interference results in a set of up to several hundred parallel fringes covering the detector plane. If a specimen is present, the two waves suffer additional phase shifts due to the electromagnetic fields present [11]. Consider the phase difference between paths QAD and QBD, schematically shown in Fig.4:

$$\begin{aligned} \varphi_1 - \varphi_2 &= 2\pi \oint_{QADBQ} \mathbf{k} d\mathbf{l} = \frac{2\pi}{h} \oint \mathbf{p} d\mathbf{l} = \frac{1}{h} \oint (\mathbf{mv} - e\mathbf{A}) d\mathbf{l} \\ &= \frac{1}{h} \oint \mathbf{mv} d\mathbf{l} - \frac{e}{h} \iint \nabla \times \mathbf{A} d\mathbf{S} = \frac{1}{h} \oint \mathbf{mv} d\mathbf{l} - \frac{e}{h} \iint \mathbf{B} d\mathbf{S}, \end{aligned} \quad (2)$$

where $\mathbf{p} = \hbar \mathbf{k}$ is the canonical momentum, \mathbf{A} is the vector potential, \mathbf{B} the magnetic field and \mathbf{S} the oriented area enclosed by the path QADBQ. From the first term in equation (2), $\frac{1}{h} \oint \mathbf{mv} d\mathbf{l}$, the mean inner potential can be determined for a specimen of known geometry. The second term of equation (2), $\frac{e}{h} \iint \mathbf{B} d\mathbf{S}$, yields information about the magnetization distribution in a magnetic specimen. In thin magnetic films of nearly constant thickness the first term contributes a constant value and the phase shift is dominated by the second term, the magnetic phase shift. The phase difference is then proportional to the magnetic flux enclosed by the two beam paths as they traverse the specimen. The enclosed area depends upon the separation of the two virtual point sources which in turn depends upon the biprism voltage and the excitation of the condensor and objective lenses.

Two intrinsically different modes of STEM holography can be distinguished, an absolute mode and a differential mode. In the absolute mode, one wave packet passes through vacuum and the other passes through the specimen as shown in Fig.5a. This mode has a direct analogy with TEM electron holography. In the differential mode, both waves traverse the specimen as shown in Fig.5b and interfere in the detector plane. In the differential mode, no hole in the specimen is required, unlike the absolute (and TEM holography) mode.

2.3. Absolute mode.

In the absolute mode, assuming a constant and zero phase in vacuum, we can absolutely calibrate the phase shift since the phase difference is always measured with respect to vacuum. With no specimen present, the phase difference in vacuum varies at maximum ± 0.3 rad across the region used for phase reconstruction. The reconstructed phase difference represents the absolute phase shift caused by the specimen. One of the two terms contributing to the phase shift in equation (2) can be eliminated by judicious choice of the specimen and its geometry. An accurate measurement of the mean inner potential of a nonmagnetic specimen, with the second term of equation (2) vanishing, requires a sharp, well-defined wedge with a preferably linear change of thickness (with increasing distance from the edge) [13]. Accurate measurements of the mean inner potential are important for low-energy electron diffraction, reflection high energy electron diffraction and Fresnel imaging of surfaces, because it determines the sample's electron-optical refractive index. A quantitative determination of the mean inner potential can be useful for the mapping of heterostructures and buried space charge layers in artificial structures. For a magnetic specimen, constant film thickness is advantageous, since the

constant contribution of the mean inner potential can be eliminated by taking a gradient of the phase shift.

Although the focus of this paper is not on the mean inner potential determination, we measured the mean inner potential of magnesium oxide (MgO) in order to compare our STEM results with the accurate measurements made using TEM based electron holography [13]. Magnesium oxide smoke crystals form nearly perfect cubes making MgO a suitable material for the determination of the mean inner potential. When oriented nearly along the [110] orientation (misalignment is necessary to reduce dynamical scattering effects), the electron wave travels through a 90° wedge, where the projected thickness t equals approximately twice the distance from the edge. For monoenergetic electrons the phase difference is proportional to the mean inner potential U_i and projected thickness as [12]

$$\varphi_1 - \varphi_2 = \frac{2\pi}{\lambda} \left(\frac{E_0 + E}{2E_0 + E} \right) \frac{eU_i}{E} t, \quad (3)$$

where λ is the electron wavelength, E_0 is the rest energy ($=0.511\text{MeV}$) and E is the electron's kinetic energy (in our case $E = 100\text{ keV}$). Fig.6 illustrates how the mean inner potential is determined from holograms extracted from a MgO crystal near the [110] orientation. The recorded hologram is shown in Fig.6a and the wrapped phase image is shown in Fig.6b. For comparison, an image of the same MgO crystal acquired in STEM bright field mode is shown in Fig.6.c. A 105 nm x 35 nm section of the phase image is unwrapped in Fig.6d, where the slope of the line-scan perpendicular to the edge gives a phase gradient of $0.1168 \pm 0.003\text{ rad/nm}$. The mean inner potential extracted from this line-scan is $U_i = 12.7 \pm 0.3\text{V}$. This value agrees quite well with the accepted value of $U_i = 13.01 \pm 0.6\%$ [13]. This experiment is carried out with the specimen in the out-of-lens position, where the error margin stems from the inaccuracy in orientation and variation in the vacuum phase.

In the case of a magnetic specimen the phase difference is evaluated from an area integral (as compared to a line integral for the mean inner potential evaluation) and therefore the phase difference, measured with respect to vacuum, represents the absolute phase shift caused by the enclosed area of the specimen. In a domain with uniform magnetization located at a sharply defined edge, the phase changes linearly with increasing distance from the edge as the enclosed flux increases, $\iint \mathbf{B} d\mathbf{S} \cong B_n x t$, where B_n is the magnetization component normal to the plane defined by \mathbf{k}_A and \mathbf{k}_B , t is the constant thickness and x is the distance from the edge. The gradient of the phase difference will determine the magnitude and direction of the magnetization in the domain (to within an overall sign). For a film of constant thickness, we neglect thickness variations due to the inner potential since the phase difference due to the mean inner potential adds a constant to the phase and the quantitative magnetic information is derived from the gradient of the phase. Any phase changes caused by the inner potential due to thickness variations are small (~ 0.2 rad/nm for cobalt [13]) when compared to the absolute phase changes caused by the magnetic field ($\sim 10\pi$ rad). Fig.7 illustrates the absolute mode for an approximately 20nm thick Co film, e-beam sputtered on a holey carbon film. The slope of the phase difference determines, in this case quantitatively, the magnetization in the specimen. A more detailed analysis of the magnetic contrast including a comparison with Fresnel and Differential Phase contrast modes of Lorentz microscopy is given in [14].

2.4. Differential mode.

In the differential mode of STEM holography, both electron waves pass through the specimen. Here, the two virtual sources are separated by a very small distance when projected onto the sample, typically several tens of nm (Fig.5b). The size of the

illuminated area which contributes to the phase difference (through the magnetic flux), is approximately constant for any two points D' , D'' in the detector plane (illumination is almost parallel). The sensitivity to local changes in phase difference in the direction perpendicular to the fringes is limited in this mode by the separation of the two sources. Since the resolution limit in reconstructed holograms is about 2-3 times the cosine fringe spacing [10], a sufficient condition for maintaining resolution is that the separation of the two dual images in the recorded hologram should be less than approximately 3 fringes. If this condition is met, the reconstructed phase difference becomes a direct measure of the local magnetic structure. This limitation can be avoided for simpler magnetic structures (for example, a domain wall between two areas of constant magnetization) oriented properly with respect to the fringe direction (i.e. domain wall perpendicular to fringes), since the magnetization is constant along the wall. In this mode, domains with constant magnetization are represented as regions of constant phase difference, in contrast to the absolute mode, where the same domains would appear as regions of linear phase difference. For comparison, the same area of a thin Co film is imaged in the absolute and differential modes of STEM holography (Fig.8a,b) and well known Fresnel and Differential Phase Contrast modes of Lorentz microscopy (Fig.8c,d). This mode is advantageous for the investigation of domain wall profiles (compare [14]) and allows direct interpretation of magnetic microstructure.

3. Conclusions.

The far-out-of-focus scheme of STEM holography has been established experimentally, revealing qualitative and, more importantly, quantitative information about the structure and distribution of electromagnetic fields in the specimen at nanometer spatial

resolution. The absolute mode of STEM holography displays a linear change in phase difference in magnetic specimens for regions with constant magnetization and thickness, and in wedge-shaped crystalline specimens used for mean inner potential determination. The slope of the phase difference determines either the absolute value of magnetization in the first case or the mean inner potential in the second. The differential mode of STEM holography displays a constant value of phase difference for regions with constant magnetization, which simplifies the identification of micromagnetic structures such as domain walls and flux vortices in the specimen. In addition, no edge or hole is necessary since neither wave packet needs to pass through vacuum. In combination with other STEM-based techniques (Fresnel and Differential Phase Contrast modes of Lorentz microscopy), the new STEM holography modes provide a valuable tool for quantitative studies of magnetic microstructure at the nanometer level.

4. Acknowledgments.

This work was supported by the NSF under grant DMR-9110386, and the Office of Naval research under grant #N00014-93-1-0099. The electron microscopy was performed in the Center for High-Resolution Electron Microscopy at Arizona State University supported by the NSF grant DMR91-15680. We are grateful to M. R. McCartney and P. Perkes for help with the hologram reconstruction and image processing and Dr. J.K. Weiss of Emispec Systems for creative data acquisition software.

5. References.

- [1] L.M. Falicov et al., *J.Mater.Res.* **5** (1990) 1299.
- [2] S.S.P. Parkin, R. Bhadra and K.P. Roche, *Phys. Rev. Lett.* **66** (1991) 2152.
- [3] M.N. Baibich, J.M. Broto, A. Fert, F. Nguyen Van Dau, F. Petroff, P. Etienne, G. Creuzet, A. Friederich and J. Chazelas, *Phys. Rev. Lett.* **61** (1988) 2472.
- [4] S.D. Bader, *J. Magn. Magn. Mater.* **100** (1991) 440.
- [5] M. Mankos, S. Wang, J.K. Weiss and J.M. Cowley, *Proc. 50th Annual Meeting of the Microscopy Society of America*, Eds. G. W. Bailey, J. Bentley and J. A. Small (San Francisco Press, San Francisco, CA, 1992) 102.
- [6] M. Mankos, J.M. Cowley, R.V. Chamberlin, M.R. Scheinfein and J.D. Ayers, *Proc. 51st Annual Meeting of the Microscopy Society of America*, Eds. G. W. Bailey and C. L. Rieder (San Francisco Press, San Francisco, CA, 1993) 1026.
- [7] S. Kraut and J.M. Cowley, *Microscopy Research and Technique* **25** (1993) 341.
- [8] J.M. Cowley, *Ultramicroscopy* **41** (1992) 335.
- [9] G. Möllenstedt and H. Düker, *Z. Phys.* **145** (1956) 377.

- [10] H. Lichte, in *Advances in Optical and Electron Microscopy*, **12** (1991) 25.
- [11] Y. Aharonov and D. Bohm, *Phys. Rev.* **115** (1959) 485.
- [12] L. Reimer, in *Transmission Electron Microscopy*, Springer Verlag, Springer Series in Optical Sciences, **36** (1984).
- [13] M. Gajdardziska-Josifovska, M.R. McCartney, W.J. de Ruijter, D. J. Smith, J.K. Weiss and J.M. Zuo, *Ultramicroscopy* **50** (1993) 285.
- [14] M. Mankos, M.R. Scheinfein and J.M. Cowley, *J. Appl. Phys.* **75** (1994) 7418.

Figure Captions.

- Figure 1 : Electron-optical scheme of the HB-5 scanning transmission microscope adapted for holography.
- Figure 2 : Fringe calibration curves for varying biprism voltage and different objective lens defoci (underfocus positive).
a - available range of fringe spacings in nm,
b - available range of twin-image separations in fringe spacing units.
- Figure 3 : The hologram reconstruction process.
a - recorded hologram (field of view approximately $2.5\mu\text{m}$),
b - Fourier transform of a),
c - wrapped phase image,
d - partially unwrapped phase image,
e - three-dimensional view of unwrapped section marked in c).
- Figure 4 : Schematic diagram for phase difference path integral evaluation.
- Figure 5 : Schematic diagrams of STEM holography modes with insets of the cross-section view demonstrating the enclosed area.
a - absolute mode,
b - differential mode.
- Figure 6 : Extraction of mean inner potential from a STEM hologram (absolute mode).
a - recorded hologram of a MgO smoke crystal, oriented approximately

along the $[110]$ direction,

b - wrapped phase image,

c - regular scanned STEM image from the same MgO crystal,

d - unwrapped $105\text{nm} \times 35\text{ nm}$ section marked in b). The fine detail in the image stems from small Fe islands ($\sim 2\text{nm}$ in diameter) sputtered on the MgO surface.

Figure 7 : Determination of magnetization in $\sim 20\text{nm}$ Co film using the absolute mode of STEM holography.

a - wrapped phase image,

b - partially unwrapped phase image,

c - three-dimensional view of the section marked in b); the gradient of the phase difference taken perpendicular to the edge determines the absolute value of magnetization.

Figure 8 : Comparison of STEM holography and Lorentz microscopy modes acquired from a thin Co film.

a - differential mode of STEM holography displaying a constant value of phase difference inside a magnetic domain,

b - absolute mode of STEM holography displaying linear change of phase difference inside the same magnetic domain,

c - differential phase contrast mode of Lorentz microscopy; areas of different orientation in magnetization show different levels of brightness,

d - Fresnel mode of Lorentz microscopy reveals walls as dark and bright bands.

Note the arrows localizing the same domain wall in each case a)-d).

STEM Holography of Magnetic Materials

Marian Mankos^a, P. de Haan^b, V. Kambersky^c, G. Matteucci^d, M. R. McCartney^e, Z. Yang^a,
M. R. Scheinfein^a and J. M. Cowley^a

^aDepartment of Physics and Astronomy, Arizona State University, Box 871504, Tempe, AZ 85287-1504, U.S.A.

^bMESA Research Institute, University of Twente, P.O. Box 217, 7500 AE Enschede, The Netherlands

^cInstitute of Physics, Academy of Science, Cukrovarnicka 10, Praha 6, Czech Republic

^dDepartment of Physics, University of Bologna, via Imerio 46, 40126 Bologna, Italy

^eCenter for Solid State Science, Arizona State University, Tempe, AZ 85287-1704, U.S.A.

1. ABSTRACT

We have been using electron holography in a HB 5 scanning transmission electron microscope (STEM) to perform quantitative investigations of magnetic microstructure in thin magnetic specimens. Holograms are acquired with the scanning switched off. The objective lens is operated at large defocus, such that a relatively large area of the specimen is illuminated. Our system allows for flexible operation of off-axis holography modes, Fresnel and Differential Phase Contrast (DPC) modes of Lorentz microscopy. This combination of micromagnetic analysis techniques in one instrument provides a valuable tool for the investigation of magnetic microstructure at 1 nm spatial resolution. STEM holography accompanied by conventional Lorentz microscopy techniques has been used to characterize thin magnetic films, magnetic multilayer structures and small magnetic particles.

2. INTRODUCTION

Recent developments in magnetic information storage technology including magnetic recording media, magnetic recording heads and magnetic sensors can be characterized by the trend to control the geometry, chemical composition and magnetic microstructure at the near-atomic level. New sample preparation techniques, such as Molecular Beam Epitaxy (MBE) and Electron Beam Lithography (EBL), permit the fabrication of magnetic devices with properties such as coercivity, micromagnetic features, local magnetic moment and anisotropy controlled at the nanometer level [1]. For example, multilayered structures, composed of alternating magnetic and non-magnetic thin films of monolayer thickness, exhibit long range oscillatory coupling [2] and giant magnetoresistance related to antiferromagnetic coupling [3], which depend critically on composition and structure. Similarly, magnetic properties of epitaxial films of magnetic elements grown on crystalline metallic, semiconducting and insulating substrates strongly depend on the microstructure: the easy axis of orientation of magnetization in a

material can change from in-plane to perpendicular with subtle changes in structure and vary the shape of the hysteresis loop [4]. Surface steps, defects, thin film stresses and alloy segregation influence the magnetic microstructure of these predominantly two-dimensional systems. Magnetic properties of small particles, which are used in magnetic recording technology, are strongly dependent on the size, morphology and magnetic microstructure. The need for a high spatial resolution technique, capable of determining qualitative and *quantitative* micromagnetic structure has become eminent. High spatial resolution magnetic contrast imaging techniques, available in the STEM, provide a valuable tool for exploring the structure-properties relationships in these materials.

3. TECHNIQUE

A detailed description of the holography instrumentation and theory is given elsewhere [5,6]; here we present a brief review only. In the STEM implementation of electron holography, we split the partially coherent electron source into two virtual electron sources through the use of an Möllenstedt electron biprism [7]. The two electron wave packets are transferred by the condenser lens and focused by the objective lens into two fine electron probes coherently illuminating the specimen. The separation of the two virtual sources can be varied by changing the voltage applied to the biprism or by simply changing the excitation of the condenser and/or objective lenses. This system has expanded flexibility when compared to standard TEM based holography methods. With the beam held stationary and the objective lens operated at a relatively large defocus, a shadow image of a relatively large area can be observed. The two wave packets interact with the specimen and form an interference pattern (hologram), which appears as a fringe modulated (twin-)image in the detector plane. From the hologram, recorded on a slow-scan CCD camera, the amplitude and relative phase of the two electron waves can be extracted using methods standard in TEM off-axis holography. A fast Fourier transform yields a diffractogram with two characteristic sidebands, whose separation depends upon the fringe spacing. One of the sidebands is isolated and its inverse Fourier transform reveals the amplitude and phase.

The amplitude image contains information about the thickness and bulk inelastic mean-free-path of electrons in the solid [8]. The relative phase difference $\Delta\phi$, due to electromagnetic potentials present in the specimen region, can be expressed as [9]

$$\Delta\phi = \frac{1}{\hbar} \oint mvd\mathbf{l} - \frac{e}{\hbar} \iint \mathbf{B} d\mathbf{S}, \quad (1)$$

where \mathbf{v} is the electron's velocity, \mathbf{B} the magnetic induction and \mathbf{S} the oriented area enclosed by the two electron paths. From the first term in equation (1), the mean inner potential can be determined for a specimen of known geometry. The second term of equation (1), involves an area integral that contains information about the magnetization distribution in a magnetic specimen. In thin magnetic films of constant thickness, the first term contributes a constant phase shift, while a magnetic phase shift results from the second term. The phase difference $\Delta\phi$ is then proportional to the magnetic flux enclosed by the two beam paths as they traverse the specimen. In a magnetic specimen of varying thickness, such as a small particle, the electrostatic contribution, which cannot be neglected, can be eliminated from the phase image with the help of the amplitude image since both terms of the phase difference in equation (1) are linearly dependent on the projected thickness. Therefore the magnetic phase image can be retrieved by dividing the phase image by the thickness distribution (determined from the amplitude image).

We have developed two distinct holography modes : the absolute and differential [5]. In the absolute mode (Fig. 1a), one of the two electron probes travels through vacuum, while the

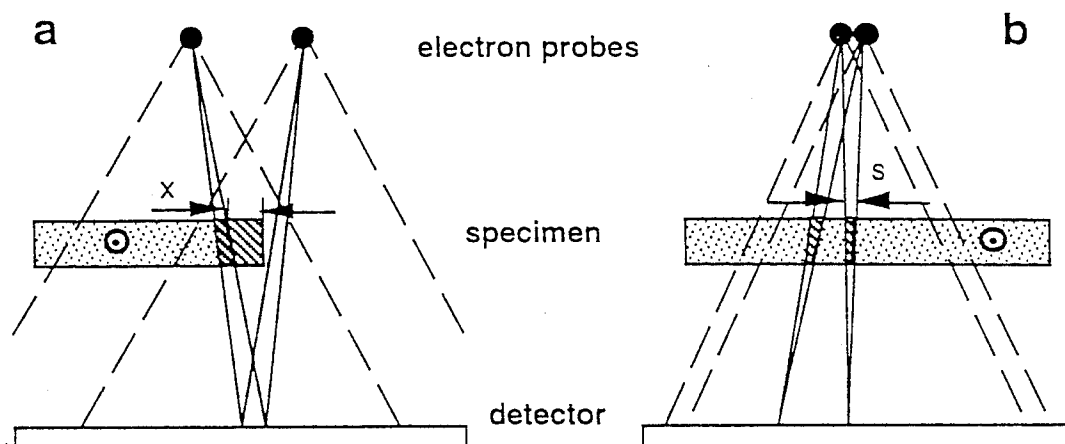


Figure 1. Absolute (a) and differential mode (b) of STEM holography.

other passes through the specimen. Assuming zero phase in vacuum we can absolutely determine the phase shift caused by the electromagnetic fields present in the specimen. For a magnetic specimen the phase shift $\Delta\phi$ is proportional to the magnetic flux enclosed by the two beam paths. In a uniformly magnetized domain located near the edge of a specimen of constant thickness, the phase difference $\Delta\phi$ changes linearly with increasing distance from the edge and $\Delta\phi \propto \iint \mathbf{B} d\mathbf{S} \equiv B_n x t$, where B_n is the component of the magnetic field normal to the plane determined by the wave vectors of the two split electron waves, x is the distance from the edge and t is the (constant) thickness. The gradient of the phase determines the magnitude of B_n (averaged over the film thickness) in the domain. For a film of nearly constant thickness we can neglect the contribution of the constant phase of the electrostatic field present in the specimen, since quantitative information is derived from the gradient of the phase difference and the phase variation due to the electrostatic potential is small (approximately 0.1 rad/nm of film thickness). This straightforward interpretation of the phase image can only be done for magnetic fields which are confined to the plane of the magnetic specimen.

In the differential mode (Fig. 1.b), both electron probes pass through the specimen. The separation of the beam paths, which is adjustable by the biprism voltage as well as the excitation of the condensor and/or objective lenses [6], can be made as small as ten nanometers. The area defining the enclosed magnetic flux is approximately constant for every point in the hologram. In this mode the phase of an uniformly magnetized domain in a specimen of constant thickness is constant, in contrast to the absolute mode, where the same domain has a linearly varying phase. The phase difference $\Delta\phi \propto \iint \mathbf{B} d\mathbf{S} \equiv B_n s t$, where B_n is the component of the magnetic field normal to the plane determined by the wave vectors of the two split electron probes, s is the separation of the beam paths projected into the specimen plane and t is the (constant) thickness. The differential mode is advantageous for the investigation of magnetic domain wall profiles and allows straightforward interpretation of the magnetic microstructure [5]. Since this mode does not require a vacuum reference wave, no assumption has to be made about the flatness of the phase in vacuum. This becomes advantageous in the case of strong leakage fields and for the observation of features far away from any holes in the specimen.

In far-out-of-focus holography artefactual contrast is contained in the reconstructed phase and amplitude images that is a direct consequence of the defocus Δf . Fresnel fringes appear near edges or holes and may obscure the magnetic contrast of reconstructed holograms. The

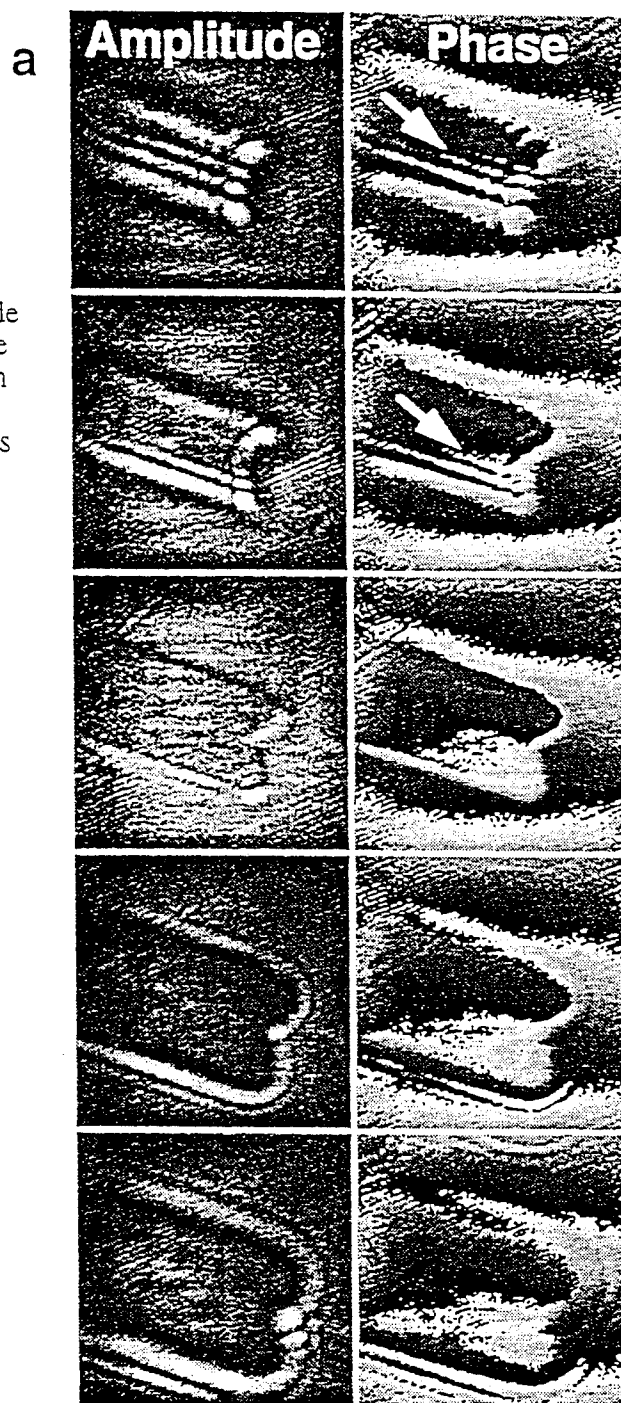


Figure 2. Defocus correction.
 (a - right) Through-focal series of amplitude and phase generated from a sideband of the hologram. Top row - overfocus, center - in focus, lower row - underfocus.
 (b - below) Line scans of five phase images corrected by different defoci near the optimum defocus.

defocus aberration can be eliminated by multiplying the isolated sideband by a function equivalent to the inverse contrast transfer function of the objective lens, $e^{-2\pi i\chi(q)}$ with a defocus phase shift given by $\chi(q) = \lambda^2 \Delta f q^2 / 2$, where q is the spatial frequency and λ the electron's wavelength [10]. The spherical aberration contribution to the phase shift can be neglected for the electron-optical conditions employed here (long focal length and resolution limit ~ 1 nm). A through focal series, shown in Fig. 2a, has been generated from the hologram of a small elongated CrO_2 particle by applying successive defocus phase corrections. Note the false phase line contrast present in both under- and overfocus images (arrows). The minimization of the standard deviation of the amplitude in vacuum has been found to be the most reliable criterion for the determination of optimum defocus, which can be loosely described as the condition for the vanishing of Fresnel fringes. A series of five line-scans of phase images corrected with defoci near the optimum value has been used for a quantitative evaluation of the phase error as a function of defocus. A plot of five line scans (Fig. 2b) reveals a maximum phase variation of 0.3 rad within a $\pm 2\%$ interval of the apparent correct defocus. This level of phase uncertainty is of the same order of magnitude as that due to noise in the phase measurement in vacuum.

4. APPLICATIONS

Both STEM holography modes, accompanied by the Fresnel and Differential Phase Contrast modes of Lorentz microscopy have been used to characterize thin magnetic films, magnetic multilayer structures and small magnetic particles. Thin magnetic films have been described in detail earlier [5]; here we concentrate on multilayer structures and small particles.

4.1. Multilayer Structures

4.1.1. Co/Pd

A Co/Pd superlattice, $\text{Pd}(20\text{nm})/[\text{Co}(1\text{nm})\text{Pd}(1.1\text{nm})]_{10}$, which was grown on an amorphous carbon film was imaged using STEM electron holography. Hysteresis loop measurements indicated a dominant in-plane magnetization with saturation magnetization $M_s =$

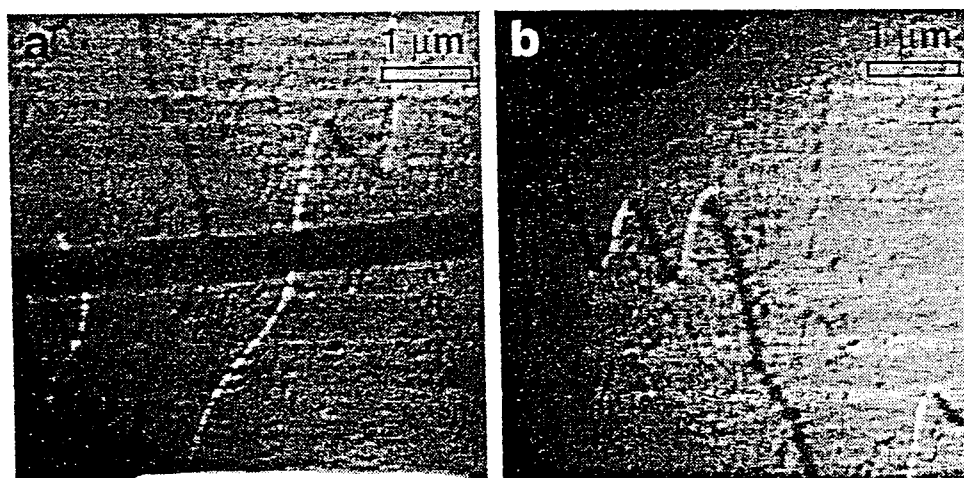


Figure 3 (a) and (b). Fresnel mode images of Co/Pd multilayer structures.

1600 kA/m and coercitive field $H_{C||} = 7\text{kA/m}$.

The Fresnel mode images (Fig. 3a, b) display a typical distribution of magnetic domain walls appearing as white and dark lines (note in Fig. 3a the broad dark biprism shadow and the edge which is parallel to the biprism at the bottom of Fig. 3a). Near an edge or hole, the domain walls become nearly parallel to each other, running approximately perpendicularly to the specimen's edge. Further away from the edge, the magnetization begins to curl forming typical 'w' shaped domain walls (Fig. 3b). A phase image, reconstructed and unwrapped from a hologram acquired in the absolute mode of STEM holography (Fig. 4a) and a three-dimensional map of the marked area (Fig. 4b) shows that the magnetization is oriented perpendicular to the edge of the sample and rotates by 180° when crossing the domain wall, a result consistently observed in different specimen regions. The overlapping rectangles in Fig. 4a are remnant of the unwrapping process. The rectangles are pasted sections from phase images with a successively added or subtracted constant phase value. A line scan of the phase, taken along the edge and averaged over a uniform region 150nm across (Fig. 4c) shows the linear dependence of the phase inside the domains I and II and the location of the domain wall. The slope of the phase absolutely determines the magnitude of magnetization inside the domains for uniform thickness films. In this case the phase gradient is 28.1 mrad/nm in domain I and 11.7 mrad/nm in domain II. The value in domain I agrees well with the theoretically predicted value for all Co layers ferromagnetically aligned throughout the superlattice stack. Assuming a total Co thickness of $10 \times 1.0 \text{ nm} = 10 \text{ nm}$ with uniform bulk saturation magnetization of 1440 emu/cm^3 , i.e. $(x 4\pi 10^{-4} =) B = 1.8096 \text{ T}$, the phase gradient in units of rad/nm equals

$$\frac{\Delta\phi}{\Delta x} = \frac{e}{\hbar} \iint \mathbf{B} \cdot d\mathbf{S} / \Delta x = \frac{e}{\hbar} B t = 27.49 \text{ mrad/nm}, \quad (2)$$

i.e. within 2% of the measured value. The magnetization in domain II is $\sim 42\%$ of the expected ferromagnetically aligned bulk value. This suggests that not all magnetic layers in domain II are

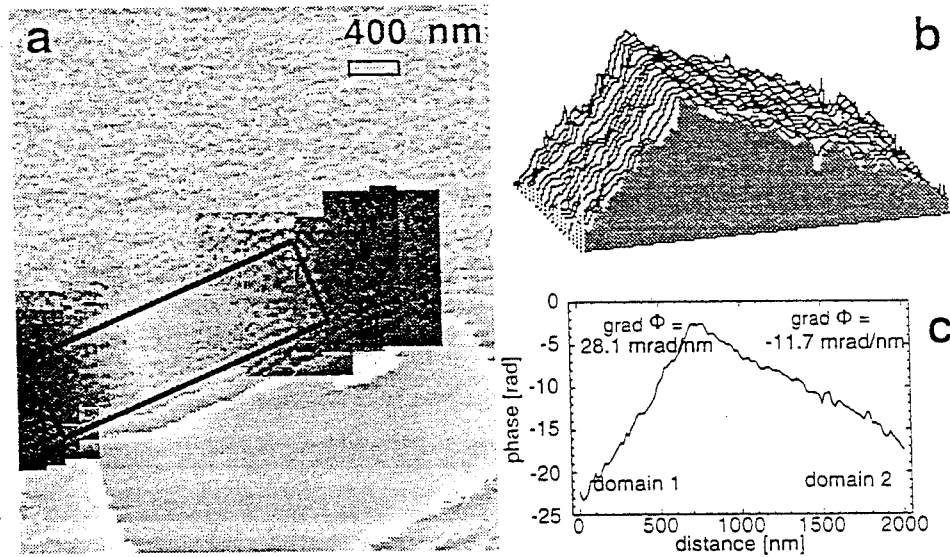


Figure 4. Partially unwrapped phase image (a) of domain structure near the edge of a Co/Pd multilayer, (b) three-dimensional plot of the phase in the region marked in a, (c) line-scan of phase along specimen edge, averaged across 150nm.

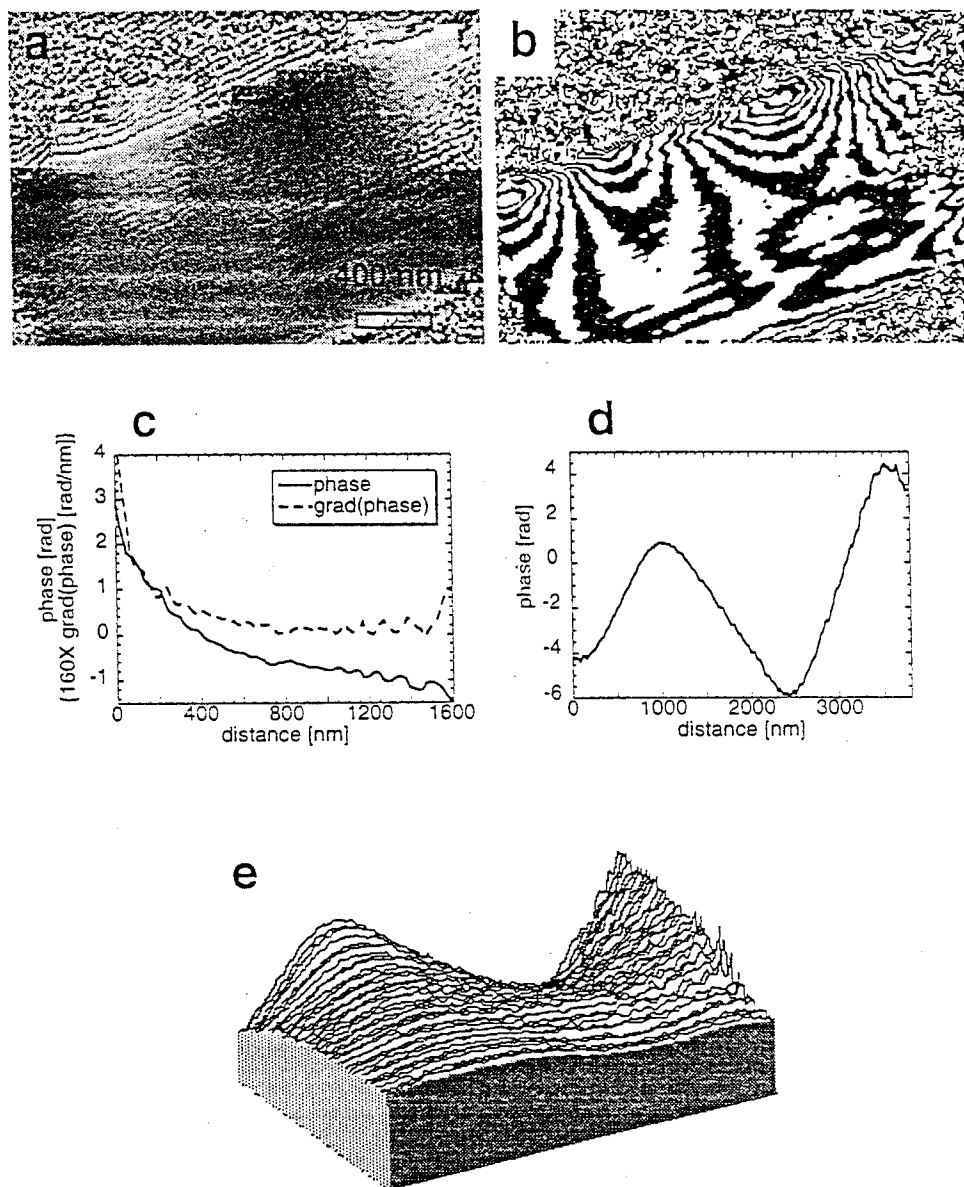


Figure 5. Leakage fields in Co/Pd multilayer films : (a) unwrapped phase image, (b) contour image of same area as in (a) where 1 contour corresponds to $\pi/9$ rad, (c) line-scan of phase perpendicular to edge and its gradient, (d) line-scan of phase parallel to the edge, (e) three-dimensional plot of phase outside the specimen.

magnetized in the same direction (assuming only in-plane magnetization). The measured value indicates that the magnetization vectors in the layers must be oriented with 7 layers in one direction and three layers in the opposite direction producing a net integrated magnetization of 40% of the saturated value.

While observing the magnetic structure near the specimen edge, a strong magnetic flux leak was observed in the surrounding vacuum (Fig. 5). The reconstructed, unwrapped phase (Fig. 5a) and contour image (Fig. 5b) of the same area displays the periodically changing phase; the contours are equimagnetic-induction lines and make the magnetization flow more visible. The line-scan in Fig. 5c, taken in a direction perpendicular to the film edge, shows the decay of the leakage field. The gradient of the phase, which is proportional to the projected component of the magnetic induction parallel to the edge, reveals that the this field falls to $1/e$ of its maximum value at a distance approximately 150nm from the edge. The ripple in the right part of the profile is due to the Fresnel fringes of the biprism, which in principle can be removed by subtracting a phase image of free space. A comparison of the line-scan parallel to the film's edge (Fig. 5d) and a Lorentz image of the same area shows that the domain walls terminate at inflexion points of the phase curve and near the center of a domain the phase is at maximum or minimum. A three-dimensional plot of the phase in the space near the edge is shown in Fig. 5e.

Investigations of the magnetic microstructure in regions far away from a hole are carried out in the differential mode of STEM holography. In this mode, the phase represents a direct

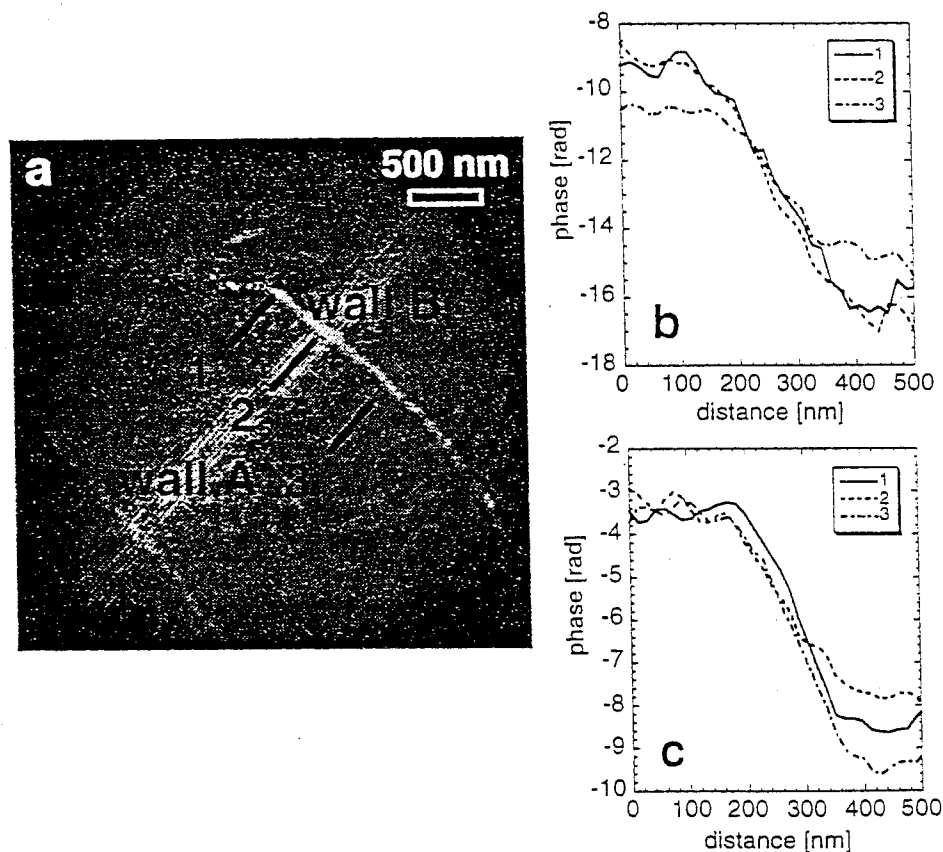
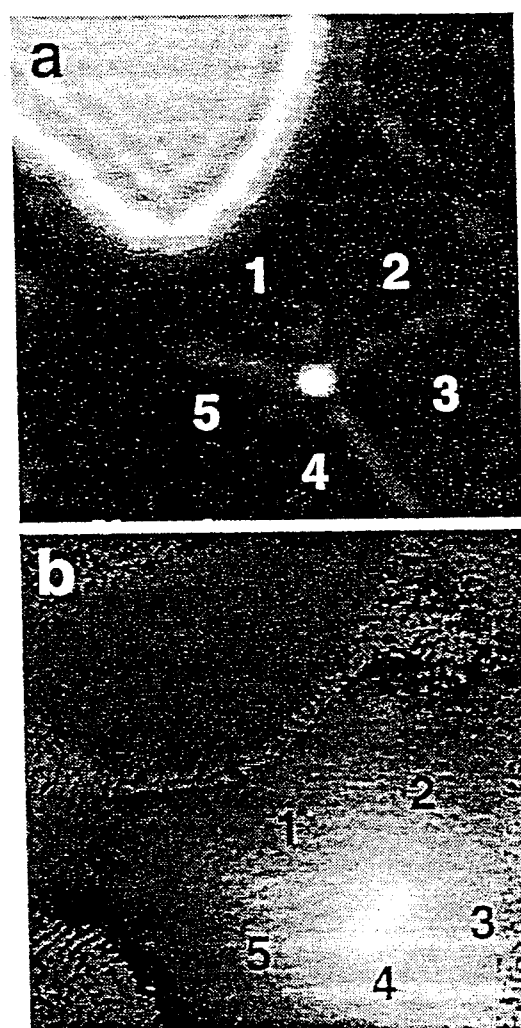


Figure 6. Domain walls in Co/Pd multilayer films : (a) hologram with marked walls and line profile positions, (b) profiles of broader wall A, (c) profiles of wall B.

measure of the magnetic field in the specimen and displays a constant phase value in regions of constant magnetization. This is advantageous for the investigation of domain wall profiles. A series of holograms (positions 1 through 3 in Fig. 6a) yields a set of 3 domain wall profiles for each of the two marked domain walls A, B. The average domain wall width is 245 nm (wall A) and 200 nm (wall B). The difference in mean domain wall width is likely related to the presence of partial antiferromagnetic coupling within the superlattice stack.

4.1.2. Co/Cu

Magnetic coupling between adjacent ferromagnetic layers in a superlattice composed of alternating ferromagnetic and nonmagnetic layers is present when giant magnetoresistance is observed. A series of multilayer structures with varying seed layer thickness, number of bilayers and bilayer geometry have been grown under UHV conditions. Samples grown on thin amorphous holey carbon films are observed in the Fresnel mode with the beam



domain #	phase gradient [mrad/nm]
1	41.2
2	41.8
3	39.8
4	36.7
5	40.7

Table 1. Phase gradients in domains 1-5 measured from Fig. 7b.

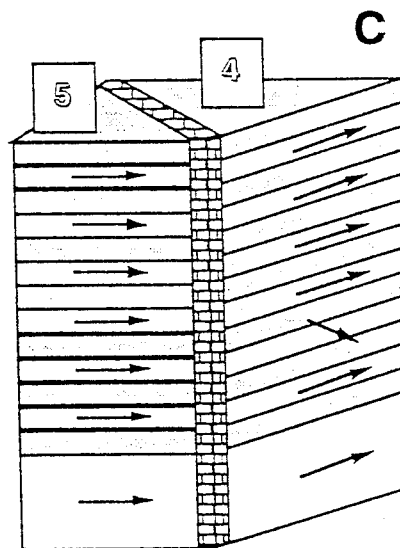


Figure 7. Underfocus Fresnel image (a, $1.4\mu\text{m}^2$) and partially unwrapped absolute phase image (b) of a Co/Cu multilayer. The proposed micromagnetic structure is shown in (c).

perpendicular to the layers of the superlattice (not cross-sectional view). Images reveal the position of domain walls as bright or dark bands and holograms of identical regions yield quantitative information on the domain. The variation of the magnitude of magnetization can be used to determine the interlayer coupling [10] assuming in-plane magnetization. For example, the Fresnel image of a $\text{Co}(6\text{nm})/[\text{Cu}(3\text{nm})\text{Co}(1.5\text{nm})]_6/\text{Cu}(3\text{nm})$ superlattice shows five domains aligned in a flux vortex (Fig. 7a). From the hologram, acquired in the absolute mode (Fig. 7b), the maximum phase gradients are determined in each of the five domains (table 1). The average maximum phase gradient in domains 1, 2, 3 and 5 is 41.0 ± 0.6 mrad, which differs from the predicted bulk value for a cobalt film of 15 nm total thickness (41.4 mrad/nm) by less than 1%. This indicates that the domains penetrate the sandwich and are uniformly (ferromagnetically) aligned. The phase gradient in domain 4 is 36.7 mrad/nm, which is approximately 90% of the expected uniformly magnetized value (37.3 mrad/nm). A proposed explanation of this magnetization amplitude loss is outlined in Fig. 7c. The magnetization in one of the layers (10% of the active thickness) is rotated by 90° with respect to the magnetization in the other layers. The amplitude must then be calculated as a vector sum, i.e.

the magnetization amplitude equals to $\sqrt{0.1^2 + 0.9^2} \cong 0.906$ and therefore approximately 10% lower than the aligned value. If a single layer were antiferromagnetically aligned in the superlattice stack within this domain, the phase gradient would have to be 80% of the maximum value. The existence of 90° coupling between layers has been confirmed by hysteresis loop measurements performed on the same sample [11]. This confirms that we are able to determine the orientation of domains in a superlattice and thereby are capable of correlating macroscopic giant magnetoresistance measurements with micromagnetic structure.

4.2. Small Particles

Magnetic properties of small magnetic particles, which are used in magnetic recording technology, are strongly influenced by their magnetic microstructure, size and morphology. Direct quantitative investigations of the magnetic microstructure in small magnetic particles has been limited by the relatively low spatial resolution of commonly used micromagnetic analysis techniques (magneto-optical methods, magnetic force microscopy, Bitter-pattern method, etc.). The Fresnel and Differential Phase Contrast (DPC) modes of Lorentz microscopy reveal the in-plane component of magnetization as well as the local microstructure at high spatial resolution, but do not allow accurate quantitative measurements. The deflection angle in the DPC mode is too small ($\sim 10^{-5}$ rad) and in the Fresnel mode, only strong magnetization changes (domain walls, ripple) are observed; an image deconvolution with an exact value of defocus and known wall profile would be required to explicitly extract the micromagnetic structure. Electron holography, carried out in a STEM, provides quantitative information about the magnetization in the specimen at nanometer resolution and therefore represents a valuable tool for the determination of the magnetic microstructure in small particles. Reconstructed amplitude and phase images of particles smaller than $\sim 1\mu\text{m}$ are strongly obscured by Fresnel fringes. These fringes must be removed with a defocus correction during the holography reconstruction process.

4.2.1. CrO_2

CrO_2 particles are elongated 'stretch shaped' particles (approx. 50-100 nm wide and 300-400 nm long) with a magnetic moment of 93 emu/g (~ 400 emu/cm³) and a coercive field of 405 Oe. Holograms of single particles acquired in the absolute mode confirm the prediction that the particles are uniformly magnetized. Micromagnetic calculations of the three-dimensional magnetic fields and phase differences have been carried out for comparison with experimental phase images since phase images of three-dimensional fields from small particles are difficult to interpret directly. Fig. 8 shows the calculated phase image of a $640\text{nm} \times 80\text{nm} \times 40\text{nm}$ particle, magnetized uniformly (saturation magnetization 400 emu/cm³) along the x axis. The phase is obtained by integrating the B_x component along y and z (fringes parallel to dipole, Fig. 8a),

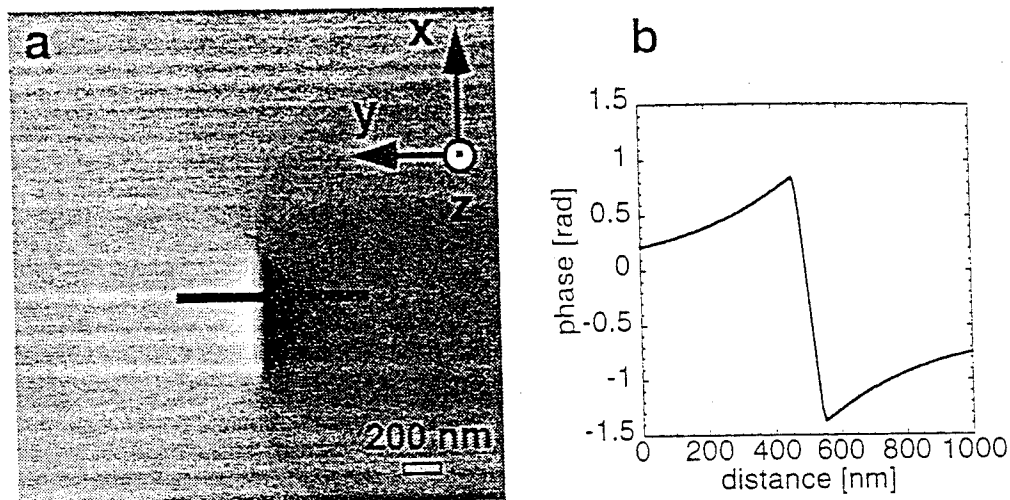


Figure 8. Calculated phase image (a) of a 640nmx80nmx40nm magnetic particle uniformly magnetized in the x direction. The line-scan (b) is taken along the line in a.

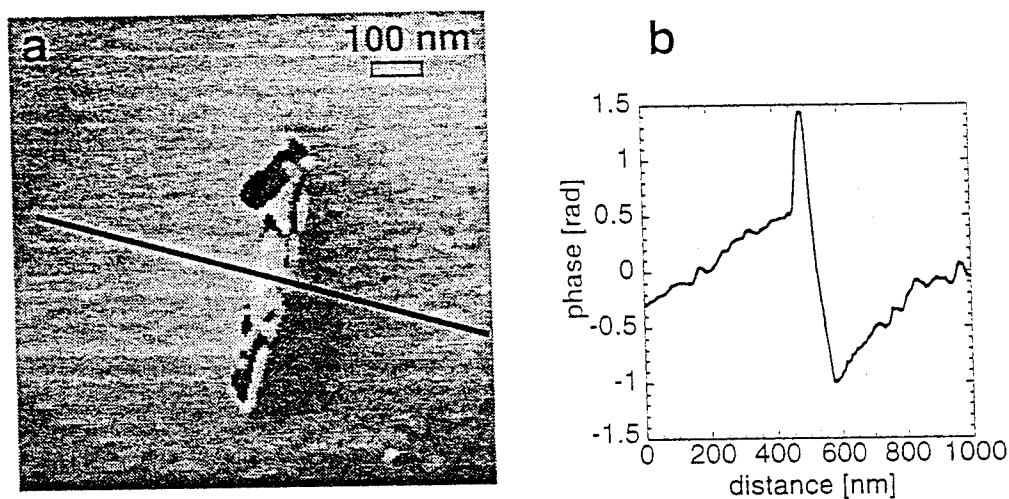


Figure 9. Absolute phase image of a CrO₂ particle (a) and line-scan (b) along line in a.

where the beams propagate along the z axis and the reference wave is assumed to have zero phase. Typical bright and dark contrast observed outside the particles is in good qualitative agreement with the experimental image (Fig. 9a). Absolute phase shifts caused by the magnetic dipole can be determined. The experimental line-scan across the particle (Fig. 9b) shows that the phase gradient inside the particle is approximately 26 mrad/nm, which compares favorably with the calculated image (25 mrad/nm). We note that an accurate value of the thickness is

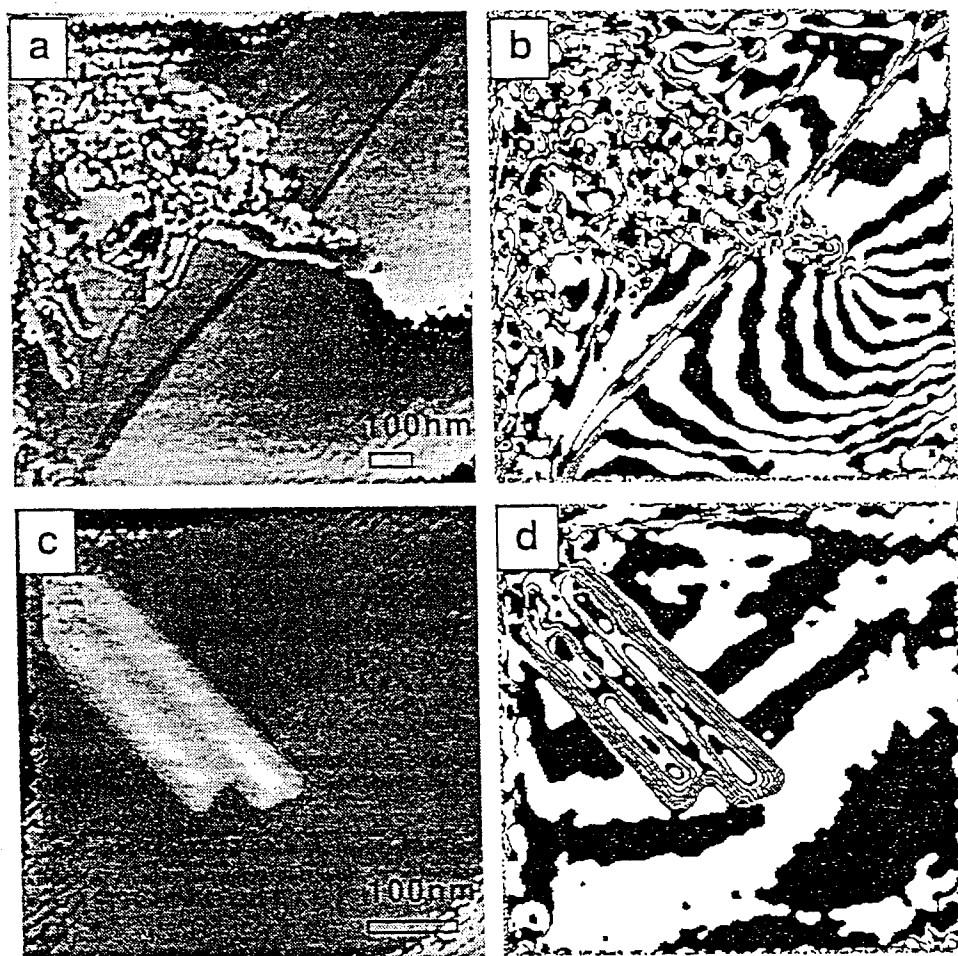


Figure 10. Interaction of CrO_2 particles : (a) and (c) - phase images, (b) and (d) - contour images, 1 contour corresponds to $\pi/10$ rad.

difficult to obtain from the experiment (large tilt or knowledge of the mean free path is required). Differences in the line-scans may be due to the non-uniform magnetization of the particles, thickness changes or scattering effects at the particle surface (edges).

The interaction of CrO_2 particles is illustrated in Fig. 10. The magnetizations of the two CrO_2 particles near the edge of the supporting carbon film (Fig. 10 (a) and (b) - phase and contour image) are aligned parallel, which manifests itself as a strong leakage field. By comparison, the two CrO_2 particles in Fig. 10 (c) and (d) (phase and contour image) are aligned antiparallel, the magnetic flux is closed, and no flux leak is observed.

4.2.2. FeB

FeB particles ($H_c=605$ Oe, magnetic moment 52.8 emu/g) have a hexagonal platelet form, typically 100 nm in diameter and ~ 20 nm thick. In Fig. 11, the STEM (a), amplitude (b) and phase image (c) of an FeB particle are compared. The phase images display a nearly constant phase difference across and around the whole region of the particle confirming that the magnetization is perpendicular to the platelet.

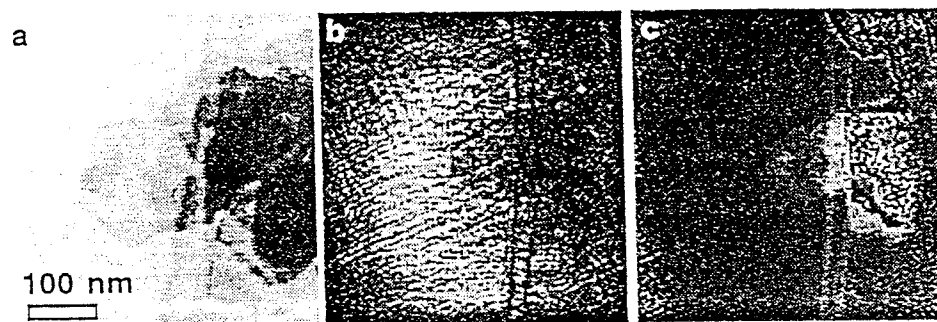


Figure 11. A STEM (a), amplitude (b) and phase (c) image of FeB platelets.

5. ACKNOWLEDGMENTS

This work was supported by the NSF under grant DMR-9110386, and the Office of Naval research under grant #N00014-93-1-0099. The electron microscopy was performed in the Center for High-Resolution Electron Microscopy at ASU supported by the NSF grant DMR91-15680. We are grateful to A. A. Higgs for the flawless operation of the HB 5 microscope, P. Perkes for help with the image processing, J. C. Wheatley and C. Weiss for inspiration and help during specimen preparation and Dr. J. K. Weiss of Emispec Systems for creative image acquisition software.

REFERENCES

1. L.M. Falicov et al., J.Mater.Res. **5** (1990) 1299.
2. S.S.P. Parkin, R. Bhadra and K.P. Roche, Phys. Rev. Lett. **66** (1991) 2152.
3. M.N. Baibich, J.M. Broto, A. Fert, F. Nguyen Van Dau, F. Petroff, P. Etienne, G. Creuzet, A. Friederich and J. Chazelas, Phys. Rev. Lett. **61** (1988) 2472.
4. S.D. Bader, J. Magn. Magn. Mater. **100** (1991) 440.
5. M. Mankos, M. R. Scheinfein and J. M. Cowley, J. Appl. Phys. **75** (1994) 7418-24.
6. M. Mankos, A. A. Higgs, M. R. Scheinfein and J. M. Cowley, Ultramicroscopy (in press).
7. G. Möllenstedt and H. Düker, Z. Phys. **145** (1956) 377.
8. M. R. McCartney and M. Gajdardziska-Josifovska, Ultramicroscopy **53** (1994) 283.
9. Y. Aharonov and D. Bohm, Phys. Rev. **115** (1959) 485.
10. M. Mankos, Z. Yang, M. R. Scheinfein and J. M. Cowley, IEEE Trans. Magn. (in press).
11. Z. Yang and M. R. Scheinfein, Appl. Phys. Lett. (submitted).

Abstracts / Session
APS March Mtg
San Jose, CA
March 95

Abstract Submitted
for the Mar95 Meeting of
The American Physical Society

Sorting Category: 36f. Surface Magnetism

Superparamagnetism and Long-Range Exchange in Nanometer-Sized Fe Islands on $\text{CaF}_2/\text{Si}(111)$.* KEVIN R. HEIM, GARY G. HEMBREE, MIKE R. SCHEINFELD, *Arizona State University* — The effective magnetic moment was measured as a function of Fe island size during the initial stages of Fe growth on $\text{CaF}_2/\text{Si}(111)$. The ultrathin Fe films were grown in a nanometer transverse resolution secondary electron microscope equipped with an in situ surface magneto-optic Kerr effect analysis chamber for magnetic measurements. Fe grown on room-temperature CaF_2 initially forms superparamagnetic 3-D islands with a narrow size distribution and an average separation of a few nanometers. Increased Fe coverages lead to 2-D island growth as the hemispherical islands gradually connect and form "meandering" islands. These islands remain superparamagnetic for coverages greater than 20 ML. Beyond this, ferromagnetic behavior with an in-plane easy axis is observed. The effective moment varies linearly with the average Fe island area for coverages between 7 and 30 ML. Ag films deposited on superparamagnetic $\text{Fe}/\text{CaF}_2/\text{Si}(111)$ specimens yielded surfaces where the Ag islands covered several Fe islands. The in-plane effective moment was found to be proportional to the mean number of Fe islands covered by an average-sized Ag island, implying that the Ag mediates the magnetic exchange between individual Fe islands within a Ag island.
* Supported by ONR Grant N00014-93-1-0099.

☒ Prefer Oral Session
☐ Prefer Poster Session

Date submitted: December 1, 1994

Kevin R. Heim
heim@phyast.la.asu.edu
Physics Department
Arizona State University

Electronic form version 1.0

90° COUPLING IN CO/CU GIANT MAGNETORESISTANCE SUPERLATTICES*

Z.J. Yang and M.R. Scheinfein

Department of Physics Arizona State University Box 871504 Tempe, AZ 85287-1504

Introduction

The strength and sign of the interlayer coupling coefficient in superlattices composed of ferromagnetic transition metals and non-magnetic spacer layers has been correlated with magneto-transport measurements for a wide class of systems [e.g. 1]. Models based on an RKKY-like treatment which couple spanning vectors normal to the superlattice layers that join extremal points of the bulk Fermi surface have successfully predicted the oscillation periods of interlayer coupling. Magnetotransport models which rely on antiferromagnetic alignment of adjacent ferromagnetic layers have been used to interpret experimental data [2]. Interlayer coupling can be complicated by surface and interface roughness, primarily due to conditions during growth. Theoretical treatments attribute 90° degree coupling between layers to spatial nanoscopic variations in the interlayer coupling arising from thickness variations [3,4]. Bilinear (180°) coupling in general coexists with the higher order biquadratic (90°) coupling [5]. Here, we demonstrate the strong correlation between giant magnetoresistance and 90° coupling between domains (in adjacent layers) in electron beam evaporated Co/Cu superlattices as a function of the Cu interlayer spacing when the interfaces are imperfect.

Experimental Results

We have grown $[\text{Co}_{1.5} \text{ nm}/\text{Cu}]_n$ ($7 < n < 13$) superlattices by room temperature evaporation in a UHV dual e-beam evaporation system on Si(100) oriented crystals. 6.0 nm thick Co layers were grown at 250° C as buffer layers on the substrates. 4.5 nm thick Co capping layers covered the superlattices. The total superlattice thickness ranged between 32 and 46 nm. Deposition rates were 0.3~1 Å/s at a base pressure 5×10^{-9} mbar.

In Fig. 1, the magnetoresistance at room temperature (solid squares) and at 77K (solid triangles) are plotted as a function of the Cu interlayer thickness of the superlattice $\text{Co}_{4.5\text{nm}}[\text{Co}_{1.5\text{nm}}\text{Cu}]_n/\text{Co}_{6.0\text{nm}}/\text{Si}(100)$ ($7 < n < 13$). The oscillation period of interlayer coupling is about 1nm, within the accepted range of Cu spacer thickness values. Evident is the suppression of the first MR maximum and a reduction in the value for the MR, characteristic of films with rough interfaces. The maximum normalized magnetization oriented at 90° with respect to the field direction, M_y (or M_{90}/M_{sat}) is also shown (solid circles). The peaks in the 90° oriented magnetization correspond with the peaks in the magnetoresistance data at approximately t_{Cu} of 0.8, 2.0 and 2.8 nm. Strong 90 degree coupling is still present at the first oscillation maximum even though the value of the MR is strongly suppressed.

The crystallographic and superlattice structure was studied with x-ray diffraction (Cu-K α radiation $\lambda=0.15405\text{nm}$), cross-sectional transmission electron microscopy (TEM) and planview

scanning transmission electron microscopy (STEM). The Large Angle X-Ray Scattering (LAXS) data are characterized by a low intensity fcc (111) Co (Cu) peak indicating that the multilayers have a weak (111) out-of-plane texture. The width of this peak was used to estimate an average grain size between 8-10 nm, a result confirmed by STEM. Only first and second order Small Angle X-Ray Scattering (SAXS) peaks with superlattice character Kiessig fringes were observed indicating the interfaces were relatively rough, shown in Fig. 2. The rms-roughness of the interfaces was estimated with a dynamical calculation of the SAXS spectra, also shown (offset) in Fig. 2. The interface roughness is ± 2 nm for the bottom half of the superlattice stack and ± 4 nm for the top half of the superlattice stack. The bilayer thicknesses calculated from SAXS Bragg peaks are in good agreement with the nominal values. A defocused cross sectional TEM (200 keV) image (90 nm across) of $\text{Co}_{4.5}\text{nm}[\text{Co}_{1.5}\text{nmCu}_{2.0}\text{nm}]_8/\text{Co}_{6.0}\text{nm}/\text{Si}(100)$, shown in Fig. 3, illustrates the overall integrity of the interface structure. The RMS interface roughness as estimated from the TEM images agrees with values extracted from the SAXS simulations. This data and theoretical models can be used to set an upper limit on the intrinsic coupling strength.

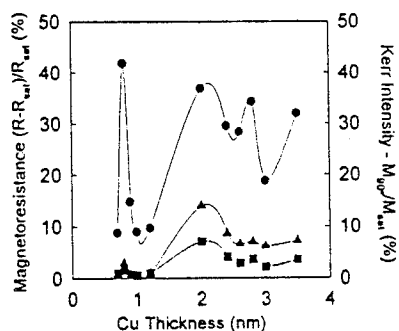


Fig. 1. 90 degree coupling (solid circles), MR 77K (solid triangles) and MR 300K (solid squares).

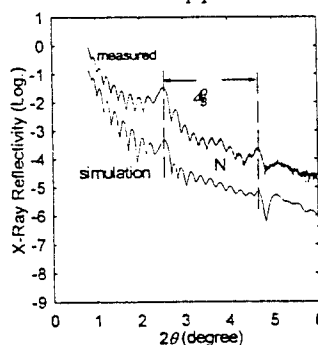


Fig. 2. Measured (top) and simulated (bottom) SAXS spectra.

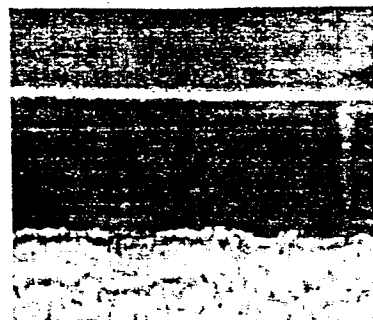


Fig.3. TEM image of $\text{Co}_{4.5}\text{nm}[\text{Co}_{1.5}\text{nmCu}_{2.0}\text{nm}]_8/\text{Co}_{6.0}\text{nm}/\text{Si}(100)$. Si on top.

References

- [1] M.N. Baibich, J.M. Broto, A. Fert, F. Nguyen Van Dau, F. Petroff, P. Etienne, G. Creuzet, A. Friederich, J. Chazelas, Phys. Rev. Lett. **61**, 2472 (1988); S.S.P. Parkin, N. More, K.P. Roche, Phys. Rev. Lett. **64**, 2304 (1990); P. Grunberg, J. Barnas, F. Saurenbach, J.A. Fuß, A. Wolf, M. Vohl, J. Mag. Mag. Mat. **93**, 58 (1991); S.S.P. Parkin, Phys. Rev. Lett. **67**, 3598 (1991).
- [2] P.M. Levy, S. Zhang, A. Fert, Phys. Rev. Lett. **65**, 1643 (1990); S. Zhang, P.M. Levy, Phys. Rev. **B47**, 6776, (1993); P.M. Levy, H.E. Camblong, S. Zhang, J. Appl. Phys. **75**, 7076 (1994); J.L. Duvail, A. Fert, L.G. Pereira, D.K. Lottis, J. Appl. Phys. **75**, 7070 (1994).
- [3] J.C. Slonczewski, Phys. Rev. Lett. **67**, 3172 (1991).
- [4] R. Ribas, B. Dieny, J. Mag. Mag. Mat. **121**, 313 (1993).
- [5] M.E. Filipkowski, C.J. Gutierrez, J.J. Krebs, G.A. Prinz, J. Appl. Phys. **73**, 5963 (1993).

*This work is supported by the Office of Naval Research under grant N-00014-93-1-0099.

Intermag-95 Digest
San Antonio, TX
April 95

NANOMAGNETOMETRY : ELECTRON HOLOGRAPHY OF SMALL PARTICLES*

M. Mankos, J.M. Cowley and M.R. Scheinfein

Department of Physics Arizona State University Box 871504 Tempe, AZ 85287-1504

Introduction

We have been using electron holography in an HB 5 scanning transmission electron microscope (STEM) to perform quantitative investigations of magnetic microstructure in thin magnetic specimens. Holograms are acquired in the far-out-of-focus scheme where the objective lens is operated at large defocus, such that a relatively large area of the specimen is illuminated, and the scanning is switched off. A detailed description of the holography instrumentation and theory is given elsewhere [1,2]. In principle, the electron probe is split into two electron wave packets which are transferred by the lenses into two fine electron probes coherently illuminating the specimen. The two wave packets interact with the specimen and form an interference pattern (hologram), from which the amplitude and relative phase of the two electron waves can be extracted. Interactions with magnetic materials produce absolutely calibrated phase differences which are proportional to the magnetic flux enclosed by the two beam paths as they traverse the specimen.

Experimental Results: CrO₂ Small Particles

Direct quantitative investigations of the magnetic microstructure in small magnetic particles has been limited by the relatively low spatial resolution of commonly used micromagnetic analysis techniques (magneto-optical methods, magnetic force microscopy, Bitter-pattern method, etc.). The Fresnel and Differential Phase Contrast (DPC) modes of Lorentz microscopy reveal the in-plane component of magnetization as well as the local microstructure at high spatial resolution, but do not allow accurate quantitative measurements. The deflection angle in the DPC mode is too small ($\sim 10^{-5}$ rad) and in the Fresnel mode, only strong magnetization changes (domain walls, ripple) are observed. However, electron holography provides quantitative information about the magnetization in the specimen at nanometer spatial resolution.

As an example, we examine the micromagnetic structure of a CrO₂ particle with a magnetic moment of 400 emu/cm³ and a coercive field of 405 Oe. Holograms of isolated single particles confirm the prediction that the particles are uniformly magnetized. Micromagnetic calculations of the three-dimensional magnetic fields and phase differences have been carried out for comparison with the experiment. Fig. 1a shows the calculated phase image of a 350 x 50 x 20 nm³ particle, uniformly magnetized along the x axis. Bright and dark phase contrast, typical of dipole fields, is observed outside the particle. A line scan across the particle, shown in Fig. 1b, has a phase gradient of 26 mrad/nm. The experimental image is shown in Fig. 2a. The experimental phase gradient across the particle is 25 mrad/nm. The phase change across the particle is directly proportional to the total flux along its length, and hence can be used to determine the magnetization. Here, the experimental saturation magnetization within the particle is 384 emu/cm³, within 4 % of the theoretical value. The magnetization sensitivity of this measurement

indicates that we can detect 1.4×10^{-13} emu. The limit of this technique as we have implemented it is almost 4 orders of magnitude more sensitive (10^{-17} emu), some 8 orders of magnitude more sensitive than a SQUID magnetometer.

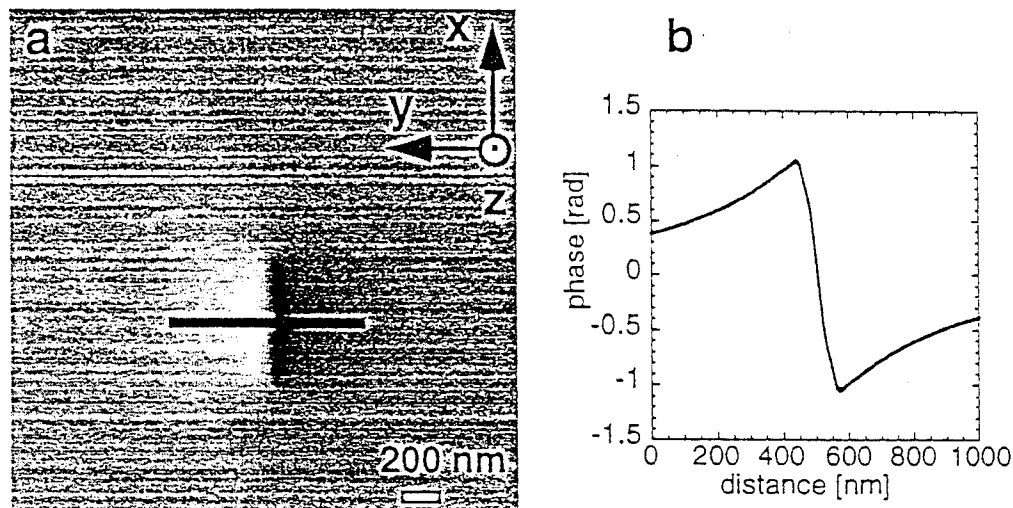


Figure 1. Calculated phase image (a) of a $350 \times 50 \times 20 \text{ nm}^3$ magnetic particle uniformly magnetized along the x direction. The line-scan (b) is taken along the mark in a.

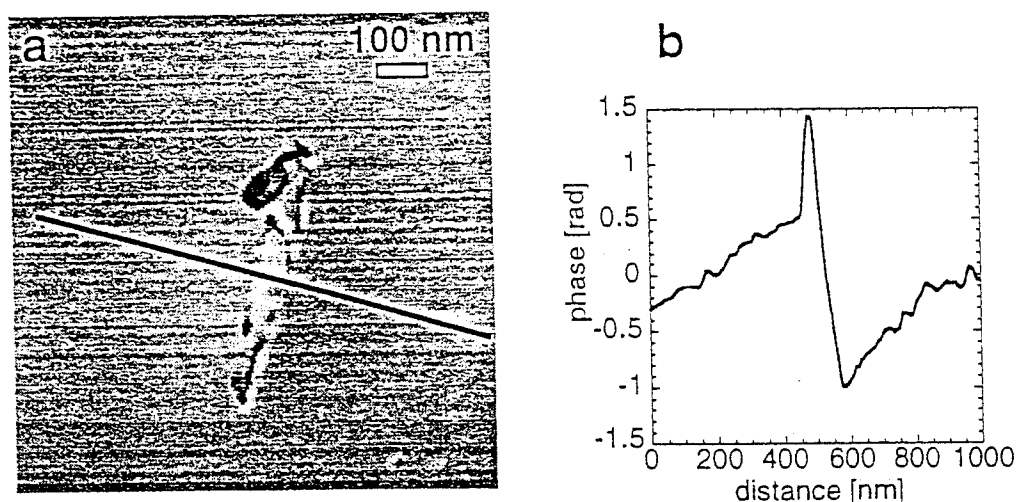


Figure 2. Absolute phase image of a $350 \times 50 \times 20 \text{ nm}^3$ CrO_2 particle (a) and line-scan (b) along mark in a.

References

- [1] M. Mankos, M. R. Scheinfein and J. M. Cowley, J. Appl. Phys. **75** (1994) 7418-24.
 - [2] M. Mankos, A. A. Higgs, M. R. Scheinfein and J. M. Cowley, Ultramicroscopy (in press).
- This work is supported by the Office of Naval Research under grant N-00014-93-1-0099 and the National Science Foundation under grant DMR-91-10386 and DMR-91-15680.

STEM HOLOGRAPHY OF MAGNETIC MATERIALS

Marian Mankos, M. R. Scheinfein and J. M. Cowley

Department of Physics and Astronomy, Arizona State University,
Box 871504, Tempe, AZ 85287-1504, U.S.A.

We have been using electron holography in an HB 5 scanning transmission electron microscope (STEM) to perform quantitative investigations of magnetic microstructure in thin magnetic specimens. Holograms are acquired in the far-out-of-focus scheme with the scanning switched off. The objective lens is operated at large defocus, therefore a relatively large area of the specimen is illuminated. Our system allows for flexible operation of off-axis holography modes, while allowing for simultaneous observation in Fresnel and Differential Phase Contrast (DPC) modes of Lorentz microscopy. This combination of micromagnetic analysis techniques in one instrument provides a valuable tool for the investigation of magnetic microstructure at 1 nm spatial resolution.

We have isolated two distinct holography modes : the absolute and differential [1]. In the absolute mode, one of the two electron probes travels through vacuum, while the other passes through the specimen. Assuming zero phase in vacuum and prior knowledge of the specimen thickness, we can absolutely determine the phase shift caused by the electromagnetic fields present in the specimen. For a magnetic specimen the phase shift is proportional to the magnetic flux enclosed by the two beam paths. In a uniformly magnetized domain located near the edge of a specimen of constant thickness the phase difference ϕ changes linearly with increasing distance from the edge and $\phi = \int \mathbf{B} \cdot d\mathbf{S} \equiv B_n x t$, where B_n is the component of the magnetic field normal to the plane determined by the wave vectors of the two split electron waves, x is the distance from the edge and t is the (constant) thickness. The gradient of the phase determines the magnitude of B_n (averaged over the film thickness) in the domain. For a film of nearly constant thickness we can neglect the contribution of the constant phase of the electrostatic field present in the specimen, since quantitative information is derived from the gradient of the phase difference. In the differential mode, unique to STEM holography, both of the split electron waves pass through the specimen. The separation of the beam paths, which is adjustable by the biprism voltage as well as the excitation of the condensor and/or objective lenses [2], can be made as small as ten nanometers. The area defining the enclosed magnetic flux is approximately constant for every point in the hologram. In this mode the phase of an uniformly magnetized domain is constant, in contrast to the absolute mode, where the same domain has a linearly varying phase difference. The differential mode is advantageous for the investigation of magnetic domain wall profiles and allows straightforward interpretation of the magnetic microstructure [1]. STEM holography accompanied by the conventional Lorentz microscopy techniques has been used to characterize thin magnetic films, magnetic multilayer structures and small magnetic particles.

Magnetic coupling between adjacent ferromagnetic layers in a superlattice composed of alternating ferromagnetic and nonmagnetic layers is present when giant magnetoresistance is observed. A series of multilayer structures with varying seed layer thickness, number of bilayers and bilayer geometry have been grown under UHV conditions. Fresnel images of multilayer structures reveal the position of domain walls as bright or dark bands. From holograms of identical regions the magnetization in the domains is determined quantitatively. The variation of the magnitude of magnetization is used to determine the interlayer coupling [3]. For example, the absolute hologram of a $\text{Co}(6\text{nm})/[\text{Cu}(3\text{nm})\text{Co}(1.5\text{nm})]_6/\text{Cu}(3\text{nm})$ acquired with the beam perpendicular to the layers of the superlattice shows that in 4 of 5 neighboring domains forming a flux vortex the maximum phase gradient equals to 41.0 ± 0.6 mrad, which agrees favorably with the predicted bulk value for a cobalt film of 15 nm total thickness (41.4 mrad/nm). This indicates that the domains penetrate

the sandwich and are uniformly (ferromagnetically) aligned. The phase gradient in the 5th domain is 36.7 mrad/nm. This value is 10% less than the uniformly magnetized value. If a single layer were antiferromagnetically aligned within this domain, the phase gradient would have to be 20% lower. Therefore, the magnetization in one of the layers (10% of the active thickness) is rotated 90° with respect to the magnetization in the other layers. When the components are added together in quadrature, weighted by the active Co layer thickness, the integrated magnetization is 10% lower than the aligned value. The existence of 90° coupling between layers has been confirmed by hysteresis loop measurements performed on the same sample. With STEM based electron holography, we are able to determine the orientation of domains in a superlattice thereby allowing macroscopic giant magnetoresistance measurements to be correlated with micromagnetic structure.

Magnetic properties of small magnetic particles, which are used in magnetic recording technology, are strongly influenced by their magnetic microstructure, size and morphology. Direct quantitative investigations of the magnetic microstructure in small magnetic particles has been limited by the relatively low spatial resolution of commonly used micromagnetic analysis techniques (magneto-optical methods, magnetic force microscopy, Bitter-pattern method, etc.). The Fresnel and Differential Phase Contrast (DPC) modes of Lorentz microscopy reveal the in-plane component of magnetization as well as the local microstructure at high spatial resolution, but do not allow accurate quantitative measurements. The deflection angle in the DPC mode is too small ($\sim 10^{-5}$ rad) and in the Fresnel mode, only strong magnetization changes (domain walls, ripple) are observed; an image deconvolution with an exact value of defocus and known wall profile would be required to explicitly extract the micromagnetic structure. Electron holography, carried out in a STEM, provides quantitative information about the magnetization in the specimen at nanometer resolution [1] and therefore represents a valuable tool for the determination of the magnetic microstructure in small particles. Unfortunately, reconstructed amplitude and phase images of particles smaller than $\sim 1 \mu\text{m}$ are obscured by Fresnel fringes and must be corrected for during the holography reconstruction process [4]. The defocus value is determined within $\sim 2\%$ and phase variations caused by this inaccuracy are comparable to the noise level of a hologram acquired in free space (maximum deviation ~ 0.3 rad).

CrO_2 particles are elongated 'stretch shaped' particles (approx. 50-100nm wide) with a magnetic moment of 93 emu/g and a coercive field of 405 Oe. Holograms of single particles acquired in the absolute mode confirm the prediction that the particles are uniformly magnetized. Micromagnetic calculations of the three-dimensional magnetic fields and phase differences are necessary for accurate interpretation of the phase images. For a particle of known geometry, a comparison of the calculated and acquired phase shift allows quantitative determination of the particle's magnetization. FeB particles ($H_c=605$ Oe, magnetic moment 52.8 emu/g) have a hexagonal platelet form, typically 100nm in diameter and ~ 20 nm thick. Phase images display a nearly constant phase difference across the whole region of the particles, therefore confirming the predicted magnetic structure that the magnetization is perpendicular to the platelet.

In conclusion, STEM electron holography with its inherent high spatial resolution and ability to deliver quantitative information has become a valuable technique for micromagnetic investigations at the nanometer level.

This work was supported by the NSF under grant DMR-9110386, and the Office of Naval research under grant #N00014-93-1-0099. The electron microscopy was performed in the Center for High-Resolution Electron Microscopy at ASU supported by the NSF grant DMR91-15680.

- [1] M. Mankos, M. R. Scheinfein and J. M. Cowley, J. Appl. Phys. **75** (1994) 7418-24.
- [2] M. Mankos, A. A. Higgs, M. R. Scheinfein and J. M. Cowley, Ultramicroscopy (in press).
- [3] M. Mankos, Z. Yang, M. R. Scheinfein and J. M. Cowley, IEEE Trans. Magn. (in press).
- [4] M. R. McCartney, private communications and computer software.